VYSOKÉ UČENÍ TECHNICKÉ V BRNĚ
BRNO UNIVERSITY OF TECHNOLOGY

FAKULTA STROJNÍHO INŽENÝRSTVÍ
FACULTY OF MECHANICAL ENGINEERING

ÚSTAV FYZIKÁLNÍHO INŽENÝRSTVÍ
INSTITUTE OF PHYSICAL ENGINEERING

PŘÍPRAVA VZORKŮ PRO ELEKTROCHEMICKÉ STUDIUM POVRCHŮ – TRANSPORT VZORKU MEZI UHV A ELEKTROCHEMICKÝM PROSTŘEDÍM

UHV-EC TRANSFER SYSTEM FOR ELECTROCHEMICAL SURFACE SCIENCE STUDIES

DIPLOMOVÁ PRÁCE
MASTER'S THESIS

AUTOR PRÁCE — **Bc. Zdeněk Jakub**
AUTHOR

VEDOUCÍ PRÁCE — **Ing. Miroslav Bartošík, Ph.D.**
SUPERVISOR

BRNO 2016

VYSOKÉ UČENÍ TECHNICKÉ V BRNĚ
FAKULTA STROJNÍHO INŽENÝRSTVÍ

Zadání diplomové práce

Ústav:	Ústav fyzikálního inženýrství
Student:	**Bc. Zdeněk Jakub**
Studijní program:	Aplikované vědy v inženýrství
Studijní obor:	Fyzikální inženýrství a nanotechnologie
Vedoucí práce:	**Ing. Miroslav Bartošík, Ph.D.**
Akademický rok:	2015/16

Ředitel ústavu Vám v souladu se zákonem č.111/1998 o vysokých školách a se Studijním a zkušebním řádem VUT v Brně určuje následující téma diplomové práce:

Příprava vzorků pro elektrochemické studium povrchů – transport vzorku mezi UHV a elektrochemickým prostředím

Stručná charakteristika problematiky úkolu:

K dalšímu vývoji nízkoteplotních palivových článků je třeba nalézt vhodný katalyzátor pro redukci kyslíku. Hledaný katalyzátor by měl v ideálním případě být levný, stabilní a neškodný k životnímu prostředí. Nedávné publikace napovídají, že některé oxidy mohou mít katalytickou aktivitu pro redukci kyslíku srovnatelnou s platinou, dosud však není zcela jasné, proč tomu tak je. Mnoho oxidů relevantních pro katalýzu je již základně prozkoumáno pomocí ultravakuových metod, detailní výzkum stále probíhá (např. studium vlastností různých adatomů na magnetitu Fe_3O_4). Pro další výzkum v tomto směru je nutné porozumět vlastnostem vybraných povrchů i v elektrochemickém prostředí.

Cíle diplomové práce:

1. Navrhnout a sestrojit systém pro transport vzorků z UHV komory do elektrochemického prostředí. Systém musí minimalizovat kontaminaci vzorků z atmosféry, měl by být snadný na obsluhu a měl by umožňovat transport vzorků různých velikostí a tvarů.
2. Otestovat sestrojený UHV-EC transfer systém měřením voltametrie známých standartních vzorků, např. Au(111) v kyselině sírové nebo Pt(111) v kyselině chloristé.
3. Vyvinout postup UHV přípravy vzorků pro in-situ elektrochemické STM.
4. Provádět další studium systémů kov/Fe_3O_4.

Seznam literatury:

H. E. HOSTER, H. A. GASTEIGER. Ex-situ surface preparation and analysis: Transfer between UHV and electrochemical cell, Handbook of Fuel Cells – Fundamentals, Technology and Applications, 236-265 John Wiley & Sons, Ltd, 2003, ISBN: 0-471-49926-9.

M.H.M. AHMED, F.P. LYDIATT, D. CHEKULAEV, P.L. WINCOTT, D.J. VAUGHAN, J.H. JANG, S. BALDELLI, A.G. THOMAS, W.S. WALTERS, et al. Wet chemically prepared rutile TiO2(110) and TiO2(011): Substrate preparation for surface studies under non-UHV conditions. Surface Science. 2014, 630: 41-45. DOI: 10.1016/j.susc.2014.06.020.

A. J. BARD, L. R. FAULKNER. Electrochemical methods: fundamentals and applications. New York: Wiley, 2001, 833 p. ISBN 0471043729.

Termín odevzdání diplomové práce je stanoven časovým plánem akademického roku 2015/16

V Brně, dne

L. S.

prof. RNDr. Tomáš Šikola, CSc. ředitel ústavu	doc. Ing. Jaroslav Katolický, Ph.D. děkan fakulty

Abstrakt

Tato diplomová práce se zabývá výzkumem vybraných povrchů oxidů železa, konkrétně $Fe_3O_4(001)$ and α-$Fe_2O_3(012)$. Použité výzkumné metody spojují tradiční techniky používáné v prostředí ultravysokého vakua (UHV) s technikami používanými v elektrochemickém (EC) prostředí. Současný stav poznání související s vybranými povrchy je stručně shrnut, je diskutována nutnost porozumět chování těchto materiálů také v elektrochemickém prostředí. V této práci je prezentován návrh a konstrukce systému pro transport vzorků z UHV do EC prostředí, jednotlivé konstrukční detaily jsou popsány a diskutovány. Vyvinutý systém je použit pro testování stability známé $(\sqrt{2} \times \sqrt{2})R45°$ povrchové rekontrukce na $Fe_3O_4(001)$. Zmíněná povrchová rekonstrukce je používaná jako substrát, který stabilizuje jednotlivé adsorbované atomy a zabraňuje jejich shlukování, což umožňuje zkoumat katalytické vlastnosti jednotlivých atomů. Experimentální část této práce ukazuje, že tato rekonstrukce je stabilní i v reálných podmínkách, přežije kontakt se vzduchem i vodou. Dále jsou v této práci prezentovány první obrázky povrchu α-$Fe_2O_3(012)$ pořízené rastrovacím tunelovacím mikroskopem (STM). Obě dosud známé povrchové rekonstrukce tohoto povrchu byly zobrazeny s atomárním rozlišením. Současný model (1×1) povrchu je touto prací potvrzen, pro (2×1) povrch prezentujeme nový povrchový model navrhnutý na základě pořízených STM obrázků. Dále byly provedeny studie adsorpce H_2O a O_2 na (2×1) rekonstruovaném povrchu pomocí časosběrného STM zobrazování.

Summary

This thesis deals with the combined ultra-high vacuum (UHV) and electrochemical (EC) studies of selected iron oxide surfaces, namely $Fe_3O_4(001)$ and α-$Fe_2O_3(012)$. The state-of-the-art knowledge regarding these surfaces is briefly reviewed, and importance of understanding these materials in the electrochemical environment is discussed. The design of the transfer system between UHV and EC environment is presented; individual features of the system are thoroughly discussed and the system is used for testing the stability of the $Fe_3O_4(001)$ $(\sqrt{2} \times \sqrt{2})R45°$ surface reconstruction in ambient conditions. The experimental results presented in this thesis show that the $Fe_3O_4(001)$ $(\sqrt{2} \times \sqrt{2})R45°$ reconstruction, utilized as an adatom array for single atom catalysis studies, survives both exposure to air and to liquid water, if the exposure is achieved in well-controlled fashion. Further, this thesis presents the first-ever atomic scale scanning tunneling microscopy (STM) study of the α-$Fe_2O_3(012)$ surface, which is important for photoelectrochemical water splitting. STM images of two surface reconstructions of the α-$Fe_2O_3(012)$ surface known to date are presented. A bulk terminated model of the (1×1) reconstruction is confirmed and a novel surface structure model for the (2×1) reconstructed surface is proposed. Adsorption studies of H_2O and O_2 on the (2×1) reconstructed surface are documented by timelapse STM.

Klíčová slova
rastrovací tunelovací mikroskop (STM), UHV-EC, magnetit Fe_3O_4, hematit α-Fe_2O_3, oxidy železa, povrchová struktura, stabilita povrchových rekonstrukcí, katalýza na jednotlivých atomech

Keywords
Scanning Tunneling Microscopy (STM), UHV-EC, magnetite Fe_3O_4, hematite α-Fe_2O_3, iron oxides, surface structure, surface structure stability, single atom catalysis

Jakub, ZDENĚK. *Příprava vzorků pro elektrochemické studium povrchů – transport vzorku mezi UHV a elektrochemickým prostředím* . Brno, 2016. 77 s. Diplomová práce. Vysoké učení technické v Brně. Fakulta strojního inženýrství. Vedoucí práce Miroslav BARTOŠÍK.

Prohlašuji, že jsem diplomovou práci *Příprava vzorků pro elektrochemické studium povrchů – transport vzorku mezi UHV a elektrochemickým prostředím* vypracoval samostatně pod vedením Ing. Miroslava Bartošíka, Ph.D. s použitím materiálů uvedených v seznamu literatury.

Bc. Zdeněk Jakub

None of the work presented here would have been possible without many people helping me along the way. First of all, I'd like to thank Asst. Prof. Gareth Parkinson for the supervision of my master project and for providing an endless stream of motivation. Ing. Jan Balajka and Dr. Roland Bliem deserve a lot of praise for teaching me how to operate UHV machines and answering loads of my dumb questions. Prof. Michael Schmid has always been a go-to guy in times of despair, unexplainable phenomena and malfunctioning equipment. He also provided most of the design ideas used in the construction of the transfer system. Herbert and Rainer, the workshop wizards, have always accepted my sometimes disorganized drawings and actually made a real thing out of it. I'd also like to thank Prof. Tomáš Šikola and Prof. Ulrike Diebold for making this all possible by allowing me to do my master project at the TU Wien, and Ing. Miroslav Bartošík, Ph.D for supervising my thesis in Brno. Last but not least, I'd like to thank my family, friends and Anne for always supporting me during my studies.

Bc. Zdeněk Jakub

Contents

Introduction

With iron and oxygen belonging to the most abundant elements in the Earth's crust, iron oxides play important roles in many natural and man made processes. Countless mountains, canyons and valleys owe its names to the red hue caused by hematite (α-Fe_2O_3). The prehistoric paleolithian paintings on the cave walls were created using hematite based Ochre pigments. The migrating pigeons are able to keep their course due to the magnetite (Fe_4O_4) nanoparticles present in their beaks [1]. Ancient chinese civilizations were able to utilize the same concept when they invented the first compasses.

The enormous abundance, low cost and environmental benignity of iron oxides makes them highly intriguing for applications in wide range of fields such as catalysis [2], medicine [3] or energy storing [4]. The two applications relevant for this thesis are single atom catalysis on $Fe_3O_4(001)$ surface and photoelectrochemical water splitting on α-Fe_2O_3.

The surface science group at the Institute of Applied Physics, Technical University Vienna made a great progress in the fundamental research of the $Fe_3O_4(001)$ surface over the past few years [5], [6], [7]. This surface is highly promising for single atom catalysis applications, because dense arrays of single metal adatoms remain stable at reaction temperatures. The concept of single atom catalysis has already been demonstrated, but exactly how the atoms are stabilized and the reaction mechanism remains a mystery. The ultimate goal to develop catalysts for real industrial applications requires to establish these factors in a controlled environment, and then continue the research in more realistic conditions. Testing the stability of the $Fe_3O_4(001)$ surface reconstruction in ambient conditions is the first project described in this thesis.

The second project of this thesis is the fundamental research of the α-$Fe_2O_3(012)$ surface. The research of hematite based photoanodes for electrochemical water splitting has been going on for nearly four decades now. Surprisingly, some of the fundamental surface science studies of the most common hematite surfaces have not been carried out yet, and the surface structure remains unknown. The first ever atomic-scale scanning tunneling microscopy (STM) study of the α-$Fe_2O_3(012)$ surface is presented in the experimental chapter of this thesis.

The overarching topic of this thesis is connecting the UHV expertise with electrochemical (EC) methods. The crucial part is the design and construction of the transfer system between UHV and EC environment. In the magnetite $Fe_3O_4(001)$ project, the current state of knowledge already enables us to do the first UHV-EC experiments, but in the case of α-$Fe_2O_3(012)$, the project is in a very early stage and the UHV-EC experiments will to be carried out once the surface structure is understood.

This thesis is divided into four chapters. The first chapter briefly summarizes the current knowledge of the $Fe_3O_4(001)$ and α-$Fe_2O_3(012)$ surfaces. The second chapter gives a description of the methods used for surface characterization in the experimental section. The third chapter deals with the design and construction of the UHV-EC transfer

system. The last chapter describes the experimental work done on the $Fe_3O_4(001)$ and α-$Fe_2O_3(012)$ surfaces.

1. The Samples

1.1. Magnetite Fe_3O_4

Magnetite provided mankind with probably the first experience with magnetism, giving rise to world's first compasses in ancient China. Hundreds of years later, magnetite still serves as a material of choice to make big discoveries on. Bragg solved the spinel structure on magnetite [8], Verwey described one of the first metal-insulator transitions on magnetite [9], Neel chose magnetite as a prototype system to his theory of ferrimagnetism. The hot topics in magnetite research today include targeted drug delivery [3], polluted water remediation [10], heterogeneous catalysis [2] and many more [11].

One of the most exciting topics discussed in connection with magnetite is Single Atom Catalysis (SAC). Ever since the first reports showing the size dependent catalytical activity of nanoclusters of various metals [12], [13], there has been an active search for ways to make these nanoclusters smaller and stable. Many succesful methods of preparing sub-nanometer clusters with high catalytic activity have been published over the past decades [14], [15]. That being said, already in 2003 it has been shown on Au/ceria catalyst, that for the water gas shift reaction all the catalytic activity was due to the single atom species, the sub-nano particles and clusters playing no role at all [16]. That claim set off an active pursuit of the topic and many approaches to prepare and stabilize single atoms on various supports have been published since [17], [18], [19].

The (001) surface of magnetite can support single atoms up to high coverages, preventing them from sintering even at elevated temperatures [5]. This makes this system ideal for SAC studies. Since then, properties of many different adatoms on magnetite (001) have been studied extensively [20], [7] [21]. A big advantage of the Fe_3O_4(001) adatom template is that its surface structure is known and all the reactions can be followed on atomic scale using Scanning Tunneling Microscopy (STM), as was shown for CO oxidation on Pt/Fe_3O_4(001) system [22].

While some impressive SAC work has been done on FeO_x substrates studied by Transmission Electron Microscope (TEM) [17], the unknown termination of the FeO_x makes fundamental studies of SAC very difficult. The thorough studies of stability, reaction mechanisms and deactivation processes can only be done on well-defined systems, such as magnetite (001).

1.1.1. Bulk Structure

Magnetite is the most abundant member of the spinel group. The general formula for spinel minerals is $A^{2+}B_2^{3+}O_4^{2-}$, where A, B are the cations and O is the anion. For spinels, the anion is usually oxygen, although structures with similar atoms (S, Se, Te) also exist - those are then called thiospinels [23]. In magnetite, both the A,B cations are iron.

The spinel structure is based on the face-centered cubic (fcc) lattice of O^{2-} anions. In the fcc lattice, 1/8 of the tetrahdral and 1/2 of the octahedral interstitial sites are occupied, see figure 1.1. Based on which of the A^{2+} and B^{3+} cations occupy which sites, we distinguish between the normal and inverse spinel.

In a normal spinel, the B^{3+} cations occupy the octahedral sites and the A^{2+} cations occupy the tetrahedral sites. In an inverse spinel, the B^{3+} cations occupy all the available tetrahedral sites and half of the available octahedral sites, the other half being filled by A^{2+} cations. In the following, the cations in tetrahedral (octahedral) sites are labeled by subscript X_{tet} (X_{oct}).

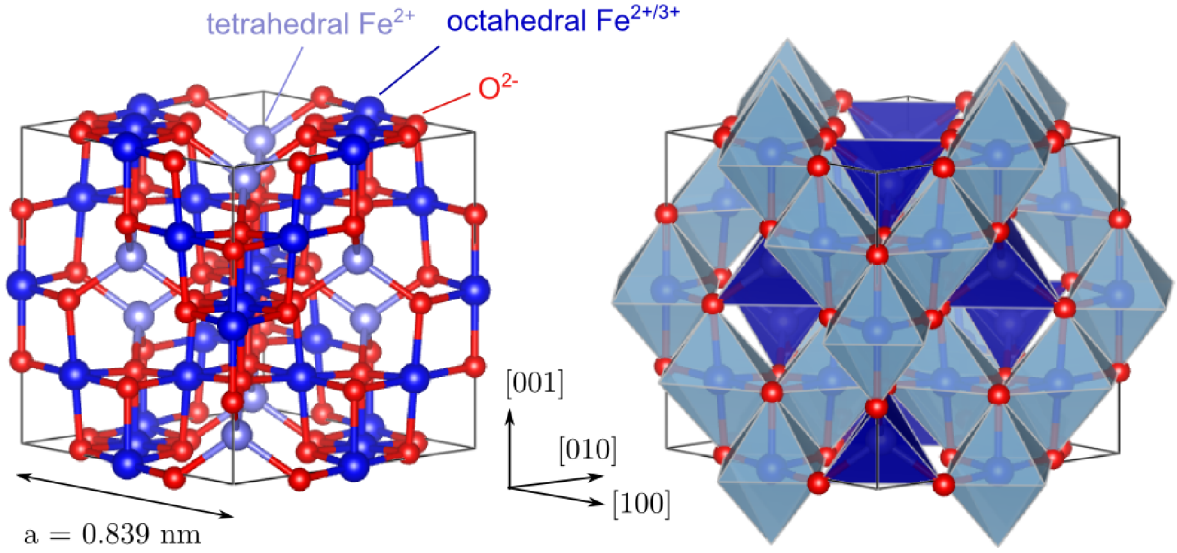

Figure 1.1: Ball-and-stick and polyhedral models of magnetite. The spinel structure is based on face centered cubic lattice of O^{2-}. Cations occupy 1/8 of the tetrahedral sites and 1/2 of the octahedral sites. Cations in the tetrahedral sites are Fe^{2+}, the octahedral sites are filled with with 50:50 mixture of Fe^{2+} and Fe^{3+}.

Magnetite (Fe_3O_4) crystalizes in an inverse spinel structure, meaning the Fe^{3+} and Fe^{2+} cations coexist in the octahedral sites. This fact is responsible for the relatively high conductivity of magnetite above the Verwey transition temperature 120 K. Below this temperature the electron hopping between the Fe^{2+}_{oct} and Fe^{3+}_{oct} is significantly reduced and the conductivity abruptly drops by two orders of magnitude [9].

Fe_3O_4 owes its name to its magnetic properties at ambient temperatures. After it was long considered a ferromagnet, Neel used magnetite as a prototype material for his theory of ferrimagnetism, proposing the Fe_{oct} and Fe_{tet} are antiferromagnetically coupled in magnetite. That means the unit cell magnetic moment of the Fe^{3+} is zero and all the magnetization comes from the Fe^{2+}. The Curie temperature for magnetite is 858 K.

1.1.2. Relevant surfaces

The natural magnetite single crystals are most commonly octahedrons enclosed by {111} surfaces. Apart from that, {100} facets have also been reported on artificially grown single crystals [24]. The energetic preference for {111} and {100} surfaces is supported by most of the theoretical DFT studies [25], [26] although there have also been some studies contradicting that [27]. Understandably, those two surfaces are the most extensively studied experimentally. The remaining low-index surface {110} does not recieve as much

attention. Recently it was shown, that the known surface reconstruction of the (110) surface is actually formed by {111} nanofacets [28].

All of the mentioned surfaces are comercially available as polished natural single crystals. Apart from that, magnetite single crystals can be prepared synthetically using variety of techniques. Many studies of all the mentioned surfaces have also been made on thin films grown on various substrates [29].

The experimental work of this thesis is based on the (001) magnetite surface, therefore only this one is described in detail in the following section. For further details the interested reader is referred to [11].

1.1.3. The (001) Surface

The (001) is probably the best understood magnetite surface at the moment. The Surface Cation Vacancy (SCV) model of the surface reconstruction published in 2014 agrees very well with both the experimental results and the theoretical calculations [6]. Relatively straightforward and reproducible preparation of the surface along with well-documented surface defects make this surface ideal for further studies.

One of the most exciting properties of the (001) magnetite surface is its ability to support single adatoms at elevated temperatures, which is the necessary prerequisite for Single Atom Catalysis (SAC) studies.

Subsurface Cation Vacancy (SCV) Termination

In the (001) direction, magnetite consists of alternating planes of Fe_{tet} and $(Fe_{oct})_2O_4$. At the surface, terminated by the $(Fe_{oct})_2O_4$ plane, a very well-known $(\sqrt{2} \times \sqrt{2})R45°$ reconstruction is formed. In the Scanning Tunneling Microscope (STM) image, characteristic undulating Fe rows are present, creating the so-called "narrow" and "wide" sites (see figure 1.2). Up to recent past, the Distorted Bulk Truncation (DBT) model of the surface was widely accepted [30], because it was the only model that could qualitatively explain the undulating rows, even though according to this model they should be much less pronounced than they are in STM. The quantitative Low-Energy Electron Diffraction (LEED IV) measurements, which were used as a proof of this model, showed only average agreement between theoretical and experimental curves (the Pendry factor $R_p = 0.34$).

The experiments that put the DBT model off the table were however the adsorption studies of different metals on the surface. It was shown that the (001) magnetite surface can support single gold adatoms up to high coverages at elevated temperatures [5]. The adatoms sit exclusively in the "narrow" site of the structure (see figure 1.2), which is difficult to accept in terms of the DBT model, where the "narrow" and "wide" sites are almost equivalent. Even more disturbing was then the study of cobalt on $Fe_3O_4(001)$, where the Co adatoms were reported to incorporate into the surface, locally creating the (1×1) bulk terminated surface reconstruction, which is inexplainable by the DBT [21].

The Subsurface Cation Vacancy structure, developed by DFT+U calculations based on experimental results, introduces interstitial Fe_{int} atoms sitting between the two Fe_{tet}, effectively blocking the "wide" side for adsorption. The origin of those Fe_{int} is in the third layer, where there are two octahedrally coordinated Fe_{oct} missing for every Fe_{int} (see figure 1.3), resulting in a net reduction of one Fe atom per unit cell. The SCV structure was convincingly confirmed by quantitative LEED IV measurements showing very good agreement with the model (the Pendry factor $R_p = 0.125$).

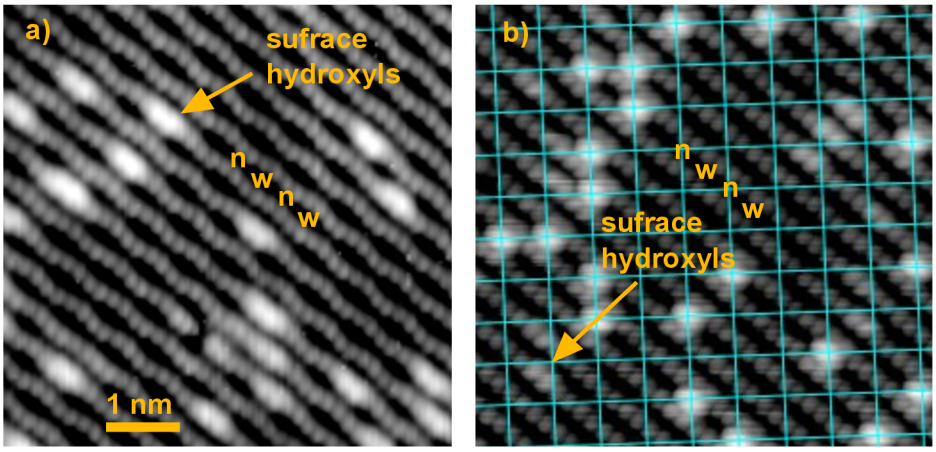

Figure 1.2: (a) Scanning Tunneling Microscopy images feature Fe_{oct} rows with distinguishable "narrow" and "wide" site (highlighted by the "n" and "w" letters). The white protrusions on the row are surface hydroxyls (b) The deposited atoms (nickel in this case) sit exclusively in the "narrow" site as highlighted by the grid. The "narrow" and "wide" site are not that distinguishable in the (b) image because of the STM tip shape.

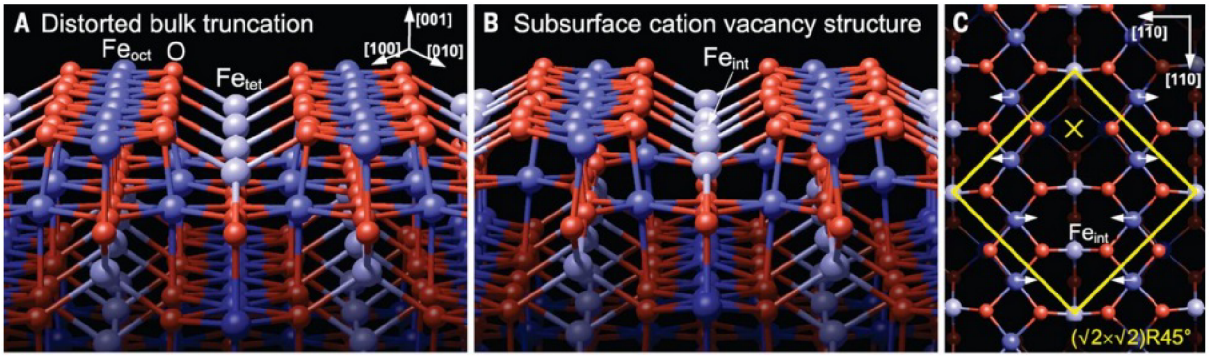

Figure 1.3: Magnetite (001) surface structure models: (a) distorted bulk truncation, (b) subsurface cation vacancy. The subsurface cation vacancy features interstitial Fe_{int} effectively blocking one of the two available adsorption sites (c). The yellow cross marks the preferred adsorption site. Two Fe_{oct} in the third layer are missing under every Fe_{int}. Picture reprinted from [6].

What is more, the SCV explains all the experimentally observed phenomena. The undulations of Fe_{oct} rows are much more pronounced than in the DBT model. The adsorption of atoms occurs only in one of the two available sites per unit cell, because the other one is blocked by Fe_{int}. Incorporation of some atoms happens, when one incident atom fills the vacant octahedral site in the third layer and Fe_{int} moves to occupy the other.

All available evidence suggests that the SCV model is correct. The reason for mentioning the DBT in this section is that the SCV model was published very recently and most of the published DFT calculations and papers regarding metal adsorption are based on the DBT model.

SCV as an Adatom Template

Magnetite (001) serves as an adatom template, binding one atom per unit cell. This results in an adatom array with nearest neighbour distance 0.84 nm. Since the first work with Au adatoms was carried out [5], many other metals including Pt [22], Pd [20], Ag [7], Co [21], Ni [21], Ti [21], Sr, Cu, Ir, Mn, Sn and Rh (unpublished) adatoms have been studied in the Surface Physics group at Technical University Vienna (see figure 1.4). Although the adsorption site is always the same, the different adatoms don't always behave similarly. The ferrite-forming atoms such as Co, Ni, Ti incorporate in the surface at slightly elevated temperatures, while the others remain stable until the $(\sqrt{2} \times \sqrt{2})$R45° reconstruction is lifted at roughly 700 K. Some (such as Au) stay put in the specific "narrow" site and become mobile when a dimer is formed, others (such as Ag) jump between neighbouring "narrow" sites as single atoms and become fixed to one site when they form a dimer. Comprehensive review of metal/Fe_3O_4(001) adatom systems is given in [11]. Properties of metal adatoms relevant for this thesis are described in chapter 4.

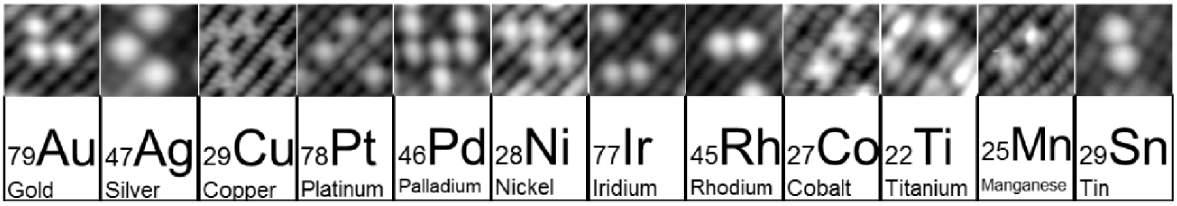

Figure 1.4: Various adatoms deposited on the Fe_3O_4(001) surface, imaged by STM with various parameters. All of them bind to the "narrow" site and do not sinter at room temperature. Picture provided by Roland Bliem.

Apart from studies of adatom array thermal stability, the adatom reactivity with gases has been studied, yielding important results. Proof of the nanocluster catalysis concept on metal/Fe_3O_4(001) system has been given by showing the catalytic cycle of CO oxidation on Pt adatoms and clusters (see figure 1.5) [22]. The known, yet not understood phenomenon of CO oxidation SAC deactivation over time has been elucidated on Pd/Fe_3O_4(001) system [20].

Motivation

Much more work is to be done on metal/Fe_3O_4 systems. The concept is proven, the properties of different single atoms are well documented, the adsorption studies of different gases on different adatoms are being carried out.

When the adsorption properties are known, it's possible to tailor catalysts for specific reactions. Depositing adatoms of a different kind on the same substrate is possible, the only challenge is to choose the right ones. Getting a detailed database of adsorption and molecular-splitting properties of different atoms is a huge step forward, so the first prototypes of tailored single atom catalysts based on Fe_3O_4(001) should come to light in foreseeable future.

So far all the work has been done in a well-defined ultrahigh vacuum (UHV) environment. The ultimate goal being to create catalysts for real applications, the next step is to check, whether the adatoms survive the exposition to high pressure environment, both gaseous and aqueous. The work presented in this thesis contributes substantially to

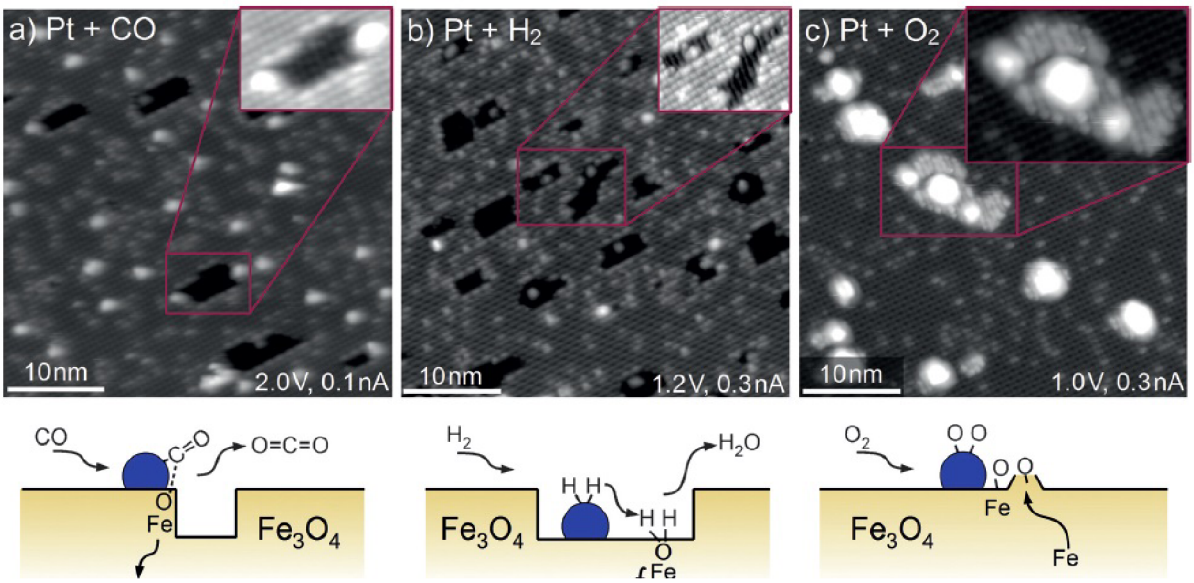

Figure 1.5: Proof of the surface science approach to single atom catalysis concept on Pt/Fe_3O_4 system. Both CO (a) and H_2 (b) extract oxygen from the magnetite lattice, creating "holes" in the surface. The process is clearly catalyzed by the Pt species - all of the holes are created either right next to Pt atom/cluster (a) or around it (b). Dosing O_2 on the system causes growth of new layers around the Pt species. Picture reprinted from [22].

this cause. If the adatoms survive the high pressure treatment, a detailed study of their behaviour in ambient conditions is going to be carried out.

The long-term plan to develop single atom catalyst based on magnetite (001) for real industrial applications then include creating ordered array of artificially grown Fe_3O_4 nanocubes exposing (001) planes [31].

1.2. Hematite α-Fe_2O_3

Hematite is the most thermodynamically stable form of iron oxide under ambient conditions and as such, it is also the most common form of crystalline iron oxide [32]. For its enormous abundance in Earth's crust, it plays an important role in many natural processes such as dissolution, anaerobic microbial metathesis or organic transport [33]. It also possesses great potential for high-tech applications - polluted water remediation [34], energy storage [4] or heterogeneous catalysis [4] are being discussed in connection to hematite.

Perhaps the most intriguing potential application of hematite is in photoelectrochemical (PEC) cells for water splitting, which would enable efficient harvesting of solar energy, directly converting it into chemical energy. In a photoanode of PEC cell for water splitting generation of electron-hole pairs is induced by sunlight. The electrons are then transferred to the cathode, where they reduce water to H_2 and OH^-, while the holes are used for OH^- oxidation to O_2 at the anode. That way, spatially separated H_2 and O_2 gas is generated.

Hematite meets some of the important requirements for the PEC cell photoanodes - a small semiconductor bandgap ($\approx$ 2 eV), durability in aqueous environments, environmental benignity and low cost [32]. For these reasons, hematite has been studied as a photoanode material for PEC water splitting for nearly 40 years now. Theoretical

solar-to-hydrogen efficiency of hematite photoanode lies around 15 %, the real achievable values are however much lower. The most notable drawbacks causing this discrepancy include very low hole diffusion length (2–4 nm) compared to relatively high light penetration depth ($\sim 10^2$ nm), short excited state lifetime (≈ 1 ps), poor electrical conductivity ($\sim 10^{-2}\,\mathrm{cm^2V^{-1}s^{-1}}$), and sluggish oxygen evolution reaction at the electrode/solution interface [35].

Various strategies have been developed to overcome these limitations. Nanophotonic structures, reflective coatings, plasmonic structures are tested to improve light absorption. The charge transfer, limited by low hole diffusion length, can be significantly enhanced by changes in morphological design, i.e. array of nanowires, nanotubes, dendrites, nanosheets etc. Lowering the high overpotential needed for the oxygen evolution reaction at the photoanode surface remains a great challenge, which has been addressed by introducing co-catalysts, surface passivation layers or surface chemical corrosion [32], [35].

Especially for the last point, understanding the surface structure of hematite might become an important step in improving the effectivity of hematite-based photoanodes for PEC water splitting.

1.2.1. Bulk Structure

The structure of hematite is based on hexagonal close packed (hcp) anion O^{2-} lattice stacked along the [001] direction. The octahedral interstitial sites are occupied by Fe^{3+} cations in a regular fashion - two filled sites followed by one empty, see figure 1.6. The pairs of occupied-face sharing octahedra are slightly distorted from the ideal packing of the cation sub-lattice, as the cations repell each other and shift towards the unshared faces [35]. As a consequence of this distortion, two different Fe-O bond lengths are present in hematite structure. The tetrahedral sites remain unoccupied.

Hematite is perfectly antiferromagnetic at temperatures below 260 K (referred to as Morin temperature). Above this temperature, the slight trigonal distortion of the octahedra causes destabilization of the antiferromagnetic ordering between the (001) iron planes, which results in hematite being weak (parasitic) ferromagnet [36]. The Neel temperature for hematite is 950 K.

In the absence of doping or impurities, conductivity of α-Fe_2O_3 is poor and highly anisotrophic [37] - up to several orders of magnitude higher along the (001) plane than perpendicular to it [38]. That phenomenon can be explained considering the magnetic structure of hematite. The spins of the Fe are ferromagnetically coupled along the (001) planes and antiferromagnetically coupled along the [001] direction. That creates an environment, where the electrons can move within the (100) Fe layers, but are forbidden to hop across the oxygen planes to another Fe layer [32].

1.2.2. Relevant Surfaces

According to the theoretical calculations, the most energetically favourable low-index surface of hematite is the (012) (also referred to as $(1\bar{1}02)$ in hexagonal four-index notation or R-cut by a common name) [39]. The ideal shape is then a pseudocube enclosed completely by $\left\{1\bar{1}02\right\}$ surfaces. Those pseudocubes are also observed in nature, among other shapes.

That being said, the surface which has recieved the most attention from surface scientists is the (001) (also referred to as (0001) or C-cut). The reason for that probably is that this surface is most commonly grown as thin film on various substrates, which enables the

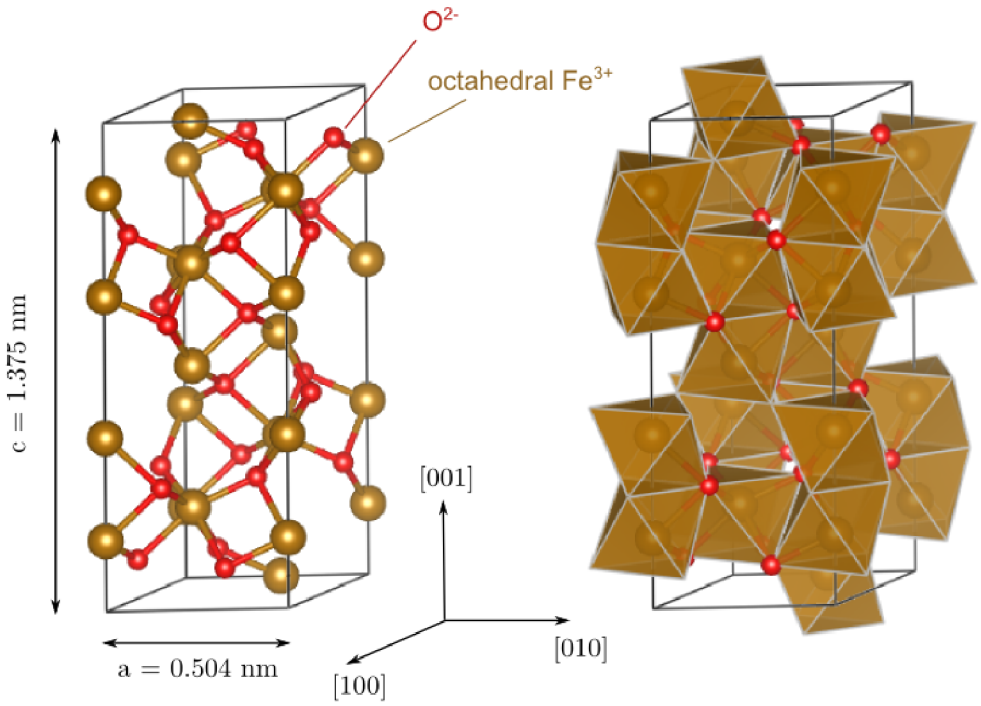

Figure 1.6: Ball-and-stick and polyhedral models of hematite unit cell. The oxygen forms slightly distorted hcp lattice. Two thirds of the octahedral sites are filled with iron, which can be seen on the polyhedral model - in the [001] direction there are always two face-sharing octahedra followed by one missing. Note the coordinate system is trigonal, not cartesian.

use of surface science techniques that require conductive samples, such as Scanning Tunneling Microscopy (STM) or X-Ray Photoelectron Spectroscopy (XPS). The (001) surface of hematite is however far from straigthforward to prepare in UHV conditions. Standard sputtering and annealing treatment reduces the surface and partially transforms it to $Fe_3O_4(111)$ [40]. Preparing stoichiometric α-$Fe_3O_3(001)$ in an UHV chamber surface was only reported to be possible by annealing in high pressures of oxygen [11].

The experimental work of this thesis is based on the (012) hematite surface, therefore only this one is described in detail in the following section. For further details the interested reader is referred to [11].

1.2.3. The (012) Surface

Very little work has been done on the α-Fe_2O_3 (012) so far. Already in 1988 it has been reported that there are two surface reconstructions possible with (1×1) and (2×1) symmetry that can be interconverted by oxidizing or reducing the surface [41]. Based on the ratio of distances in the Low Energy Electron Diffraction (LEED) pattern and ratio of intensities in of the O and Fe Auger lines in the Auger Electron Spectroscopy (AES), the proposed model for the (1×1) is simple bulk termination (see figure 1.7) [42].

The (2×1) surface structure is not known to date. The LEED pattern implies that the reconstruction takes place in the direction perpendicular to the zig-zag rows formed by surface oxygen atoms in the (1×1). The Electron Energy Loss Spectroscopy (EELS) spectra shows the (2×1) has Fe^{2+} cations on the surface. The simplest model for the (2×1) proposes a missing row feature on the bulk termination (see figure 1.7).

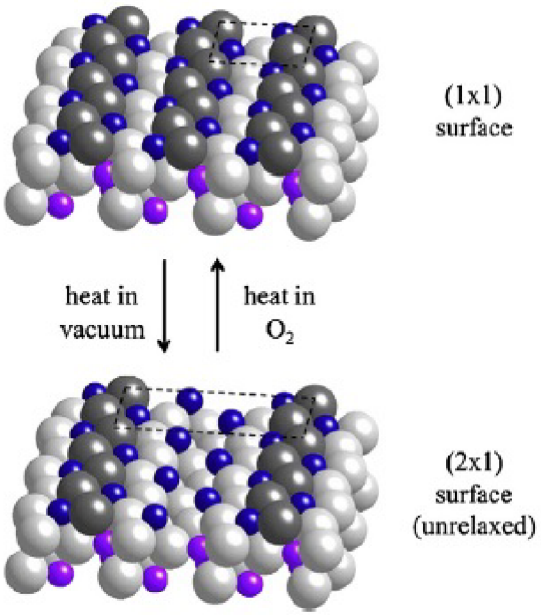

Figure 1.7: Surface reconstrucitons of hematite (012). The (1×1) surface is bulk terminated, it features oxygen (gray) rows (highlighted by dark gray) straddled by iron (blue). The surface structure of the (2×1) in unknown. The simplest proposed model is bulk termination with missing row. Picture reprinted from [43].

Both the (1×1) and (2×1) surface have been studied using water Temperature Programmed Desorption (TPD) [44]. Based on the TPD spectra, both recostructions adsorb water both dissociatively and molecularly, although different amounts and with different strengths [33]. The (2×1) surface adsorbs oxygen, both molecular and dissociated, which stabilizes some hydroxyls on the surface and destabilizes molecularly adsorbed water [43].

Adsorption of O_2 on the (2×1) surface at room temperature changes the electronic structure of the surface to one resembling the (1×1), as probed by EELS. That being said, LEED pattern does not change to (1×1) with O_2 adsorption, instead c(2×2) spots appear, suggesting an O_2 overlayer forms [43].

Motivation

For development of the cocatalysts or passivation layers on the photoanode surface, knowing the exact surface structure might prove to be crucial. Using the (012) surface as a model system, our plan is to document the phenomena taking place at the surface and investigate their behaviour at an atomic scale. With this knowledge, addressing the needs of surface modification on more complex polycrystalline surface of hematite photoanodes might become better targeted.

Choosing the classical UHV based surface science approach means taking a step back from the direct-application-motivated research of hematite photoanodes that is enjoying success lately. It is difficult to predict what impact our findings may have on the development of hematite based PEC cells. Since the subject has stayed out of the science mainstream for such a long time, any new discovery might become a significant one. But even in the worst case, this research will noticably extend the knowledge of surface structures of hematite (012), which is currently desperately incomplete.

Determining the surface structure is vital for further studies of the hematite (012) surface and its reactivity. Both confirming the (1×1) and determining the (2×1) structure

by Scanning Tunneling Microscopy would be an important step in the hematite research. As it has already been shown by water TPD studies that the surface strongly interacts with water in both its surface reconstructions, water dosing experiments will be carried out and documented by STM as well. All the so far published experimental data will be looked at from a different perspective, should the STM study turn out to be possible. If the UHV surface science approach yields results promising for further applications in PEC cells, then the in-situ Electrochemical STM studies combining the expertise from UHV and electrochemical surface science will be carried out. The ultimate motivation is to explain the electrochemical reactivity by the expertise acquired from UHV surface science.

2. The Techniques

This chapter gives brief description of the general principles of methods used in the experimental section. The parameters specific for given experimental apparatus are described in chapters 3 and 4.

2.1. Scanning Tunneling Microscopy (STM)

Ever since its Nobel prize awarded invention in 1981, Scanning Tunneling Microscopy has been a method of choice for determining the surface structure in many research groups all over the world. Its ability to relatively easily produce high quality atomically resolved images of conductive samples can only be matched by modern Atomic Force Microscopes (AFM).

STM belongs to the family of Scanning Probe Microscopes (SPM), meaning the crucial part of the microscope is a sharp tip scanning the imaged area line-by-line in close proximity to the sample surface. The SPM techniques differ by the feedback mechanism, that keeps the tip close to the sample, and by the type of information gathered by the tip. In the case of STM, the feedback mechanism is based on the quantum tunneling current, the gathered information is the topography and electronic structure of the sample.

2.1.1. Principle of operation

The tunnel effect can be explained in terms of quantum mechanics. Consider a wave function $\psi(\vec{r},t)$ belonging to a general particle, as was proposed by de Broglie in 1924. The wave function by itself has no physical meaning, but its squared modulus $|\Psi|^2$ is a real number interpreted as probability density of detecting the particle in given configuration. The wave function has to fulfill the Schrödinger equation

$$\mathrm{i}\hbar\frac{\partial\Psi(\vec{r},t)}{\partial t} = -\frac{\hbar}{2m}\Delta\Psi(\vec{r},t) + V(\vec{r},t)\Psi(\vec{r},t), \tag{2.1}$$

where $\hbar$ is the reduced Planck constant ($h/2\pi$), Δ is the Laplacian operator and V is the potential energy.

For simplicity, let's consider one-dimensional problem and potential energy $V(\vec{r})$ independent on t. The corresponding Schrödinger equation is

$$\mathrm{i}\hbar\frac{\partial\Psi(x,t)}{\partial t} = -\frac{\hbar}{2m}\Delta\Psi(x,t) + V(x)\Psi(x,t), \tag{2.2}$$

.

We can rewrite the $\Psi(x,t)$ as a product of two functions

$$\Psi(x,t) = \psi(x)\varphi(t) \tag{2.3}$$

and after putting this form into the Schrödinger equation we get separate equations for $\psi(x)$ and $\varphi(t)$

$$-\frac{\hbar}{2m}\Delta\psi(x)\frac{1}{\psi(x)} + V(x) = E, \tag{2.4}$$

$$\mathrm{i}\hbar\frac{\partial\varphi)}{\partial t}\frac{1}{\varphi(t)} = E, \tag{2.5}$$

where E is the sum of the kinetic and potential energy of the particle.

Let's consider the case an electron hitting a potential barrier. The height of the barrier is $V_0 > E$, the width is L, see figure 2.1. The solution of equation 2.4 can be expressed as linear combination of harmonic functions

$$\psi(x) = A\exp(\mathrm{i}kx) + B\exp(-\mathrm{i}kx), \tag{2.6}$$

where k is the length of the wave vector defined as

$$k = \frac{\sqrt{2m(V(x) - E)}}{\hbar}. \tag{2.7}$$

In the first and third region $V(x) = 0$ and k is a real number, meaning the solutions described in 2.4 are propagating waves. In the region 2, however, $V(x) = V_0 > E$ and the solutions have a form of exponential decay.

For the calculations of the A and B coefficients for every region, we use the conditions of continuity of the wave function and continuity of the first derivation of the wave function. The resulting probability P of detecting the electron on the other side of the barrier is exponentially proportional to the width of the barrier [45]

$$P = \frac{|\Psi_3|}{|\Psi_1|} = \frac{A_3^2}{A_1^2} \cong \exp(-2k_2L). \tag{2.8}$$

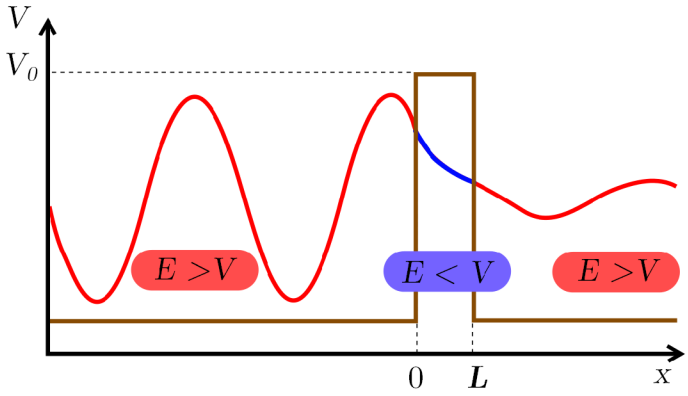

Figure 2.1: Illustration of a tunneling effect on a potential barrier. Electron with wave function Ψ_1 hits a potential barrier. Even though the potential barrier is higher than the energy of an electron, the wave function continues in the form of exponential decay through it. In the region behind the barrier, the wave function Ψ_3 has much lower, but still non-zero amplitude.

The vacuum between the STM tip and the sample surface is a potential barrier similar to the one described. The shapes of the barrier and the wave function are more complex and calculation of tunneling current is more complicated. For the theoretical STM simulations, usually a Tersoff-Hamman model is used [46]. But the general principle is clear even from the most simple case - when the bias voltage is applied, the tunneling current is exponentially dependent on the distance of the tip from the sample, which makes the detection of protrusions in the range of picometers possible [47].

2.1.2. Construction

The STM consists of the scanner head, electronics and computer for data processing (see figure 2.2). In the STM head, the relative movement between the tip and the sample is provided by piezomotors. Usually there are two kinds of piezomotors, one for the macroscopic approach and one for the fine motion and scanning. Generally, two designs are possible - either the tip is stationary and the sample holder moves or the other way around.

Since the distance between the tip and the sample needs to be measured with picometer precision, the whole system needs extraordinary isolation from external vibrations. Various damping systems based on springs, airsprings or eddy curl are therefore commonly part of the STM apparatus as well.

The tip is basically a piece of wire with a sharp end. Methods for creating such sharp end include cutting while pulling, chemical and electrochemical etching or selective growth. The most common materials for tips are tungsten or platinum iridium.

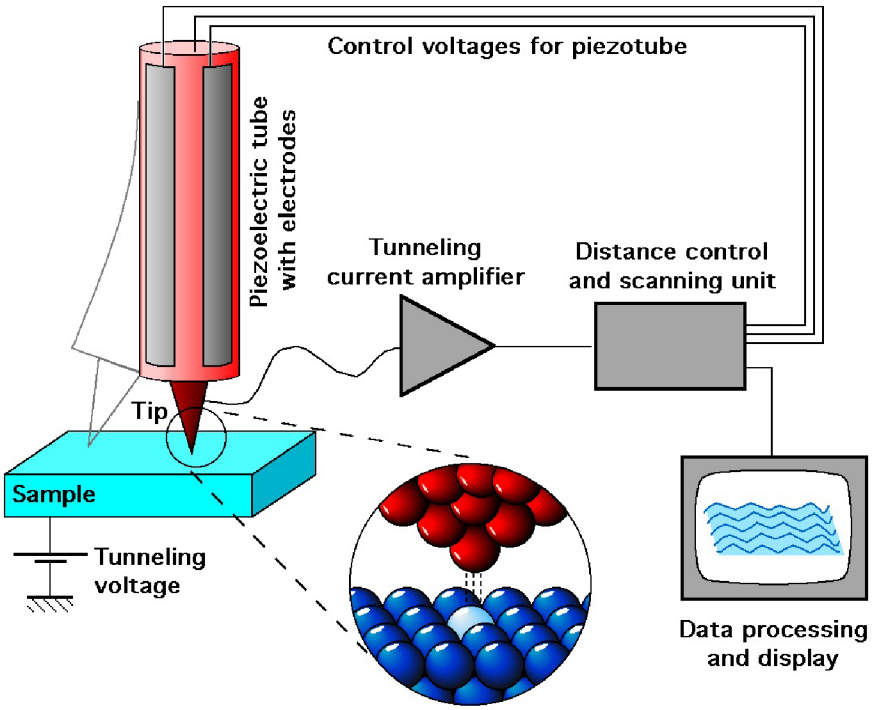

Figure 2.2: Schematic drawing of the Scanning Tunneling Microscope. Picture reprinted from [48].

2.1.3. Imaging

There are two basic modes of STM imaging: Constant height mode and constant current mode (see figure 2.3). In the constant current mode the tip scans over the surface and the electronics change the voltage on the piezomotors to keep the current constant. The z position of the tip then copies the topography of the sample. The image is created by assigning the piezo voltage signal to every point.

In the constant height mode the z position of the tip stays the same while scannning and the current changes. The current signal is then used to create an image. In the constant distance mode faster scanning is possible, but the danger of crashing is higher.

The working distance between the tip and the sample is usually in the range of angströms. The common bias voltages for STM imaging units of V, the tunneling currents are usually tenths of nA.

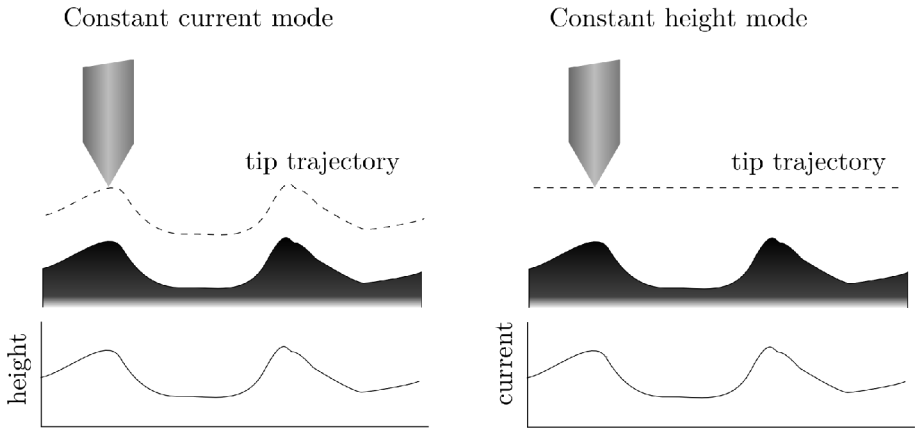

Figure 2.3: Constant current (left) and constant height (right) modes of STM imaging.

Because the sample needs to have electronic states in the vicinity of Fermi level, the measured samples must be conductive. Based on the polarity of the bias voltage, both empty states above Fermi level and filled states below Fermi level can be imaged by STM.

The information gathered by the tip is a mixed signal of topography and electronic structure. That means STM, while it may be quite accurate in determinig the height of terraces of the same kind, generally cannot be used for measuring the z dimension of surface features. The images can be decieving and features physically higher may look lower or may not be detected at all.

2.2. X-Ray Photoelectron Spectroscopy (XPS)

X-Ray Photoelectron Spectroscopy, also known as Electron Spectroscopy for Chemical Analysis (ESCA), is a surface-sensitive technique for measuring the elemental composition of the sample. Providing both qualitative and quantitative analysis, XPS can be used to identify elements on the surface, distinguish between the same elements bonded in different chemical states, and roughly determine the depth profiles of different species.

2.2.1. Principle of operation

The technique is based on the photoelectric effect. Energy transfer between an incident photon and electron occurs when the photon energy is larger than work function of the material and the binding energy of the electron.

The detected kinetic energy of the emitted electron is given by the equation

$$E_{kin} = h\nu - E_b - \Phi_{spec}, \tag{2.9}$$

where $h\nu$ is the energy of the incident beam, E_b is the binding energy of the atomic orbital from which the electron originates and Φ_{spec} is the work function of the spectrometer. For further explanation of this equation see figure 2.4.

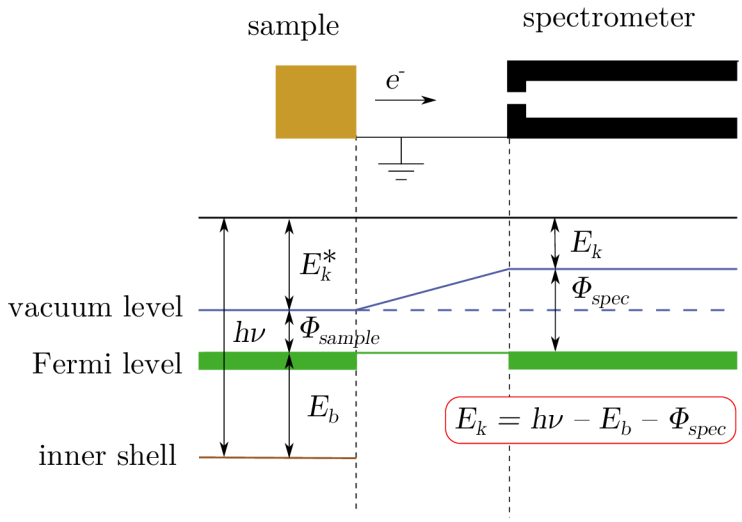

Figure 2.4: Illustration of equation 2.9. Picture adapted from [49]

In XPS, the sample is irradiated by monoenergetic x-rays and photoelectron counts at different energies are taken. In the resulting spectra, peaks can be assigned to electrons in specific states or other inelastic processes.

Although the photons travel micrometers deep into the sample, only the electrons from several top atomic layers are detected in XPS. That is due to the inelastic mean free path of the excited electrons, which is in the range of units to tens of Angströms for the relevant energies [47].

2.2.2. Construction

The x-ray source is usually water cooled twin-anode type with Mg (1253.6 eV) and Al (1486.6 eV) anodes (see figure 2.5). Electron beam with energy of 15 keV hits the selected anode which emits the x-rays. Thin Al foil window serves as simple a monochromator.

The analyzer is commonly of hemispherical type (see figure). It consists of two metal hemispheres with coincident curvature, between which voltage is applied. Only electrons with selected energy can pass through. A set of electrostatic lenses slows the electrons down before entering the hemispheres. The analyzer can work in two different modes - Constant Analyzer Energy (CAE) or Constant Retard Ratio (CRR). In the Constant Analyzer Energy the pass energy of the hemisphherical analyzer is fixed and all the energy adjusting is done by the focusing lense system. The advantag of this mode is constant energy resolution over the whole spectrum and most of XPS measurements are done using the CAE mode. In the Constant Retard Ratio, the ration of initial electron energy and analyzer pass energy is fixed. That way, the resolution is higher for high kinetic energy (low binding energy) and lower for low kinetic energy, where the intensity of the singal is much higher due to the background.

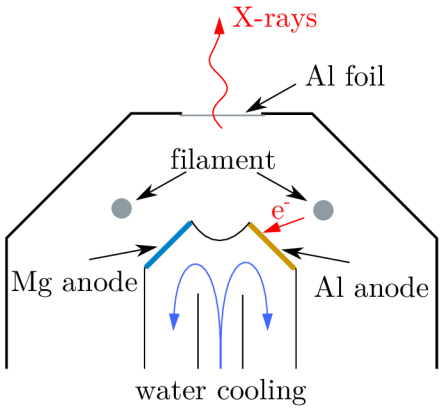

Figure 2.5: Schema of an x-ray source. Voltage of 15 keV is applied between the heated filament and the selected anode. X-rays are emitted from the anode, the Al foil window serves as a primitive monochromator.

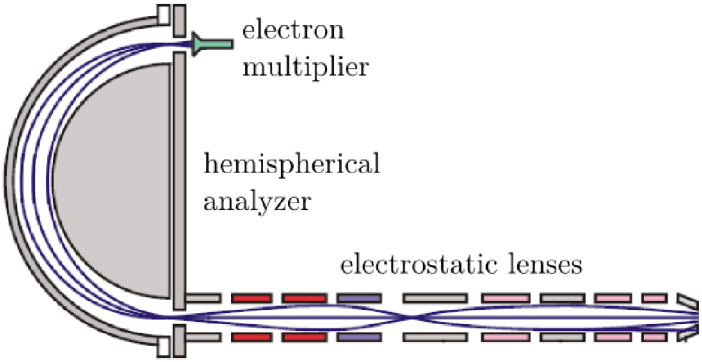

Figure 2.6: Scheme of a hemispherical analyzer. Picture adapted from [49].

The sample and the analyzer are conductively connected, so that their Fermi levels are the same and equation 2.9 applies. If the sample is not conductive, then this connection does not apply anymore, the sample becomes charged and the spectrum shifts.

2.2.3. Interpreting XPS spectra

The XPS spectra are usually labeled in terms of binding energy, not kinetic energy. That is convenient, because the photoelectron peaks keep their position when anode with different energy is used.

Apart from photoelectron emission, other processes take place on the sample under x-ray irradiation and other peaks are formed in the XPS spectra. The most common peaks are described in the following text.

Photoelectron peaks

Photoelectron peaks are the most important peaks in the XPS spectrum. Every element has a specific set of photoelectron peaks and by their energy, photoelectrons can be assigned to electrons in specific orbitals.

The electronic structure of an atom changes, when it is bound in a compound, therefore the photoelectric peaks shift for atoms in different binding state. In all orbitals apart from s, the spin-orbital splitting takes place and there are two peaks for every orbital.

Auger peaks

An electron from an outer shell filling a vacancy in the inner shell can cause another electron from outer shell to be emitted. This process called the Auger effect (see figure 2.7) and the Auger peaks are commonly present in XPS spectrum. Since the Auger effect is an intrinsic process, the kinetic energy of a specific Auger electron is always the same, meaning in the binding energy spectrum its position changes with different anode. That's the reason why dual-anode x-ray sources are usually used - in case an Auger peak overlaps with a photoelectron peak, changing the anode separates them in the spectrum.

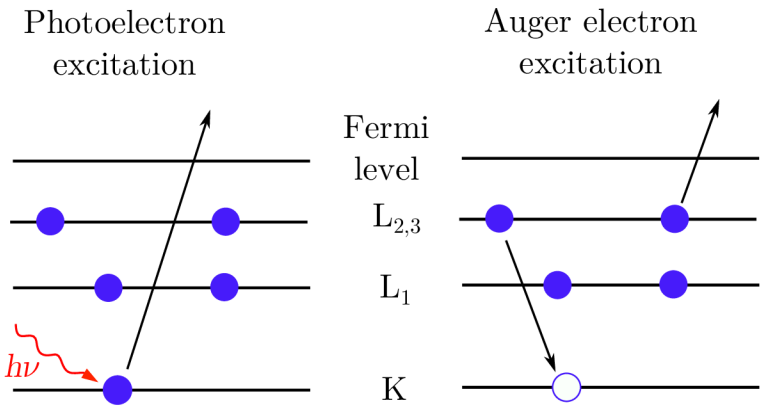

Figure 2.7: Illustration of photoelectron and Auger processes.

Satellite peaks

The x-ray source does not produce ideally monochromatic light. Although the Kα line is the strongest, there are other lines present, which results in duplicated peaks with constant offset. Because the intensity of the satellite peaks is much lower than that of the original peaks, usually they are only distinguishable next to really high peaks.

Plasmon and shake-up peaks

Excited plasmons and photoelectrons can excite different electron, causing it to be emitted. Those "tertiary" electrons have always lower kinetic energy than the "secondary" (the ones excited by x-rays) and therefore are detected to the left of the original photoelectron peak.

2.3. Low Energy Electron Diffraction (LEED)

Low energy electron diffraction is a technique used to determine the surface structure of single-crystalline materials. It can be used both qualitatively as a quick and straightforward method to check the surface symmetry or quantitatively (LEED IV) as a powerful tool to confirm proposed complex surface structure models.

2.3.1. Principle of operation

The sample is bombarded by an electron beam with energy of (10^1–10^2) eV. The electrons can be assigned a de Broglie wave with wavelength of

$$\lambda = \frac{h}{\sqrt{2mE}}, \tag{2.10}$$

which for those energies is units of Angströms, commensurate with interatomic distances. When incident to an ordered lattice, the electron beam scatters and the reflected electrons interfere constructively and destructively, creating a diffraction pattern.

The interfering waves have to fulfill the Laue diffraction condition, which states

$$\vec{k}_i - \vec{k}_f = \vec{G}, \tag{2.11}$$

where $\vec{k}_i$ is the wavevector of the incident beam, $\vec{k}_f$ is the wavevector of the diffracted beam and $\vec{G}$ is a general reciprocal lattice vector. The reciprocal lattice vector is a linear combination of basis vectors $\vec{g}_1$, $\vec{g}_2$, which are given by

$$\vec{g}_1 = 2\pi\frac{\vec{a}_1 \times \vec{n}}{\vec{a}_2 \times \vec{a}_2}, \qquad \vec{g}_2 = 2\pi\frac{\vec{n} \times \vec{a}_1}{\vec{a}_1 \times \vec{a}_2}, \tag{2.12}$$

where $\vec{a}_1$, $\vec{a_2}$ are the real space lattice vectors and $\vec{n}$ is a unit vector with direction perpendicular to the surface. The reciprocal lattice vectors are perpendicular to real space lattice vectors, their length is proportional to the reciprocal value of the real space lattice vectors. The Laue diffraction condition can be pictured by the Ewald's sphere. Because the electron beam only interacts with a few of the topmost atomic layers, the spots in the reciprocal space are very densely packed in the $\vec{k_z}$ direction, effectively creating "rods" (see figure 2.8).

When more layers are involved, there are brighter and darker spots on every "rod" which results in varying intensity of the spots with changing incident beam energy. This effect as well as multiple scattering is taken in consideration when measuring quantitative LEED IV. In LEED IV, the intensity of each spot at wide spectrum of energies is measured and the set of intensity spectra is fitted by a curve calculated for a specific proposed model and a level of agreement is checked.

The diffraction pattern is then imaged on a fluorescent screen. The surface sensitivity of LEED is determined by the inelastic mean free path, which is in the range of Angströms ($\approx$ several atomic layers) for low energy electrons [47]

2.3.2. Construction

The common configuration of LEED can be seen in figure 2.9. The hot cathode electron source emits electrons, which are accelerated and focused by electrostatic lenses to create a colimated electron beam. The reflected electrons pass through a set of concentric grids, that filter out inelastically scattered electrons and accelerate the elactically scattered ones to the concentric fluorescent screen. The diffraction pattern is acquired by the CCD camera.

2.3.3. Information in LEED patterns

The information obtained from LEED pattern originates from an area with diameter smaller than the coherence length of the electron beam, which for common LEED systems

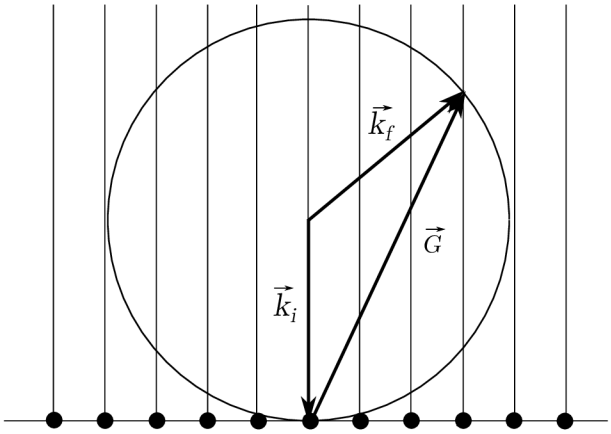

Figure 2.8: Ewald's sphere - an illustration of Laue diffraction conditions. Because the electron beam interacts only with the topmost few layers, the reciprocal lattice spots in the $\vec{k}_z$ direction are very densely packed together.

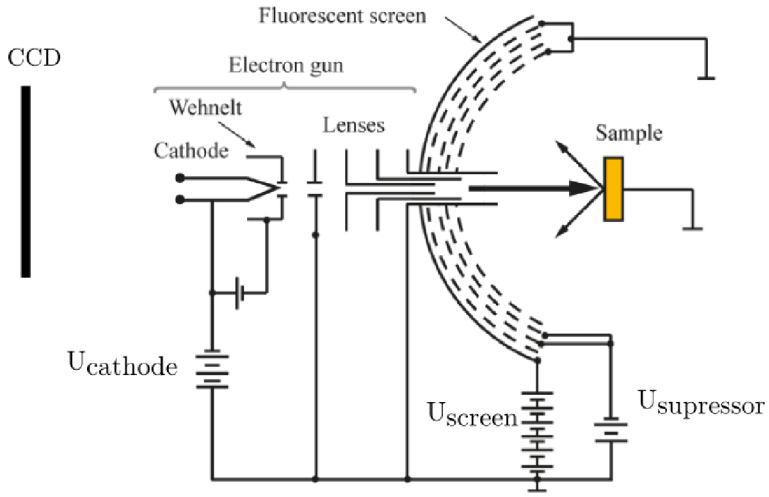

Figure 2.9: Experimental configuration of LEED. Picture adapted from [50].

is in the range of 10^2 Å[47]. Ideally, the LEED pattern of a crystal after preparation should feature bright and sharp diffraction spots. The distances in LEED pattern are dependent on the beam energy, but their ratio is constant. Using that information, a surface structure or a superstructure of the sample can be determined. Random surface impurities and defects affect the spot sharpness and background intensity.

Other surface features, that can be identified using LEED are regular step edges and facets. Regular array of step edges results in splitting of LEED spots at certain beam energies. Faceted surface creates a set of diffraction spots, that is centered around different point than the original LEED pattern, which can be clearly identified when continuously changing the beam energy.

2.4. Voltammetry

Voltammetry is an electrochemical technique used to study reactivity of species in aqueous environment. It provides information about chemical stability, reaction mechanisms or reversibility of reactions. Voltammetry has proven to be very convenient method for studies of corrosion or electrodeposited and self-assembled systems. It's also widely used in research of materials suitable for fuel cell electrodes, photoelectrochemical cell electrodes and catalysts.

2.4.1. Experimental configuration

In voltammetry, electrochemical current is measured as a function of applied voltage. At least two electrodes in a solution are needed for such measurements - the working electrode (WE, the studied analyte) and the counter electode (CE). However, in the two electrode setup, the ohmic drop in the solution and at the second electrode contributes to the resulting I-V curves (voltammograms). Although may be desirable in some cases when the whole cell is of interest, usually a three electrode setup is used in which only the effect of the analyte half-cell is measured. In the three electrode setup, the electrochemical current is still measured between the WE and CE, but the potential of the WE is measured with respect to the third electrode called reference electrode (RE).

The three electrodes are connected to a potentiostat, a simplified potentiostatic circuit is given in figure 2.10. The crucial part of the potentiostat is the comparator, which equalizes the potential difference E_m between the WE and RE to the desired value E_d given by the function generator. Any potential difference between E_m and E_d is immediately compensated by the current passing between CE and WE. The RE connection has very high input impedance so that no current passes between WE and RE.

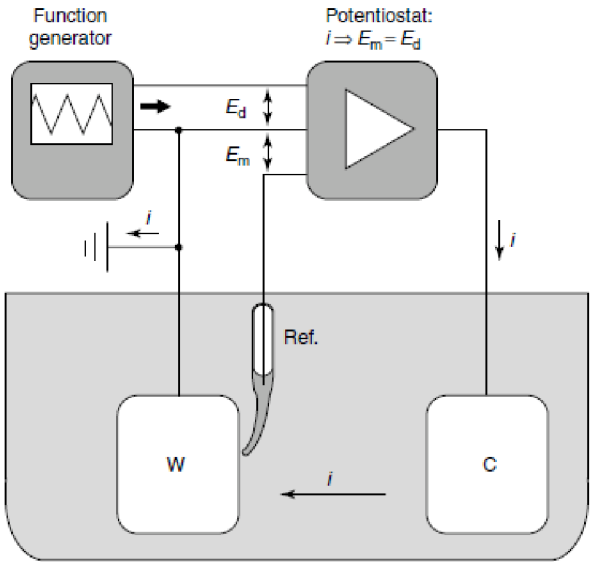

Figure 2.10: Basic potentiostatic circuit. E_d is the driving voltage, E_m is the measured voltage. Potentiostat equalizes those two by delivering current i. Picture reprinted from [51].

2.4.2. Principle of operation

Potential of an electrode, at which an electron transfer reaction takes place, is given by the Nernst equation

$$E = E^0 + \frac{RT}{nF} \ln \frac{a_{ox}}{a_{red}}, \tag{2.13}$$

where E is the half-cell reduction potential, E^0 is the standard half-cell reduction potential (tabulated for most half-cells), R is the universal gas constant, T is the temperature in K, n is the number of electrons transferred in a reaction, F is the Faraday constant and a_{ox}, a_{red} are the activities of the reactants. At low concentrations, the activity can be approximated by concentration.

The Nernst equation describes a relationship between the electrode potential and reaction products concentration. By varying the potential of the electrode, the product concentration changes. Varying the voltage can be done in many defined ways - based on that we distinguish between Linear Step Voltammetry, Linear Sweep Voltammetry, Cyclic Voltammetry or AC Voltammetry.

An important aspect of voltammetry measurements is the mass transport, because it changes the reactant concentration at the electrode. There are three basic ways of mass transport in the electrochemical cell - diffusion ($\propto$ concentration gradient), migration ($\propto$ potential gradient) and convection ($\propto$ pressure gradient). The measured current is always determined by the slowest process. The experiments are designed in such a way that there is one transport mechanism dominant and the others can be neglected.

2.4.3. Cyclic voltammetry

In cyclic voltammetry, the potential difference between WE and RE is linearly scanned in a given potential window (see figure 2.11). From the resulting voltammogram it can be determined at which potential the is reaction happening and whether it is reversible or irreversible.

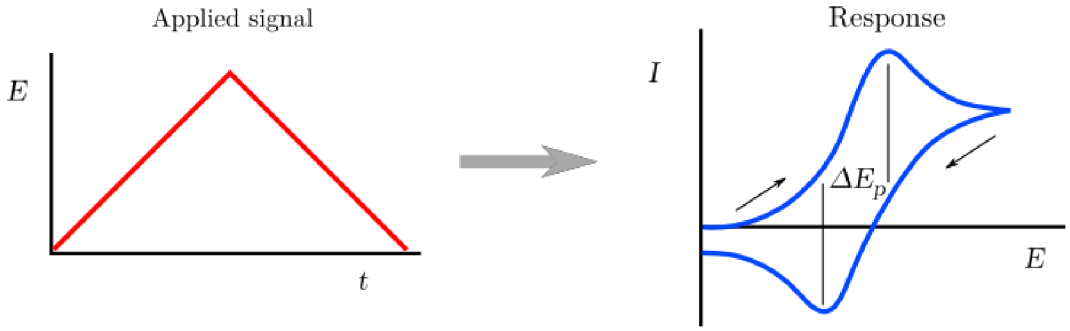

Figure 2.11: Principle of cyclic voltammetry. The voltage between WE and RE is scanned linearly back and forth, the current response is measured.

The reversibility of the reaction is determined by the ratio of the reaction rate and mass transport velocity. If the electron transfer process is much faster than the mass transport, then the Nerstian equilibrium is maintained at the electrode surface and the process is reversible. Two corresponding oxidation/reduction peaks can be seen in the voltammogram (see figure 2.11). A rule of thumb is that if the process is reversible, the potential difference between the two should not be higher than $59/n$ mV, where n is the number of electrons transferred in the reaction [52]. The heigths of the peaks should be commensurate.

If the reaction if irreversible, then the peak separation is much higher and the reduction peak is much smaller than the oxidation one. There is no definitive line between the reversible and irreversible reactions, the reactions between the well-distinguishable cases are called quasi-reversible.

Different reaction mechanisms (such as reversible electron trasfer followed by reversible chemical reaction, reversible electron transfer followed by an irreversible regeneration of starting material, etc.) produce different characteristic voltammogram shapes [52].

2.4.4. Hanging meniscus configuration

When only one crystal plane is of interest, a hanging meniscus configuration can be used. When using the sample as working electrode, it is necessary to wet only the crystallographically well-defined surface. That is achieved by lowering the sample surface-first slowly into the electrolyte and creating a hanging meniscus. To make the meniscus forming process easier, sometimes a syringe-like glass component is used to make a drop of electrolyte on the investigated surface before lowering it into the cell. That way, the risk of wetting the non-defined sides of the sample is minimized. The process in illustrated for sample aplicable for UHV studies as well in figure 2.12.

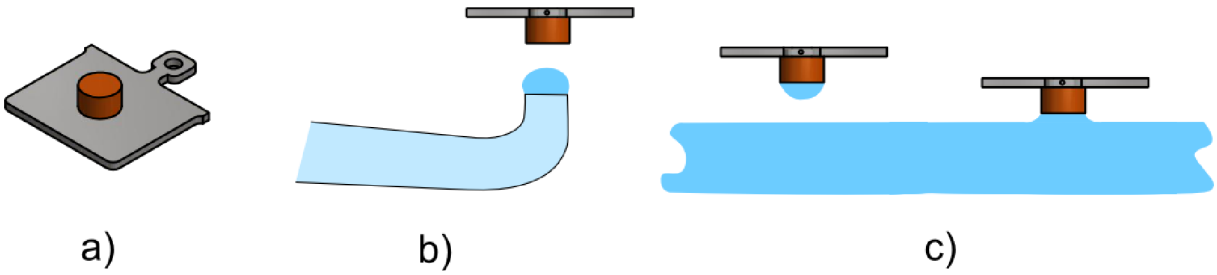

Figure 2.12: a) Cylindrical sample mounted on standard Omicron sample plate. b) Making a drop of electrolyte on top of the sample using a bent glass capillary. c) Lowering the sample with a drop into the electrolyte creates a meniscus.

2.5. Combining voltammetry with imaging techniques

Adding an imaging technique to the voltammetry setup is very convenient for determination of the reaction mechanism - at every point of the voltammogram the surface can be imaged and the surface changes can be directly assigned to the features observed in the voltammogram. There are two basic ways how to connect the two - either the scanning tunneling microscopy setup is moved directly to the electrochemical cell (in-situ EC-STM) or the electrochemical compartment is connected to an UHV apparatus, where the traditional methods of surface characterization take place.

2.5.1. In-situ EC-STM

In-situ electrochemical STM, sometimes referred to as just in-situ STM, is an STM operating in liquid environment under precise potential control. The scheme of common experimental configuration is given in figure 2.13.

The principle of STM imaging stays the same as in classical STM operated in UHV. There are however some adjustments - the most apparent difference is the tip. While in

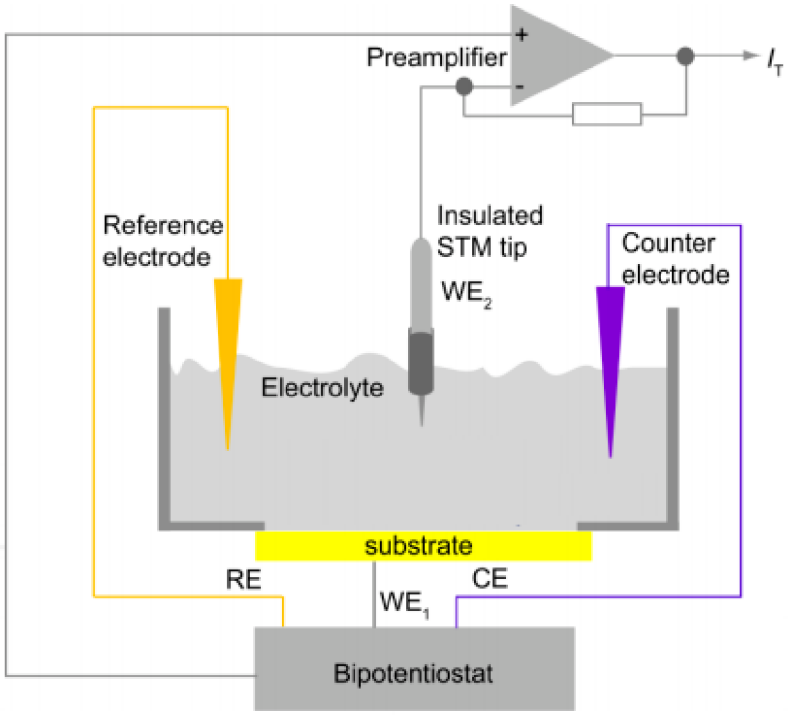

Figure 2.13: Setup of in-situ EC-STM, picture adapted from [53]

classical STM the tip is just a piece of wire with sharp end, in EC-STM the wire must be coated by an insulating material, so that the current passes only through the very tip, effectively minimizing the contribution of faradaic current. The second adjustment is that the bias voltage is given with respect to the RE - for the same reasons as in classical three electrode cell setup.

Liquid or air are much more complex environments than UHV and scanning in liquid is more demanding than scanning in UHV. Therefore the resolution achievable by EC-STM is generally lower than in classical STM.

2.5.2. Combined UHV-EC apparatus

Ultra-high vacuum environment offers surface characterization techniques, whose capabilities are unmatched in high pressure environment, such as STM, XPS or LEED. That is a clear advantage of choosing the combined UHV-EC apparatus for characterization of electrochemically prepared surfaces.

The disadvantage is that the electrochemical preparation is no longer as well-defined as in in-situ EC-STM. After the sample is put out of the liquid the precise potential control is no longer possible. While the transfer between electrochemical cell and UHV apparatus is taking place, the sample must be shielded from the ambient - otherwise species present in air adsorb, which deteriorates the quality of the prepared surface.

The combined UHV-EC apparatus serves as a bridge between classical surface science in UHV and the electrochemical approach. The motivation for using these setups is often to check the stability of structures well understood in UHV, but not tested in more complex environment or to image electrochemically prepared structures with high resolution.

3. The Design

This chapter deals with the design of the transfer system between ultra high vacuum and electrochemical environment (UHV-EC). General requirements on the system are summarized, a review of possible designs applicable for a specific UHV chamber is given, individual design features of the system are presented and discussed and lastly, test by measuring voltammetry of a known standard sample is carried out.

3.1. Motivation

Connecting the expertise in UHV with electrochemical surface science is a highly desirable, yet difficult task. The UHV surface science can provide the fundamental knowledge about the phenomena present on the well-defined surfaces and electrochemical surface science gives insight into the behaviour of those phenomena in conditions much closer to the real applications. Just the pressure gap of 14 orders of magnitude illustrates how far apart the worlds of those two branches of surface science are.

For both of the projects described in the Chapter 1, the plan is to study the samples both in UHV and in the electrochemical environment and to move the individual samples back and forth between those two. That way the effect of different preparation in UHV and in ambient does not play a significant role - a sample prepared by any method can be analyzed in both environments and the effect of different preparations can be well documented.

3.2. Requirements on the transfer system

In short, the transfer system must be able to provide fast and reliable transport of the sample between UHV chamber and electrochemical environment. At every stage of the transport, the sample should be sealed from ambient atmosphere. The samples used for UHV studies are mounted on standard Omicron sample plates, the transport and electrochemical measurement must be enabled witout the need of unmounting it.

There are three basic different types of experiments, that the transfer system must enable:

1. Sample preparation in UHV $\rightarrow$ exposure (or analysis) in EC cell attached to the UHV chamber $\rightarrow$ analysis in UHV.

2. Sample preparation and analysis in UHV $\leftrightarrow$ analysis by in-situ EC-STM (a different machine located in a different room).

3. Sample preparation by chemical cleaning $\leftrightarrow$ analysis in UHV.

The choice of materials must be consistent with the designation of individual parts. The vacuum part of the system must be mechanically robust, the materials used must comply with the standard requirements on UHV materials - that is, low desorption and high mechanical stability both at room temperature and at temperatures elevated up to 200°C (these properties can be summed in one word as "bakeability").

The components used for electrochemical studies are traditionally made out of glass. If there is a need for other materials, which are easier to machine, they used must be highly chemically stable - such as Teflon (PTFE), Kel-F (PCTFE) or PEEK. All the parts of the glass compartment that might come into contact with the sample or the electrolyte must be designed in a way that enables cleaning from organic contamination by boiling in nitric acid.

From the different cleaning methods of the UHV and EC parts, it is clear that the whole system must be easy to disassemble. Even for safety and convenience, it must be possible to easily dismount the glass compartment from the UHV chamber. The UHV chamber must remain fully functional both with the glass compartment mounted or dismounted.

3.3. The UHV chamber

The UHV chamber intended for the electrochemical studies is called Omega. Omega is based on a commercial Omicron UHV chamber equipped with Omicron STM microscope, XPS, ISS, LEED and mass spectrometer for residual gas analysis. A schematic drawing of Omega is shown in figure 3.1. Samples are loaded through the 5-way cross (highlighted by purple colour in the picture) in the sample storage mounted on the magnetic transfer rod. Then the load-lock is pumped and gate valve between load-lock and main chamber can be opened. In the main chamber, samples are transfered from magnetic rod to XYZφ manipulator (cyan colour in the picture) using a wobble-stick (part of the STM, blue colour). Cleaning by sputtering-annealing cycles, LEED (green) and XPS (red) measurements take place when the sample is mounted on this manipulator. When performing STM measurements, sample is transfered in the STM using a wobble-stick. Typical achievable base pressures are $p_{main} = 5 \times 10^{-11}$ mbar in the main chamber and $p_{LL} = 1 \times 10^{-8}$ mbar in the load-lock.

3.4. General concept of the transfer chamber

Protecting the sample from the air contamination can be done in several ways. For transfer between the UHV chamber and an electrochemical cell attached to it, argon or nitrogen atmosphere may be used. Although the glass compartment will never be tight enough to prevent contamination from going in, maintaining an overpressure of inert gas inside minimizes the amount. When transporting the sample betweeen the UHV chamber and in-situ EC-STM, sealing the sample surface from ambient air can be done by placing a drop of ultrapure water in agron or nitrogen atmosphere. Before the electrochemical experiment, the drop is rinsed off with ultrapure water.

In the following text, different designs of UHV-EC transfer system aplicable to the Omega chamber are briefly reviewed. The interested reader is referred to [54] for a more detailed review of possible designs of such systems.

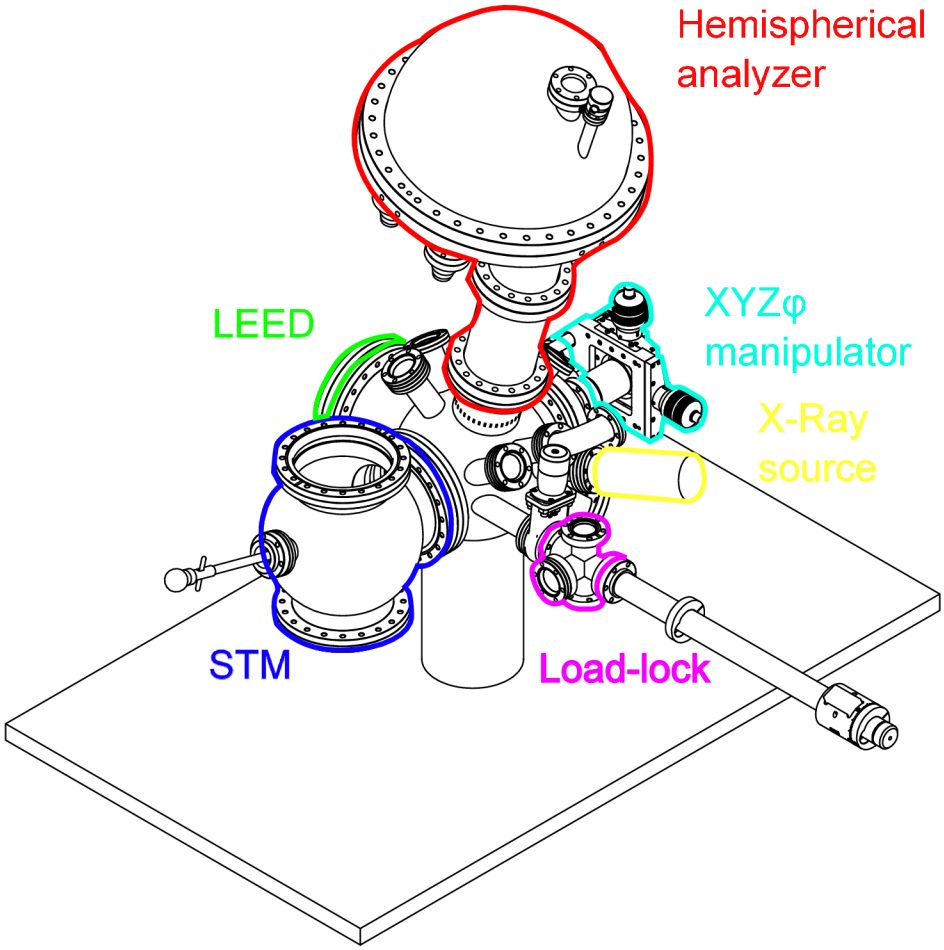

Figure 3.1: Approximate drawing of UHV chamber Omega.

3.4.1. In-plane vertical transfer

The first design is inspired by an UHV-EC transfer system used in group of prof. Klaus Kern at the Max Planck Institut for Solid State Research in Stuttgart. A design layout of EC cell attached to Omega chamber was created, see schematic sketch in figure 3.2.

In this design, the 5-way cross, which is already mounted on Omega, is used for attachement of the electrochemical cell. The vertical transfer to the cell is provided by a standard UHV manipulator with bellows, the remaining port in the 5-way cross is used as viewport. In addition to the current cross, a new 6-way cross is mounted right next to it. Through ports in this cross pumping, gauge and gas inlet are provided, while the last port is left for possible future needs.

This rather simple concept was however not recommended in a personal discussion with prof. H. E. Hoster (the author of [54]). The main reason being generation of metal micro-particles in bellows of the z-manipulator, which can consequently fall down to the electrochemical cell and affect the voltammetry results. This problem can be resolved in several ways. The simplest solution is just tilting the whole 5-way cross about 30°, which

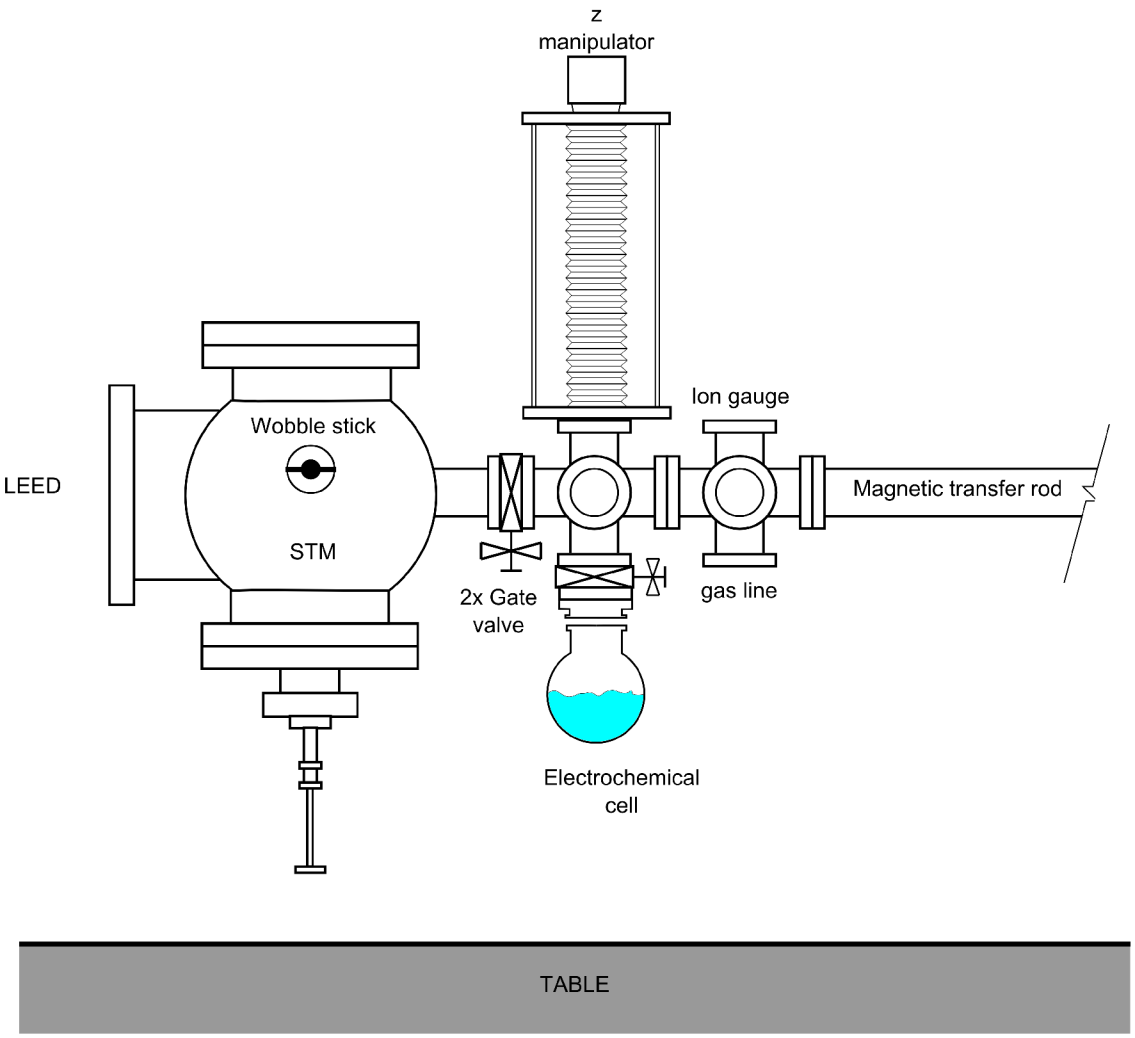

Figure 3.2: Design configuration with in-plane vertical transfer, front view.

would cause the microparticles to stop at the copper gaskets (see figure 3.3) and not fall to the electrolyte. However, problems might arise when engaging the hanging meniscus. Either when making the drop or when aproaching the electrolyte, precise control of the sample position is needed, which may be difficult in the tilted geometry. Also loading sample through the port, that is now facing downwards, would be uncomfortable. For those reasons, another design was proposed, described in the next section.

3.4.2. Out-of-plane vertical transfer

To solve the problem of metal micro-particles falling into the electrolyte another design was required. In the novel design, vertical transfer should be provided solely by parts made of glass or plastics. Some metal parts cannot be omitted (the sample plate, for example), but sliding metal-to-metal contact above the electrolyte should be avoided. The new design is inspired by the work of H. E. Hoster [54].

Sketch of the design adapted for the Omega chamber can be seen in figure 3.4. The 5-way cross currently present in Omega is replaced with a 6-way cross and a magnetic transfer rod is added to the new port. Apart from that, there are no changes to the load-lock. This design was later chosen for implementation, further details of the glass compartment and vertical transfer are discussed in section 3.5.2.

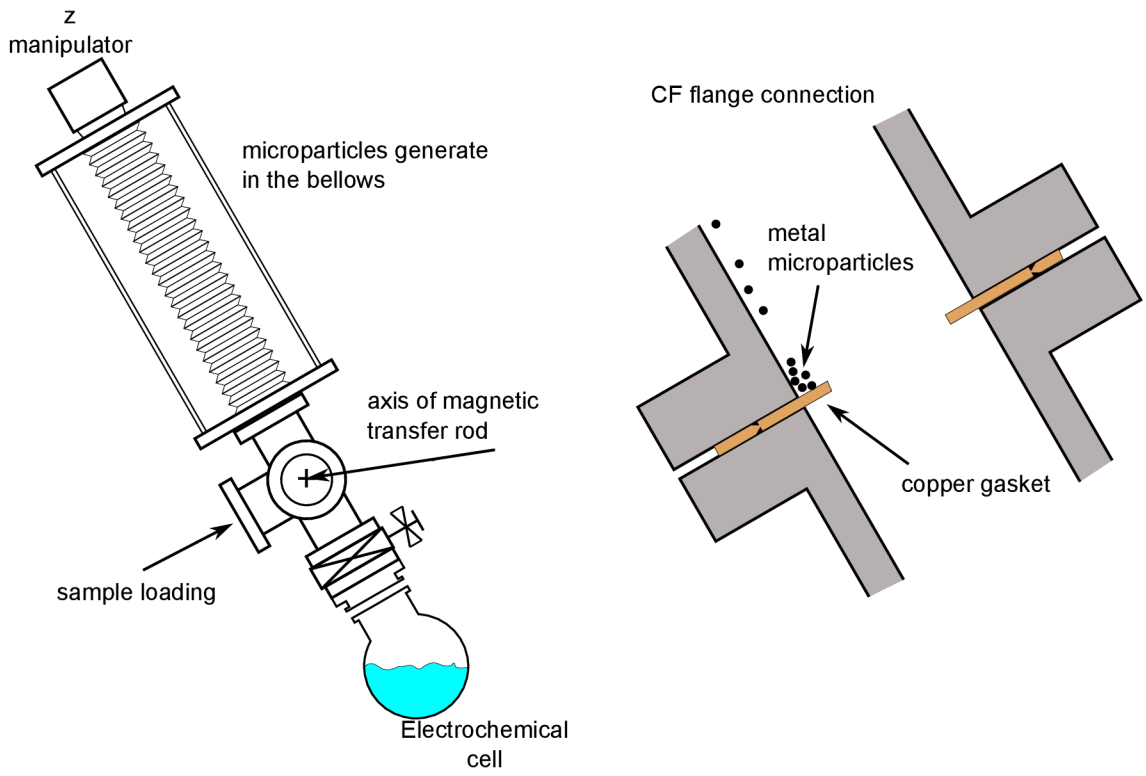

Figure 3.3: Design with in-place vertical transfer with tilted 5-way cross. Microparticles stop at the copper gaskets as the fall from the Z manipulator.

3.4.3. Flow cell

The third design considered for the Omega chamber is the so-called flow cell. In the flow cell design, the electrochemical cell is not a separate compartment to which the sample would be transfered, but it's a miniature mobile tube-like part, that is driven to the static sample. One of the possible designs of the miniature flow cell is in figure 3.5. Because the cell comes to the sample from below and only touches the sample via the hanging meniscus, there needs to be a constant pressure applied to the liquid in the cell to prevent breaking of the meniscus by evaporation of the liquid. To make that possible there is a constant flow of the liquid and the excessive electrolyte is collected in the outer tube, hence the name flow cell.

Because of the need for a relatively high volume of liquid directly in the load-lock chamber, a complicated construction of the cell with precise liquid pressure control and a need to provide electrical contact to the sample directly in the loack-lock chamber, the flow cell design was not further considered for Omega chamber.

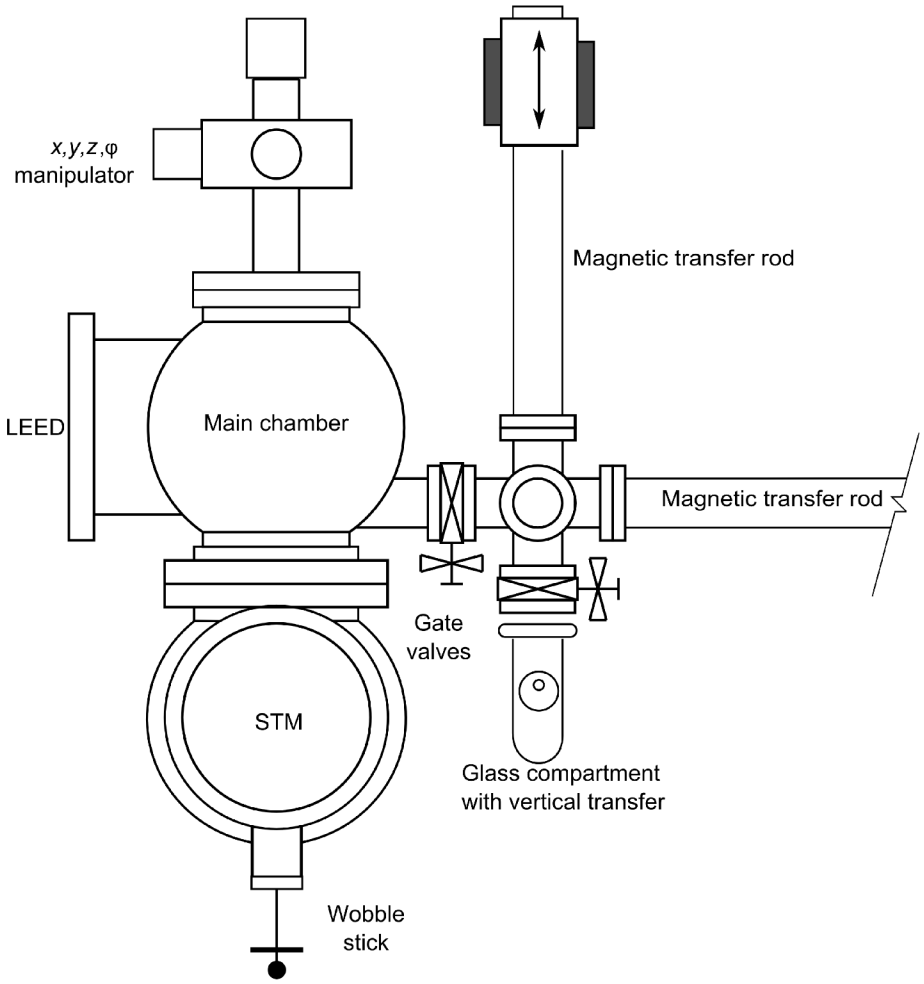

Figure 3.4: Design configuration with out-of-plane vertical transfer, top view.

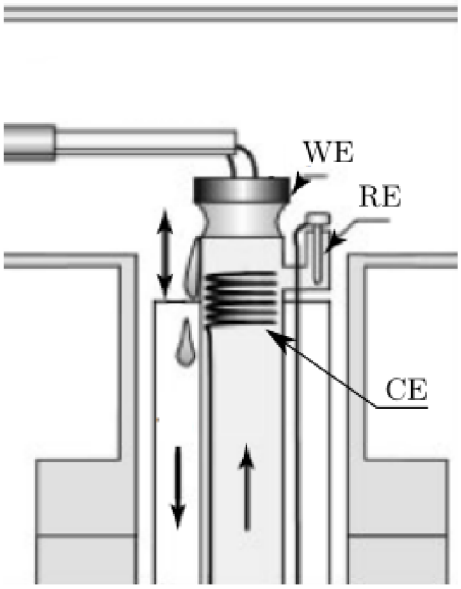

Figure 3.5: Sketch of the flow cell design. The glass tube is driven to the sample form below. Inner tube serves as an electrolyte feed, the excessive liquid is caught in the outer tube. Picture adapted from [54].

3.5. Design details

For the reasons mentioned in the previous section the design with the external electrochemical compartment and an out-of-plane vertical transfer was chosen. Individual features of the concept are discussed in this section.

3.5.1. Holder with locking mechanism

In the design with out-of-plane vertical transfer, a new sample holder is needed to transfer samples from sample storage on magnetic rod to vertical transfer in the glass compartment. Such a holder should be able to take samples from shelf-like storages, lock them, so they don't fall down and finally unlock them again when placed in the other shelf-like holder.

For this purpose a holder with locking mechanism was designed, depicted in figure 3.6. The locking is enabled by a slit, in which the ear of the sample plate is placed. Then the slit is turned 90 degrees, which results in locking the sample plate in place.

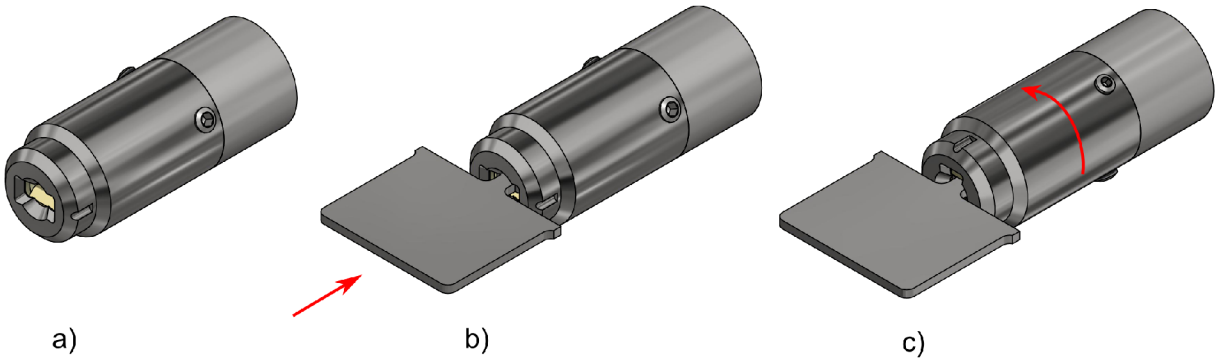

Figure 3.6: a) Holder with locking mechanism. b) Ear of the sample plate is inserted in the slit. c) The holder is turned 90 degrees, the sample plate is locked.

The holder is assembled from several parts, section sketch is in figure 3.7. There are two groups of parts - one that turns with the transfer rod (the outer shell, grey colour in figure) and one that moves with the sample plate (the inner part, yellow colour in figure). The inner part is needed to prevent the sample from moving in the locked position. The contact between the outer shell and inner parts is provided by stainless steel balls of 2 mm diameter, that are held in position by copper cage. That way, a ball bearing is made.

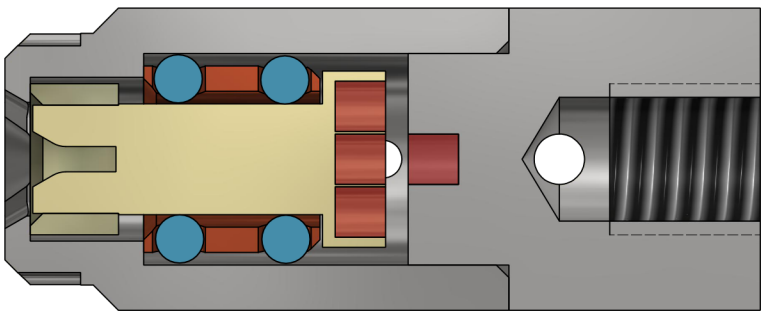

Figure 3.7: Section sketch of the holder. The grey parts move with the transfer rod, the coloured parts move with the sample plate (with exception of the red magnets in the outer shell). Contact between the outer shell and the inner part is provided by ball bearing made of stainless steel balls and copper cage.

Another point to address is the need for the inner part to stay in place when the sample plate is not present. If it was able to turn freely (as a consequence of vibrations, for example), it may become impossible to insert the sample plate, because the slits in the inner and outer parts could become misaligned. To prevent this, five magnets are used to press the inner part against the sample plate. The magnets tend to stay in certain stable position (see figure 3.8). That way any unwanted rotation of the inner part is prevented.

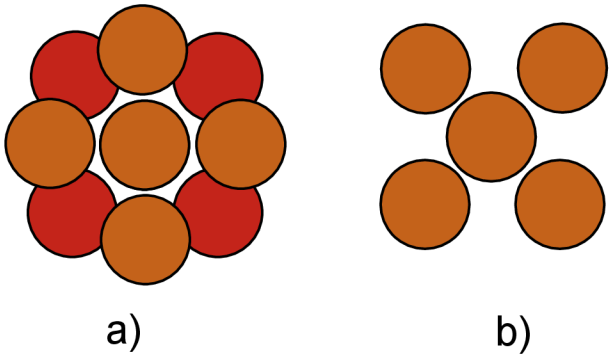

Figure 3.8: There are five magnets on both the outer shell and the inner part. The outer shell and inner part can rotate against each other. Nevertheless, it is energetically favourable for the inner part to stay in position, where the magnets are oriented as in picture a). Position b), where the red magnets are hidden behind the brown ones, is unstable. That way, stable positions are separated by 90° - locked and unlocked.

3.5.2. Glass compartment

A sketch of the glass compartment is shown in figure 3.9. The glass comapartment is connected to the load-lock by a KF flange. A jar with KF flange as well as the special plastic KF clamp and sealing ring was supplied by EVAC Vacuum company. Further details of the glass compartment design are discussed in following subsections.

Vertical transfer

The ports in the glass jar are NS 45/40 ground joints. The vertical transfer is provided by a glass capillary with an outer diameter of 6 mm, that slides in a hole drilled in a Teflon NS 45/40 stopper. For reasons described in following paragraph, the hole is not drilled in the centre of the stopper, but is shifted 7 mm away from it. A special sample holder made from PEEK is fixed to the glass capillary.

Off-centre design

The point of choosing this design configuration was to avoid sliding metal-to-metal contact above the electrolyte. That kind of contact must however surely be present in the holder with locking mechanism since both the holder and the sample plate are metal. While it is probably quite safe to assume that most of the generated microparticles would stay in the outer shell of the metal holder, it is better to be sure by moving this kind of movement away from the cell. That can be done by designing a plastic holder that could rotate excentrically in the off-centre hole of the Teflon stopper. Such a holder design is depicted in figure 3.10. It is designed to hold the sample plate with the possibility to insert the sample oriented both up or down. The sample oriented up is needed for the

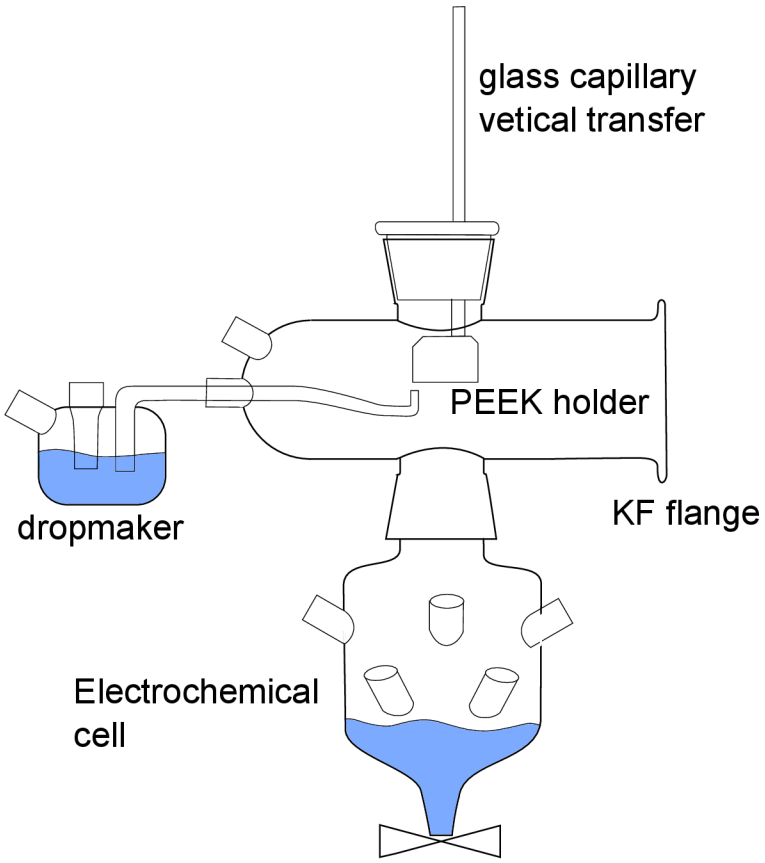

Figure 3.9: Overview of the glass compartment.

case of putting a drop of water on it to seal it, the sample oriented down is needed for the voltammetry measurements in the attached cell. The material chosen for this holder was PEEK for its chemical stability and mechanical properties. The sample is inserted with the holder with locking mechanism, then the PEEK holder is turned around the axis of the capillary. Then it is in the reach of the drop maker and can consequently be lowered to the cell.

Contacting the sample

The only place where the sliding metal-to-metal contact above the cell cannot be omitted is the spot where the sample plate must touch the wire that provides electric contact to the sample. While it cannot be moved away from the cell, it can at least be hidden in a groove, so that any generated microparticles don't fall down immediately. For that reason the $Pt_{0.8}Ir_{0.2}$ wire is placed in the groove at the side of the sample plate. There are two wires touching the sample plate - one in each groove. That gives the possibility of performing a quick check of the electrical contact by just measuring the resistance between the two wires before lowering the sample plate to the EC cell. In addition to providing electrical contact, the wires also work as soft springs to create a little friction, so that the sample plate cannot move much (as a consequence of vibrations, for example). A photo of the contacted sample plate in PEEK holder is in figure 3.11.

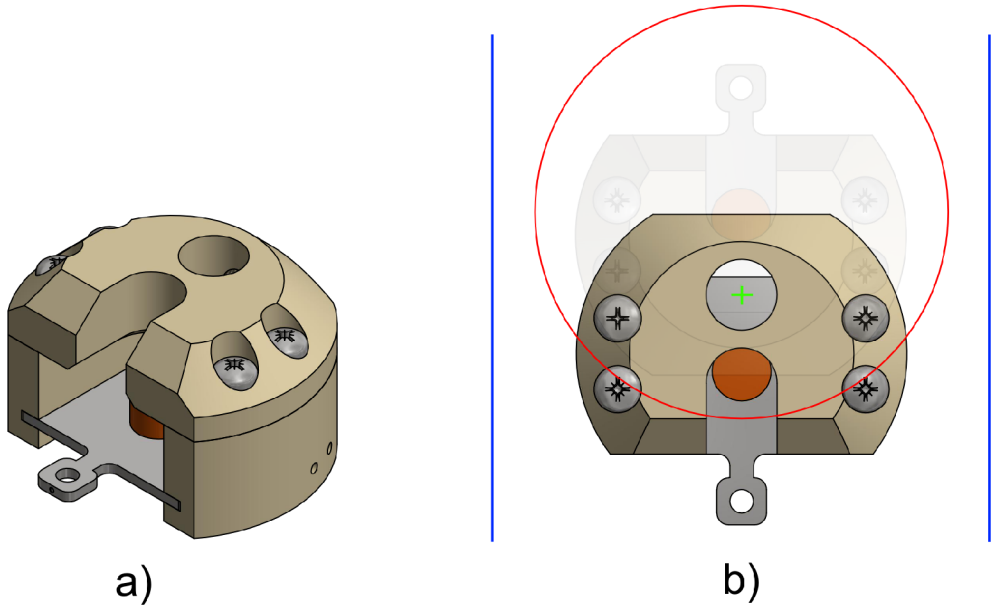

Figure 3.10: Sample holder made of PEEK. The sample plate can be inserted facing both up or down while being in reach of the drop maker. In picture b) the off-centre design is highlighted. Axis of rotation is the green cross. The blue lines indicate the inner tube of the glass jar (diameter 42 mm), the red circle is inner diameter of both NS ground joints used for the vertical transfer (35 mm). It can be seen, that the place where the sliding metal-to-metal contact would take place is not directly above the cell (red circle is approx. 5 mm away from the ear). Then the whole PEEK holder is rotated and can be lowered through the NS ground joint (red circle) to the cell.

EC-cell

The first prototype of the cell itself is made from a glass tube with an NS ground joint on one side and narrow part with a valve on the other. Eight ports are attached to the tube, two of them being plain GL 18, two GL 18 with a needle valve, three GL14 and one ball joint. Rough sketch of the cell is in figure 3.12. One of the GL 18 with a needle valve has an inside capillary that goes under the intended level of electrolyte. This is used to bubble the fluid with gas to deaerate it. The other GL 18 with a needle valve is intended as a gas intlet above liquid level. The electrodes are going to be inserted through the GL 18 as well, the same for filling the cell with electrolyte. The single ball joint is used for the standard gas out bubbler. The remanining three GL14 have currently no function and are kept for possible future needs.

Drop maker

The drop maker is used to create a drop on the sample surface. For different experiments (measuring voltammetry or sealing the surface from ambient air), the possibility to create a drop on the sample facing both up and down is needed. Photo of designed drop maker is shown in figure 3.13. The valve is intended for filling the drop maker with ultrapure water and for providing a gas outlet when the water is being deareated by N_2 or Ag gas bubbling. A plastic syringe is used to apply pressure, which results in creating a drop on the pipette-like end of the drop maker. It is questionable whether it is more convenient to apply pressure above the level of the liquid or below (which means, whether the syringe should be filled with liquid or with gas). While filling the syringe with water and applying

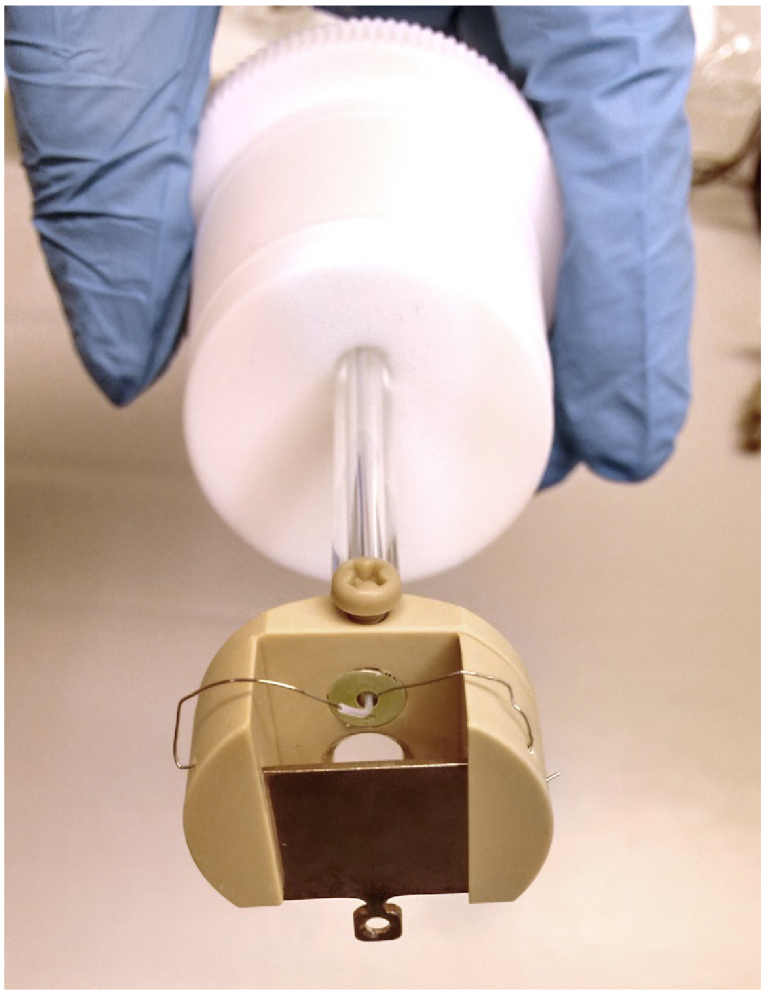

Figure 3.11: The place of contact between the PtIr wire and the sample plate is hidden in a groove. Two wires are used to contact the sample, isolated from each other by a teflon sleeve. Before performing any voltammetry measurement, the resistance between the two wires is checked to see, whether the electrical contact with the sample is estabilished.

pressure below the level might provide better control of the drop size due to incompressibility of liquid, the fact that the plastic syringe and connecting tube cannot be cleaned properly by boiling in nitric acid speaks against it. For this reason, it might be better to apply the pressure above the liquid, so that the syringe would only be in contact with the gas and not the liquid itself. For this reason, two GL14 ports were designed on the dropmaker, one with the tube going into the liquid, the other one without it to test both possibilities.

For making a drop on the sample surface facing up, originally a different piece of drop maker was intended. It turned out, however, that having those two GL14 ports and a valve enables us to rotate the dropmaker freely and having the possibility to apply pressure both above and below the liquid in the rotated case as well. Therefore there is no need for another drop maker.

3.5.3. Gas supply

The glass parts cannot be pumped to UHV. To protect the sample from atmospheric contamination, argon or nitrogen overpressure is used. Because the gas available in the

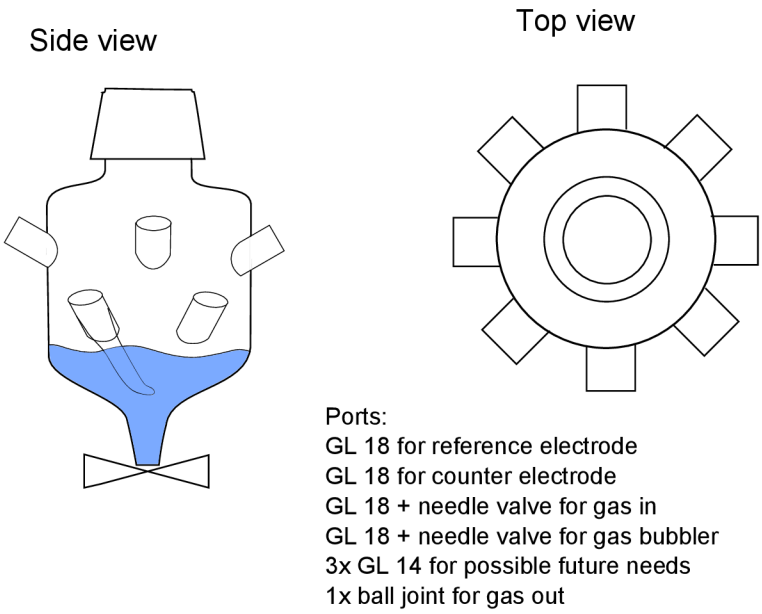

Figure 3.12: Side and top view of the electrochemical cell.

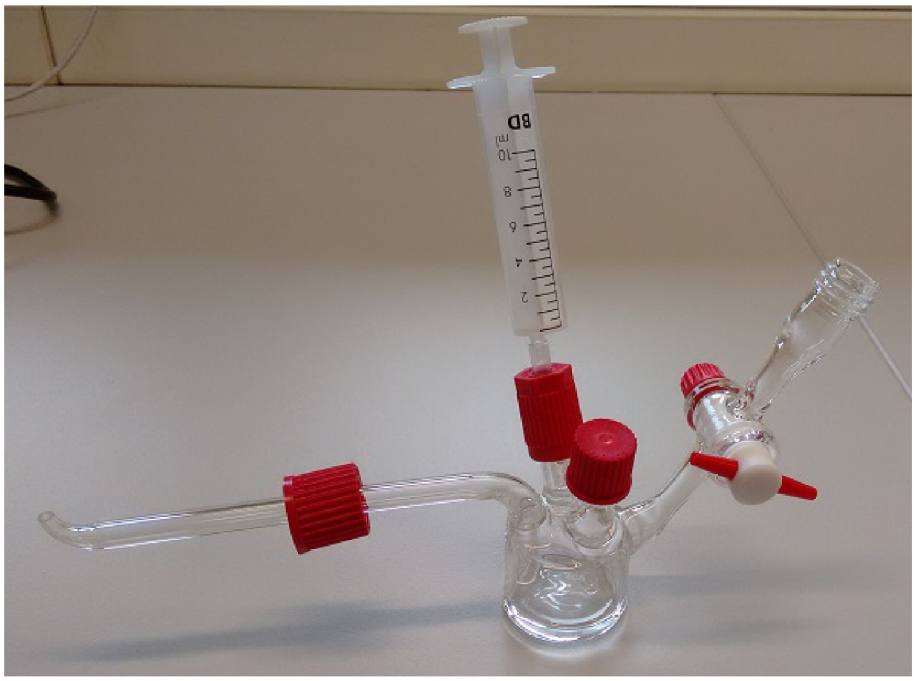

Figure 3.13: Photo of a drop maker. Drop is created by applying pressure by the plastic syringe. The two GL14 ports are intended to test whether it is better to apply pressure with gas-filled syringe or liquid-filled syringe. Therefore one of the ports has a glass tube, that goes below the level of liquid. Valve on the right is used to fill the drop maker with liquid and to provide gas outlet, when the liquid is being deareated.

lab is only 5N grade, a gas purifier was purchased. However, by the date this thesis is submitted, it was not installed yet due to the ongoing maintenance of the Omega chamber and a lack of lab time. A sketch of the current Ar or N supply system is in figure 3.14. The venting line for the load-lock was already present on the chamber. What is added as a part of the transfer system are the two lines for supplying the gas to the glass compartment. The first is for creating overpressure in the compartment and the

second is for deaerating the electrolyte by bubbling the gas through. The electrolyte in the dropmaker is bubbled through the drop-making tube.

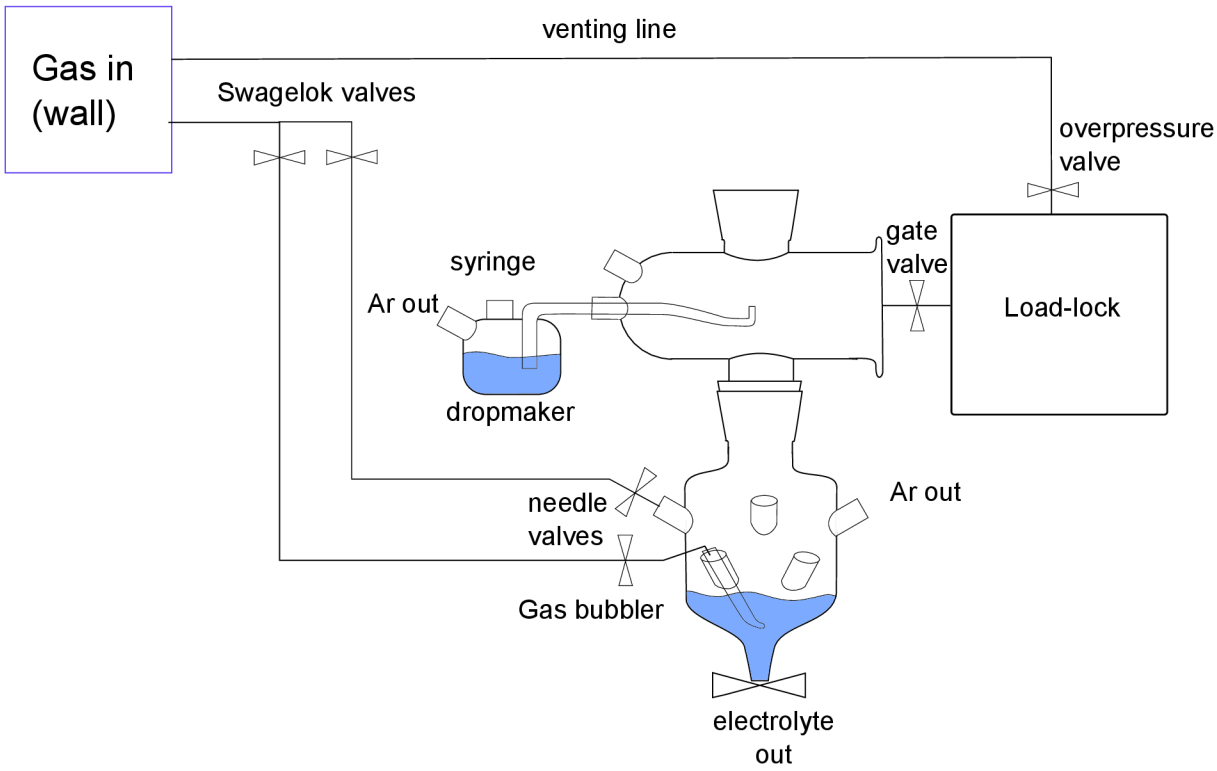

Figure 3.14: Overview of the glass compartment with gas supply.

3.5.4. Load-lock pumping and venting system

Several changes needed to be made on the load-lock pumping and venting system. First of all, a zeolite cryo trap was installed on the load lock. A great advantage of the cryo trap is its efficience for pumping water vapours, which are expected to be the main contaminants of the load-lock after electrochemical experiments. Cryo trap pump is also very clean, which makes it ideal for this cause as it does not produce any oil traces.

The second significant change in the Omega load-lock is the N_2 venting line. Originally, the venting line was not connected directly to the load lock, but ended behind the turbo pump rotor. The flow of the venting gas then went through the turbo pump to the load lock and caused the carbon contamination by backing pump oil traces. After the venting line was connected directly to the load lock, the carbon contamination level of the samples transfered from the load lock to the main chamber was lowered significantly, see section 4.2.4.

The work on changes to the load-lock pumping and venting system was done by Ing. Jan Balajka.

3.6. Testing the system

Transfering the sample from the load lock to the glass compartment and electrochemical cell was tested several times without greater difficulties. Problems sometimes occur with specific sample plates, that are a little thicker or whose surfaces or edges are corrugated.

They tend to get stuck in the holder with locking mechanism. Apart from that, sometimes it happens, that the electrical contact between the sample plate and the PtIr wires is not estabilished. In case this happens, it is usually sufficient to just press the sample plate further into the PEEK holder using the transfer rod. Creating a drop and lowering the sample in the cell is usually without any problems.

Voltammetry measurements on a known sample were made to the functionality of the electrochemical cell. The sample measured was Au(111) surface immersed in 0.1M H_2SO_4 [55], measured in $0.08 - 1.25\,V$ potential window vs. reversible hydrogen electrode (RHE).

In the first try, the cell was not boiled in nitric acid, because at that time that there was no available beaker big enough to fit the cell in. Instead, the cell was only sonicated in Extran M02 detergent solution, so certain level of contamination is expected. Results can be seen in figure 3.15. The slight tilt of the voltammogram can be attributed to the fact that one side of the bead crystal was slightly melted. This tilt is present in all the voltammograms measured on this particular crystal in other cells as well, therefore it is believed to be a property of the crystal, not the measurement conditions. The peak at 0.5 V in the forward scan is the only feature that should not be present in the voltammogram. Since the cell was not cleaned properly, this peak can be attributed to residual contamination.

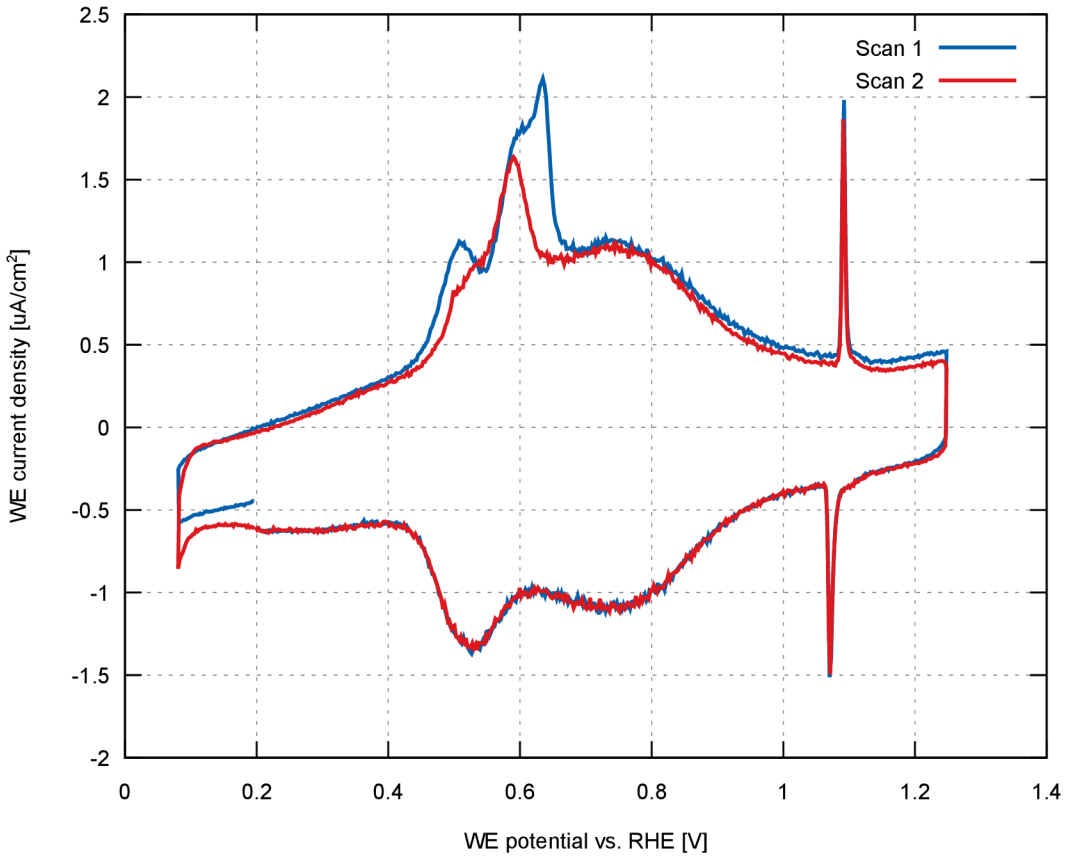

Figure 3.15: Voltammetry measurements on a known standard sample, Au(111) bead crystal in 0.1 M H_2SO_4. The slight tilt of the voltammogram can be attributed to the fact, that one side of the bead crystal was slightly melted.

4. The Experiments

4.1. Experimental apparatus

The experimental work of this thesis has been done on two different UHV chambers. The UHV-regime experiments (that is, experiments featuring low water doses) have been measured on a chamber called RT-STM. The experiments studying the effect of liquid water on the surface have been performed on the Omega chamber with attached UHV-EC transfer system described in chapter 3.

4.1.1. RT-STM chamber

RT-STM is a twin-vessel UHV chamber consisting of a preparation chamber with base pressure $< 1 \times 10^{-10}$ mbar (measured by a cold emission ion gauge) and an analysis chamber with base pressure $< 7 \times 10^{-11}$ mbar (measured by a Bayard-Alpert gauge). The analysis chamber is equipped with an Omicron μ-STM operated in constant current mode, a commercial ErLEED setup, a VG Microtech dual-anode x-ray source and a Specs EA 10 Plus hemispherical analyzer operated in constant analyzer energy mode.

Samples are prepared in a preparation chamber sputtering and annealing. The annealing step is done either in UHV or in O_2. Temperatures are measured with a K-type thermocouple attached to the sample holder. Because the thermocouple is not attached directly to the sample, the temperature readout can be up to 50 K too low at high temperatures. Up to 300° C, a systematic uncertainty of the given temperatures of approximately ±20 K is possible.

Adatoms are deposited on the surface by Omicron e-beam evaporator in the preparation chamber. The deposition rates are measured using watercooled quartz crystal microbalances (QCM). The adatom coverage given by QCM can be checked against estimates from STM images where counting of atoms is possible.

Water used for the experiments is prepared by Milli-Q Integral Water Purification System. The purification processes involve successive steps of filtration and deionization to achieve a purity expediently characterised in terms of resistivity (typically 18.2 MΩ·cm at 25° C). Water purified by this system is referred to as ultrapure water in this thesis.

The H_2O vapour is dosed from a glass beaker welded to a UHV compatible CF flange and filled with ultrapure water. The water was further cleaned by several freeze-pump-thaw cycles. Dosing is done by backfilling the preparation chamber. Water vapour pressure near the sample can be locally enhanced by using a shower-shaped component, which is moved close to the sample and through which the vapour is dosed. The enhancement factor of this component is estimated to be roughly 20–30, based on the ratio of the area of the ”shower” and the tube, where the gauge is located.

4.1.2. Omega chamber

Omega is a single-vessel UHV chamber. Some properties of Omega as well as a schematic drawing have already been given in chapter 3 of this thesis. The achievable base pressure of Omega analysis chamber is 5×10^{-11} mbar. Omega is equipped with Omicron STM1 operated in constant current mode, a Specs ErLEED setup, a VG Microtech dual-anode x-ray source and a Specs Phoibos 100 hemispherical analyzer operated in constant analyzer energy mode.

Sample preparation by sputtering/annealing takes place in the analysis chamber. Temperatures are measured by K-type thermocouple attached to the sample holder. Because the samples used for liquid water experiments have cylindrical shape with height of 5 mm, the temperatures on the sample surface are significanty lower than the thermocouple readout. At high temperatures the difference between the two can be as high as 150 °C, during typical preparation of magnetite (001) surface, the thermocouple readout is 700 °C while the surface temperature measured by pyrometer is approximately 550 °C).

Adatoms are deposited on the surface by an Omicron e-beam evaporator in the analysis chamber. The deposition rate is measured by a QCM, the same rules apply as in RT-STM.

4.2. Fe_3O_4(001) adatom template stability in ambient

4.2.1. Sample preparation

The SCV surface of Fe_3O_4(001) surface can be reproducibly prepared by sputtering (1 kV, 2 μA, 20 min) and annealing (900 K, 20 min) cycles in UHV with the last annealing step in O_2 ($p_{O_2} = 1 \times 10^{-6}$ mbar, 900 K, 20 min). The number of necessary sputtering/annealing cycles may vary depending on how many impurities are present on the sample. Usually only units of cycles are needed, but in some cases (after experiments with Pt adatoms, for example) the number may rise to 15–20. In that case, it is recommended to do the O_2 annealing step every 5–10 cycles to prevent excessive reduction of the surface. The annealing step in O_2 leads to regrowth of many new layers of pristine SCV surface. When this step is omitted or done only for a short time, characteristic defects appear on the surface or the surface is reduced to the Fe-dimer termination [11]. It is important that the cooling after the O_2 annealing is done in UHV and not in O_2, otherwise the surface will be covered with many small islands of pristine surface. The interested reader is referred to [11] for further information about the characteristics about the SCV termination and the metastable Fe-dimer surface termination of Fe_3O_4(001)

4.2.2. Pristine Fe_3O_4(001) surface

The pristine SCV surface can be easily recognized as it features characteristic undulating rows in the empty states STM image. The ”wide” and ”narrow” sites can be identified on the undulating rows (figure 1.2). The rows are perpendicularly oriented on each neighbouring layer (see figure 4.1). The visible atoms forming the rows are irons. Even though oxygens are topographically on the same level as the irons, they have very low density of states in the vicinity of the Fermi level, so they cannot be detected in empty states STM [6]. With the typical ”every day” resolution the single Fe atoms in the rows cannot be resolved and the protrusions consist of Fe dimers. The true single-atomic resolution shown in figure 1.2 is achievable only occasionally with a very good tip.

There are some characteristic defects that are always present on the freshly prepared surface and whose appearance is well documented [11]. By the labels in figure 4.1, there are:

Surface hydroxyl groups (labeled OH) are the most common defects on the SCV surface. They are easily distinguishable, because they exhibit characteristic hopping between the Fe rows over the narrow site at room temperature. The H bonds to one of the O atoms in the narrow site and forms a hydrogen bond to the other symmetrically equivalent O on the other side of the narrow site. The OH is not directly detected by STM, but its presence changes the density of states of the nearest Fe, which then appear brighter. The origin of the surface hydroxyl groups is most probably in the H_2O present in the residual gas, which reacts with surface oxygen vacancies.

Anti-phase domain boundaries (labeled APDB) appear, when the SCV reconstruction formed from different nucleation sites with different phase meet. When annealing above $\approx 750\,\mathrm{K}$ the $(\sqrt{2} \times \sqrt{2})\mathrm{R}45°$ reconstruction is lifted and when the sample consequently cooles down, the reconstruction starts forming at places where the needed temperature is reached sooner. Anti-phase refers to the fact, that that on the phase boundary the regular fashion of alternating narrow and wide sites is broken and there are two wide or narrow sites next to each other.

Stationary wide site defects resemble a pair of surface OH groups, but don't exhibit the hopping characteristic for the hydroxyls. These defects are most probably unreconstructed unit cells with filled cation vacancies.

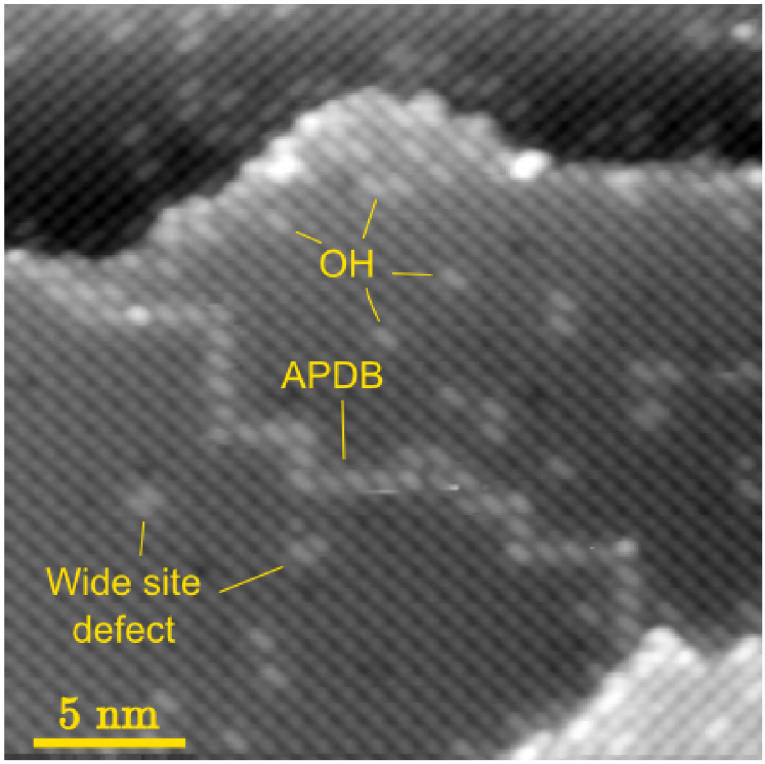

Figure 4.1: Typical STM image ($V_{sample} = 1.2\,\mathrm{V}$, $I = 0.2\,\mathrm{nA}$) of the $Fe_3O_4(001)$ surface after preparation. The undulating rows are oriented perpendicular to the rows on neighboring terraces. The characteristic defects (surface hydroxyls, anti-phase domain boundary and stationary wide site defects) are labeled.

4.2.3. Ag/Fe_3O_4(001) adatom array

The behaviour of Ag adatoms on Fe_3O_4 has been described in detail in the previous work at the Institute of Applied Physics, TU Wien [7]. Silver adatoms deposited on the Fe_3O_4(001) surface occupy exclusively the narrow site when their coverage is lower than 0.33 ML (one monolayer is defined as one adatom per unit cell, 1.42×10^{18} atoms/m^2). The adatoms exhibit limited mobility along the Fe undulating rows, possibly this mobility is partially tip induced.

The cluster formation is kinetically hindered by the instability of dimers. In low coverages, whenever a dimer is formed, it breaks up eventually and the excessive atom is distributed to a neighboring "narrow" site along the row. The clusters start to nucleate when two dimers meet and create a trimer. Small clusters have been observed at room temperature at coverages higher than 0.5 ML.

The interested reader is referred to [7] for more information about the Ag/Fe_3O_4(001) adatom array and its cluster nucleation mechanism.

4.2.4. Stability studies of the clean Fe_3O_4(001) surface

The $(\sqrt{2} \times \sqrt{2})$R45° SCV reconstruction is thermodynamically favoured in UHV conditions. Although deposition of Fe induces formation of single unreconstructed unit cells, to date it has not been shown that deposition of Fe could completely lift the reconstruction and create a (1×1) surface. Instead a metastable Fe-dimer termination is created with higher doses of Fe [56]. Adatoms of ferrite forming metals can be incorporated in the surface, filling the cation vacancy and locally lifting the reconstruction [21].

Complete lifting of the $(\sqrt{2} \times \sqrt{2})$R45° reconstruction with H_2O adsorption has been reported with dosing of formic acid [57], atomic hydrogen [58] and water [59]. The results after water dosing were however not consistently reproducible in our group.

For the development of Fe_3O_4(001) based single atom catalyst for real applications, it is crucial to investigate this subject further and experimantally determine the limits of stability of the $(\sqrt{2} \times \sqrt{2})$R45° reconstruction.

Effect of the pumping and venting system

Before the UHV-EC transfer system was utilized, the stability of the $(\sqrt{2} \times \sqrt{2})$R45° reconstruction was tested by just venting the Omega load-lock chamber with N_2 with the freshly prepared sample in. As will be shown, the pumping and venting mechanism plays a major role in the stability studies. In this section, the difference between the old pumping system (venting line through turbo rotor, rough pumping by a rotary pump) and the new system (venting through a separate line directly to the load-lock, rough pumping by a cryo trap) is investigated and its effect on the $(\sqrt{2} \times \sqrt{2})$R45° surface reconstruction is shown. LEED patterns after transfer to the vented load lock are shown in fig 4.2. It is clear, that the $(\sqrt{2} \times \sqrt{2})$R45° spots are gone after the treatment with the old system, but they are preserved after the same treatment with the new system.

XPS analysis reveals high carbon signal and significant hydroxylation (indicated by the shoulder on the O1s peak) after the treatment with old system, see figure 4.3. With the same experiment performed with the new system, the carbon contamination is minimized.

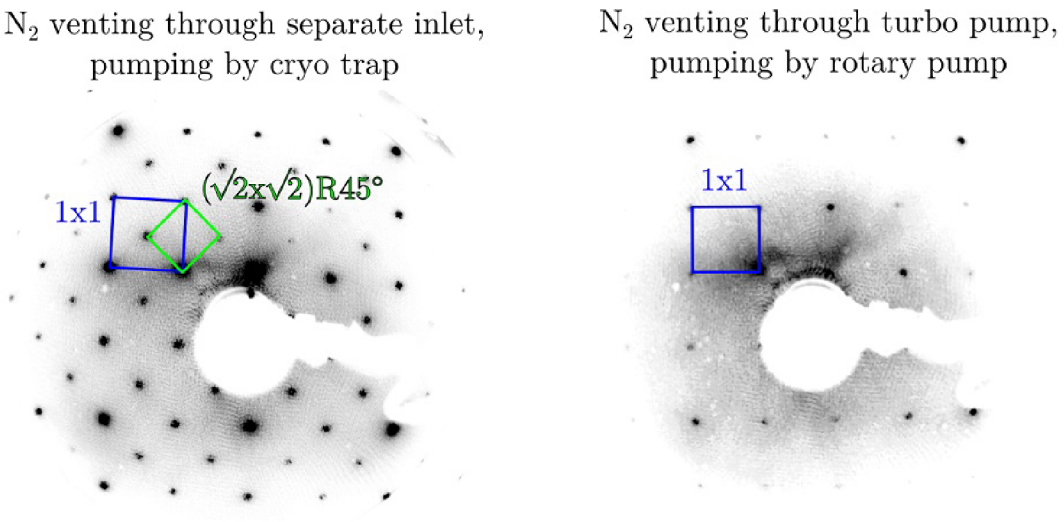

Figure 4.2: LEED patterns of clean Fe_3O_4(001) after exposure to atmospheric pressure of N_2. Using the old pumping system with rough rotary pump and venting line going through turbo, the reconstruction is lifted (right). With the new system using cryo trap for the rough pumping and separate gas line for venting, the reconstruction survives the high pressure.

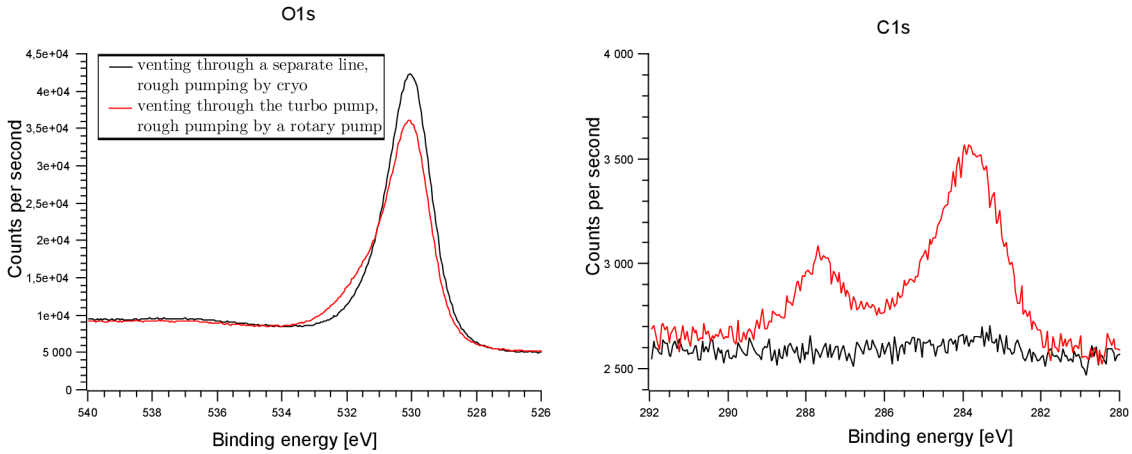

Figure 4.3: XPS analysis of clean Fe_3O_4(001) after exposure to atmospheric pressure of N_2. Using the old pumping system with rough rotary pump and venting line going through turbo, high carbon contamination is present and the oxygen peak is slightly attenuated. With the new system using cryo trap for the rough pumping and separate gas line for venting, the carbon contamination is minimized, oxygen signal is higher and with less hydroxylation (O1s peak shoulder is less pronounced).

Exposure to air and liquid H_2O

The experiments with liquid H_2O were carried out in the Omega chamber. Sample was prepared in the main chamber, then it was transfered to the load lock, which was later opened to the atmosphere. A drop of ultrapure water was put on the sample using a regular pipette.

After the load lock was closed again and pumped down, the sample was analyzed by LEED, STM, and XPS.

The LEED patterns before and after exposure to liquid H_2O are shown in figure 4.4. It is clear, that the $(\sqrt{2} \times \sqrt{2})$R45° symmetry is still present after the high pressure treatment.

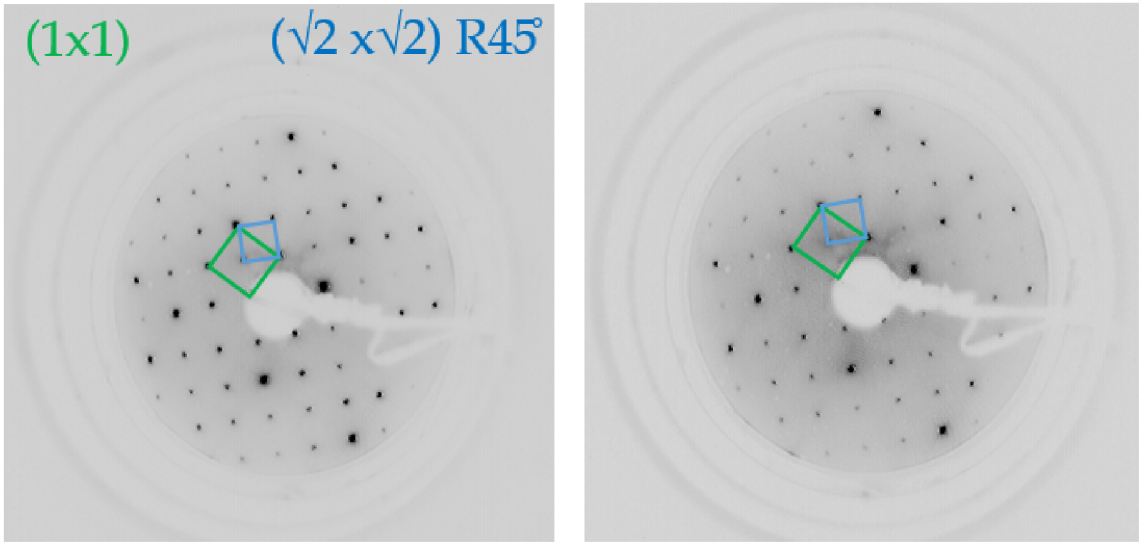

Figure 4.4: LEED patterns of clean $Fe_3O_4(001)$ before and after exposure to air and liquid water. The patterns were taken with beam energy of 90 kV.

STM images before and after exposure to water are shown in figure 4.5. The surface is very difficult to scan after the exposure. Fast fourier transform (FFT) of acquired images shows weak spots of the $(\sqrt{2} \times \sqrt{2})$R45° reconstruction.

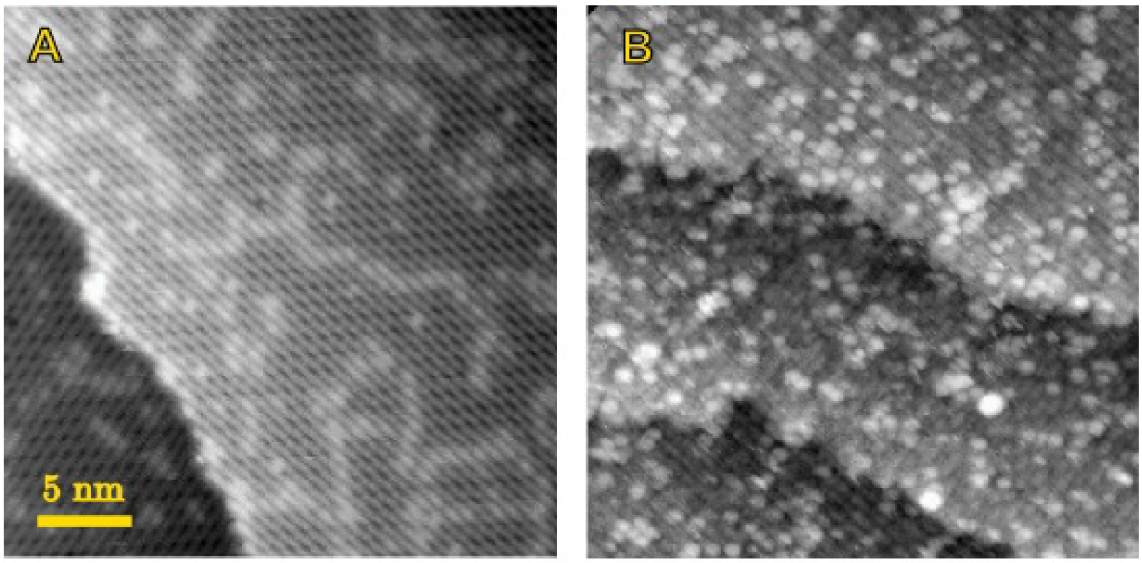

Figure 4.5: STM images of clean $Fe_3O_4(001)$ before and after exposure to air and liquid water.

Analysis by XPS reveals hydroxylation of the surface (indicated by the ”shoulder” of the oxygen peak) and slight carbon contamination (see figure 4.6).

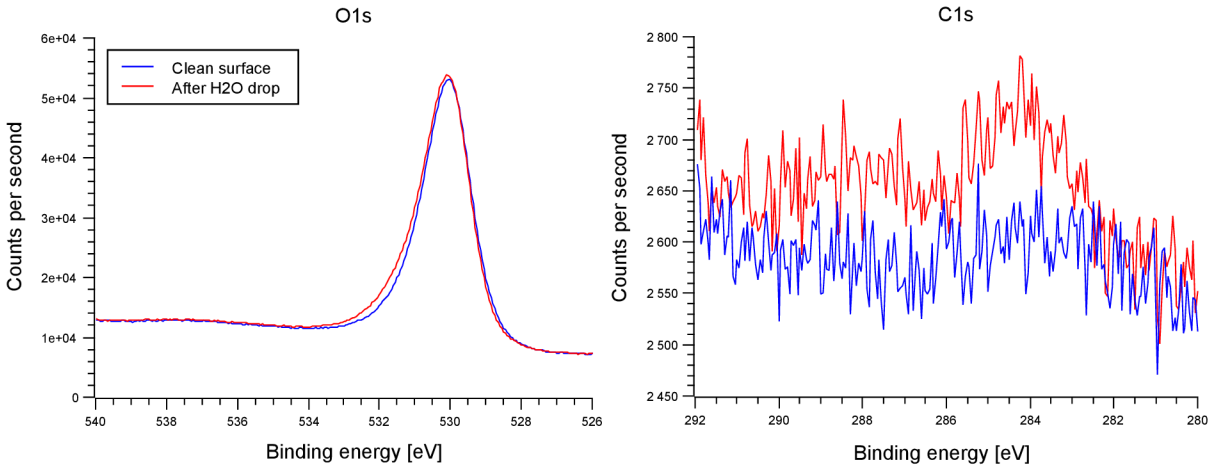

Figure 4.6: XPS analysis of the surface before and after exposure to air and liquid H_2O. The shoulder on the O1s peak indicates hyroxylation of the surface. The C1s peak, almost non-existent on the clean surface, is much higher on the surface after exposure to air and water.

Exposure to inert gas and liquid H_2O

In this experiment, the sample was prepared in the Omega chamber, then transfered to the load-lock, which was later vented with inert gas. The drop of ultrapure water was placed on top of the sample using the dropmaker in the glass compartment setup. The LEED analysis of the sample after this treatment still shows weak $(\sqrt{2}\times\sqrt{2})R45°$ reconstruction spots (see figure 4.7. The carbon signal measured in XPS is similar to the one measured in the previous experiment after exposure to air and liquid H_2O. The hydroxylation of the surface is higher compared to the previous experiment (see figure 4.8).

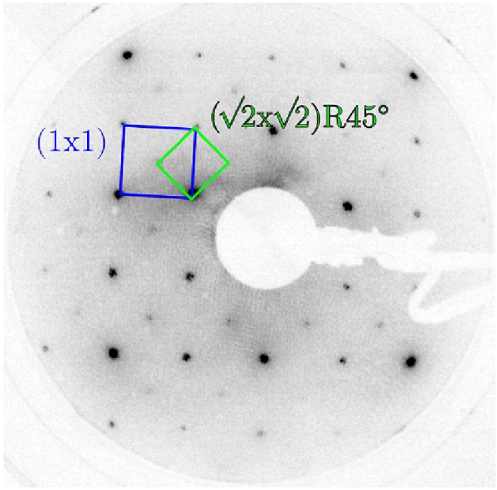

Figure 4.7: LEED pattern of the clean $Fe_3O_4(001)$ surface after exposure to inert gas and liquid water. The reconstruction spots are visible, but very weak.

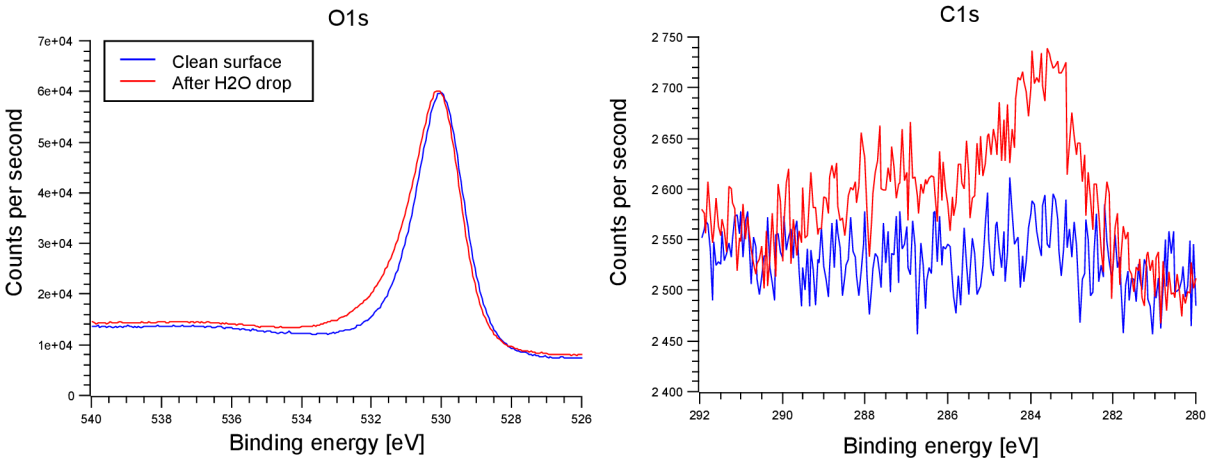

Figure 4.8: XPS analysis of the surface before and after exposure to inert gas and liquid H_2O. The shoulder on the O1s peak indicates hyroxylation of the surface, which is higher compared to the experiment with air and liquid H_2O exposure. The C1s peak is sligthly more pronounced than after exposure to air and liquid H_2O.

4.2.5. Stability studies of $Ag/Fe_3O_4(001)$ adatom array

Dosing controlled amount of H_2O

Before doing the experiments in high pressure environment and liquid water, it may be beneficial to try dosing high amount of water in a controlled way. In case that lifts the reconstruction or causes to adatoms to sinter, the dose can be lowered and the critical value can be determined. The experiments were carried out in the RT-STM chamber.

The STM images of $Ag/Fe_3O_4(001)$ adatom array after dosages of water in range of (0–10000) Langmuir are in figure 4.9. From the images it is clear, that the adatoms did not sinter, which means both the reconstruction and the adatom array survived relatively high dose of water vapour. With higher doses the tip started to interact significantly with the surface and changed a lot, which can be seen in figure 4.9 C), where the adatoms look different from the other images. In the other pictures in figure 4.9 both the surface and the adatoms look standard, the difference in their appearance is caused by the different bias voltages. In picture 4.9 D), the density of species adsorbed on adatoms increased significantly.

Exposure to air and liquid H_2O

The sample was prepared in the Omega analysis chamber, 0.3 ML of Ag adatoms were deposited. The sample was transfered to the load lock, exposed to air and a drop of liquid water was placed on top. After pumping the load lock down, the sample was transfered back and analyzed using STM (see figure 4.10). XPS and LEED were unfortunately not functional at the time this eperiment was carried out.

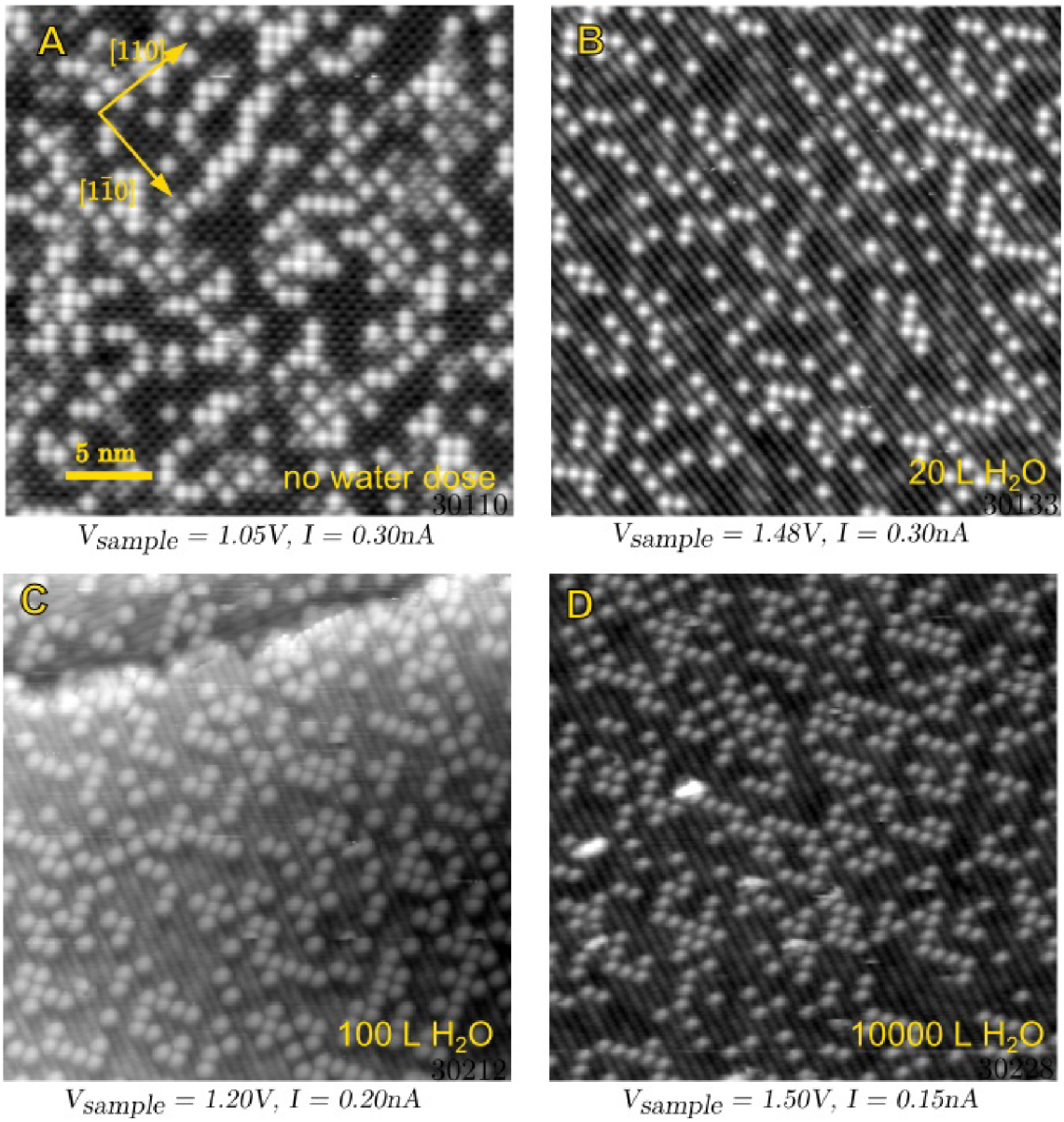

Figure 4.9: STM images of Ag adatoms (coverage 0.25 ± 0.10 ML) on $Fe_3O_4(001)$ surface after dosing H_2O. A) before dosing, B) dosed 20 L H_2O, C) dosed 100 L H_2O, D) dosed 10000 L H_2O.

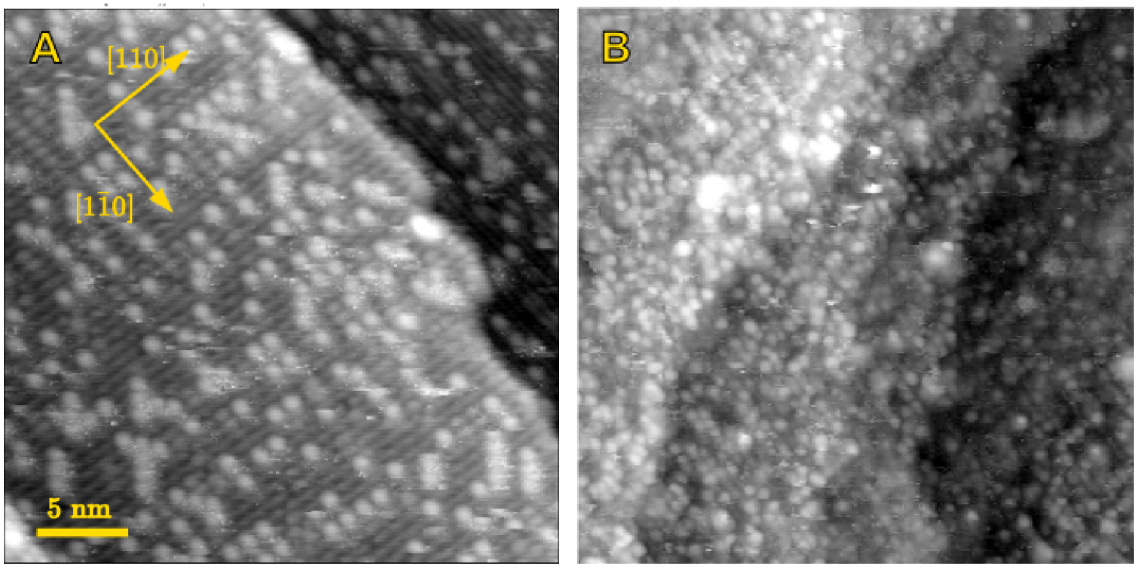

Figure 4.10: STM images of Ag adatoms (coverage 0.3 ± 0.10 ML) on $Fe_3O_4(001)$ before and after exyposure to air and liquid H_2O. A) Before exposure, B) after exposure.

4.2.6. Discussion

The high pressure exposure experiments carried out using the transfer system clearly show, that the $(\sqrt{2} \times \sqrt{2})$R45° reconstruction survives both the high pressure environment and contact with liquid water. However, what seems to have a major effect on the stability of the reconstruction is the carboneous contamination. It was observed that with increasing carbon peak detected in XPS, the intensity of the $(\sqrt{2} \times \sqrt{2})$R45° reconstruction spots detected in LEED decreases. The inconsistency in previous results can be attributed to this effect.

Experiments exposing the surface to air and to inert gas atmospere show very similar results. In both cases, the surface reconstruction survives, but traces of carbon contamination are detected. With inert gas venting, the carbon peak is slightly higher and the reconstruction spots are weaker. Hopefully, the carbon concentration in the inert gas can be minimized with installing the improved gas line with purifier and steel tubes (instead of the current plastic ones).

Dosing high amounts of H_2O vapour on the $Ag/Fe_3O_4(001)$ adatom template did not cause the adatoms to sinter. Placing a drop of liquid water on the $Ag/Fe_3O_4(001)$ adatom template seemingly didn't as well. Although the quality of the image acquired after the liquid water experiment is far from ideal, what can be said with certainty is that there are no big clusters present on the surface.

4.3. STM study of α-Fe_2O_3(012) surface

The (012) is the most stable surface of hematite. Yet, no STM study of this surface has ever been published. A brief review of the state of the art knowledge of hematite has been given in section 1.2. All the work on hematite (012) presented in this thesis has been done on the RT-STM chamber.

4.3.1. Sample preparation

The natural crystal sample was purchased from SurfaceNet. Before putting in UHV, the sample was cleaned by sonication in acetone, ethanol and Extran MA02 solution followed by sonication in ultrapure water. After the sample was insterted in the RT-STM chamber, it was immediately analyzed by XPS, indicating only contamination by carbon (that is, no sign of Al, Si, P, S, Cl, K, Ca or Ti, which were reported in previous works [33]).

Before any preparation in UHV the sample was analyzed by LEED and exhibited weak (1×1) spots (see figure 4.11 A). With a beam energy below 85 eV the sample was charging, which resulted complete distortion of the LEED pattern. The low conductivity of the sample was also detected by XPS, where the measured spectra were shifted roughly 6 eV from the expected position.

It was subsequently discovered that the mounting of the sample was not ideal, which resulted in a strong temperature gradient on the sample surface when heated to high temperatures. Different surface structures have been observed on the "hotter" and "colder" part. The temperature difference between the two is estimatedly $(100 \pm 50)\,^{\circ}$C. All the temperatures given in this section are the thermocouple readouts corresponding to the temperature of the "hotter" part.

The "hotter" part

With stepwise annealing the LEED pattern became weaker until it was almost non existent after annealing to 400 °C. The conductivity improved, the critical beam energy at which the LEED pattern got distorted went down to ≈ 60 eV. After the sample was annealed to 480 °C in O_2 ($p_{O_2} = 7 \cdot 10^{-7}$ mbar) followed by cooling in O_2 to 250 °C, the (1×1) pattern was recovered and stronger than before, and very weak (2×1) spots could be resolved as well (see figure 4.11 B). The conductivity was poor (LEED charging at $\approx$ 95 eV). As the XPS spectra indicated only slight contamination by carbon and the LEED pattern exhibited the expected symmetry, the aim of further preparation was mainly to increase conductivity needed for STM measurements by reducing the bulk.

When prolonged annealing to 480 °C both in UHV and in O_2 didn't yield any better results in terms of conductivity, sputtering (0.5 kV, 0.9 μA, 10 min) and annealing (480 °C, 10 min) cycles were utilized and the annealing temperatures were slowly raised. After roughly 10 cycles and UHV annealing to 450 °C the clear (2×1) pattern was achieved (see figure 4.11 C), LEED still exhibited charging at $\approx$ 95 eV. After roughly 20 cycles and UHV annealing to 550 °, the conductivity improved (charging at $\approx$ 60 eV), but the (2×1) LEED pattern started to exhibit additional (3×1) spots and faceting (similar to figure 4.11 D). After oxidizing the surface back to (1×1) those extra spots were gone, but the sharpness of the (1×1) was never fully reclaimed. The shift of XPS spectra was significantly lower ($\approx$ 1 eV).

After roughly 40 more sputtering and annealing cycles with higher ion energy (1 kV, 1.8 μA) and temperatures up to 630 °C, the LEED charging energy went down to $\approx$ 30 eV.

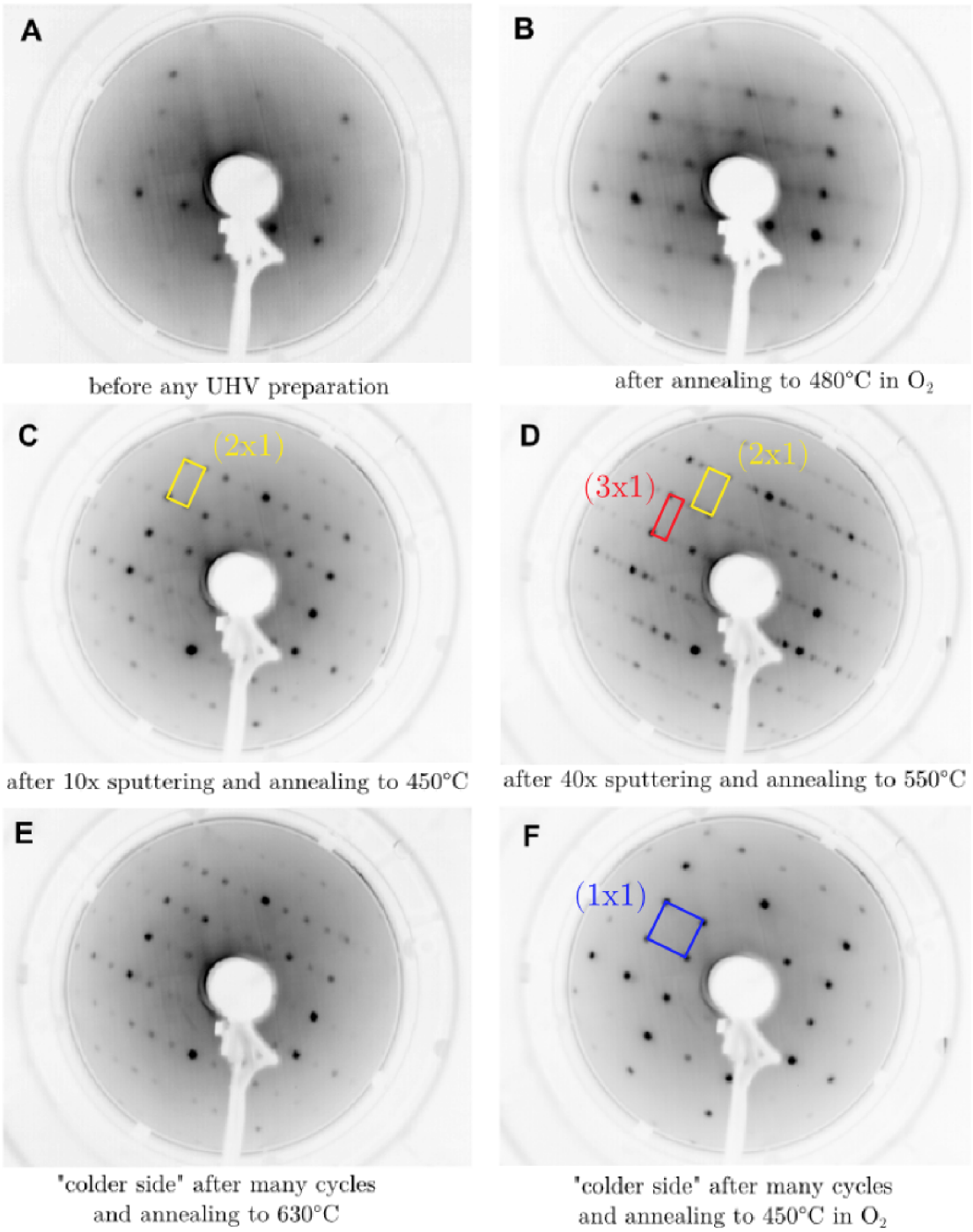

Figure 4.11: LEED patterns (150 eV) acquired during initial preparation of the hematite (012) surface. A) Following the wet chemical preparation, a weak (1×1) pattern was visible. B) After annealing to 450 °C in O_2 the pattern got stronger. C) Clear (2×1) pattern was observed after 10 sputtering/annealing cycles. D) After more cycles with annealing temperatures up to 630 °C, the new (3×1) spots appeared. The quality of the surface deteriorated irreversibly - higher background, lower sharpness of the spots. E), F) Both the (1×1) and (2×1) patterns are still reproducibly achievable at the "colder" side of the crystal. The temperatures on this side are estimated (100–150) °C lower than the thermocouple reading.

On the reduced surface, the (3×1) and (2×1) pattern was always present, on the oxidized one some weak residual (3×1) spots remained.

The "colder" part

After the preparation described above, the temperature gradient on the sample was discovered and the "colder" part was analyzed. On the "colder" part, there were no (3×1) spots and both the (2×1) and (1×1) could be easily achieved by annealing to 630 °C in UHV or to 450 °C in O_2 (see figure 4.11 E,F).

When the critical charging energy in LEED was (20–40) eV and XPS shift <0.5 eV, an STM approach was attempted. XPS spectrum of the sample after the described cleaning procedures is shown in figure 4.12.

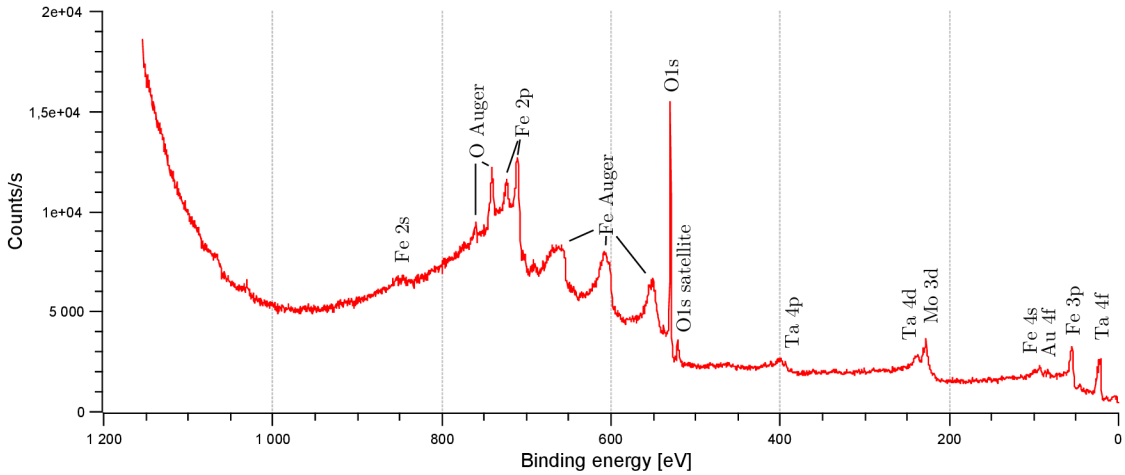

Figure 4.12: XPS spectrum of the hematite (012) sample after the cleaning procedures. Apart from Fe and O, there are peaks from Ta, Mo and Au. Tantalum comes from the clips used for mounting the sample to the molybdenum sample plate. Between the sample and the sample plate there is a gold foil to enhance the thermal contact. These peaks weren't shifted when the sample was not conductive, therefore we are confident those elements are not present on the sample surface.

4.3.2. The (1×1) reconstruction

The oxidized (1×1) reconstructed surface can be imaged by STM with sample biases as low as ± 1 V. The surface exhibits large terraces, >100 nm width is not uncommon. Images acquired on the same spot with positive, and negative sample bias are shown in figure 4.13. In both the empty and filled states images an easily distinctive zig zag line pattern is present. On the surface there are many white and black clusters. The single step edges are quite common feature of the surface, measured step height is roughly (350 ± 20) pm.

Discussion

The dimensions of the zig-zag lines observed in STM are consistent with the bulk terminated model (see figure 4.14). The measured unit cell dimensions are approximately 5.4×6.1 Å^2 which corresponds to dimensions of the bulk terminated unit cell 5.0×5.4 Å^2.

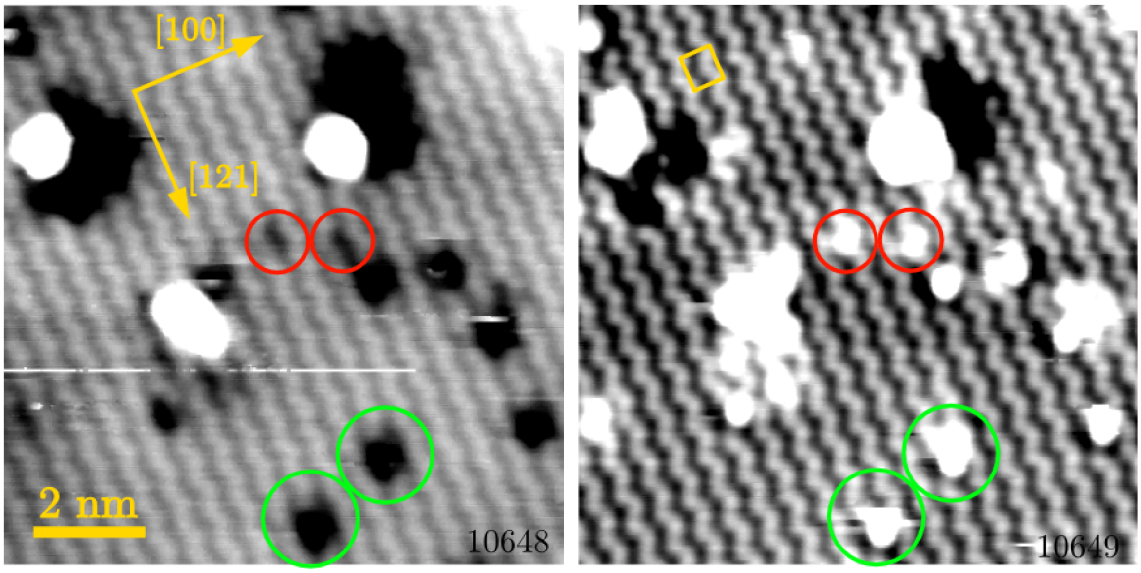

Figure 4.13: Filled states (left) and empty states (right) STM images of the hematite (012) (1×1) reconstructed surface acquired on the same spot. Both the filled and empty stated images feature dictinctive zig zagging lines. The (1×1) unit cell is highlighted by the yellow square. Position of the defects hints, that the lines are out of phase - the species highlighted by red circle sit on the dark row in the filled states image and on the bright row in the empty states image. The species highlighted by green circle occupy a space between two dark rows on the filled states image and and a space between two bright rows in the empty states image.

The difference can be attributed to the non ideal calibration of the STM, the important fact is that the ratio of the dimensions is similar. From the position of the defects (such as the ones highlighted in figure 4.13) it can be concluded that the lines are out of phase. That can be reconciled with of the bulk terminated model, as both the Fe and O atoms can be seen as zig-zag lines from the top view. It also corresponds to the bulk density of states calculations, which show higher DOS of O in filled states and higher DOS of Fe in empty states [60]. The DOS above the surface imaged by STM might however be different, so this hypothesis must be first confirmed by STM simulations in order to be accepted. The step height of (350 ± 20) pm agrees with the bulk terminated step height of 370 pm.

From the side view image of the bulk terminated surface (see figure 4.14 C) it is clear that the model surface has no dipole moment perpendicular to the surface and thus can be classified as Tasker type 2 non-polar surface [61] and be considered stable. The acquired STM images agree very well with the bulk termination model and at the moment there is no reason to believe that there would be any other surface termination on the (1×1) surface.

Since it has been previously reported, that dissociated water binds strongly to the (1×1) surface [33], it seems probable, that some of the defects present in the STM images are surface or terminal hydroxyls. This hypothesis will be checked by further STM adsorption studies on this surface.

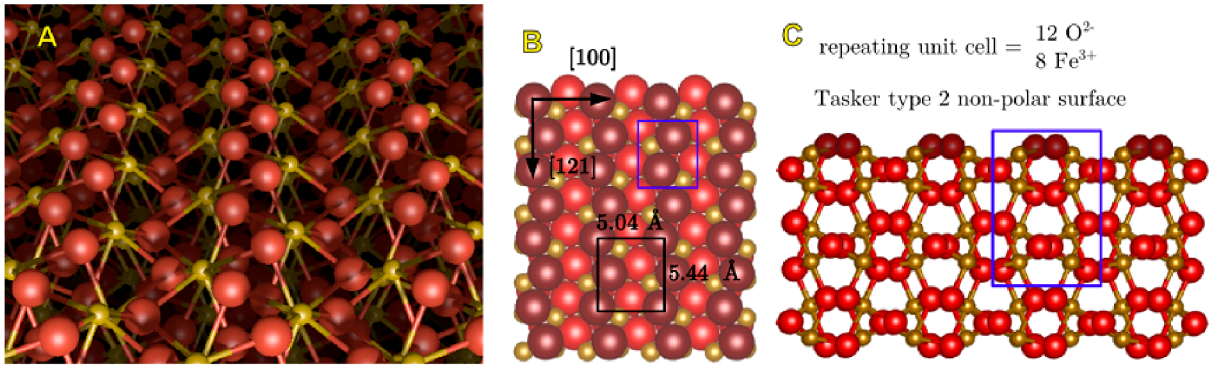

Figure 4.14: Bulk terminated hematite (012) surface. A) Perspective view on the bulk terminated hematite (012) (1 × 1) reconstructed surface. Oxygen atoms are red, iron atoms are yellow. B) Space-filing top view on the bulk terminated (1 × 1) surface. The surface oxygens are highlighted by dark red colour. C) Ball-and-stick side view on the bulk terminated (1 × 1) surface. The surface oxygens are highlighted by dark red colour. The repeating unit cell is highlighted by blue rectangle in pictures B and C. The cell has zero dipole moment, therefore the surface is classified as Tasker type 2 non polar.

4.3.3. The (2 × 1) reconstruction

The reduced (2 × 1) reconstructed surface can be imaged by STM with sample biases as low as ±1 V, although imaging in empty states is generally less stable. Images acquired following preparation by UHV annealing are shown in figure 4.15. On both the empty and filled states images there are lines in the same direction as on the (1 × 1) surface (the sample orientation is the same on all the STM images in this chapter).

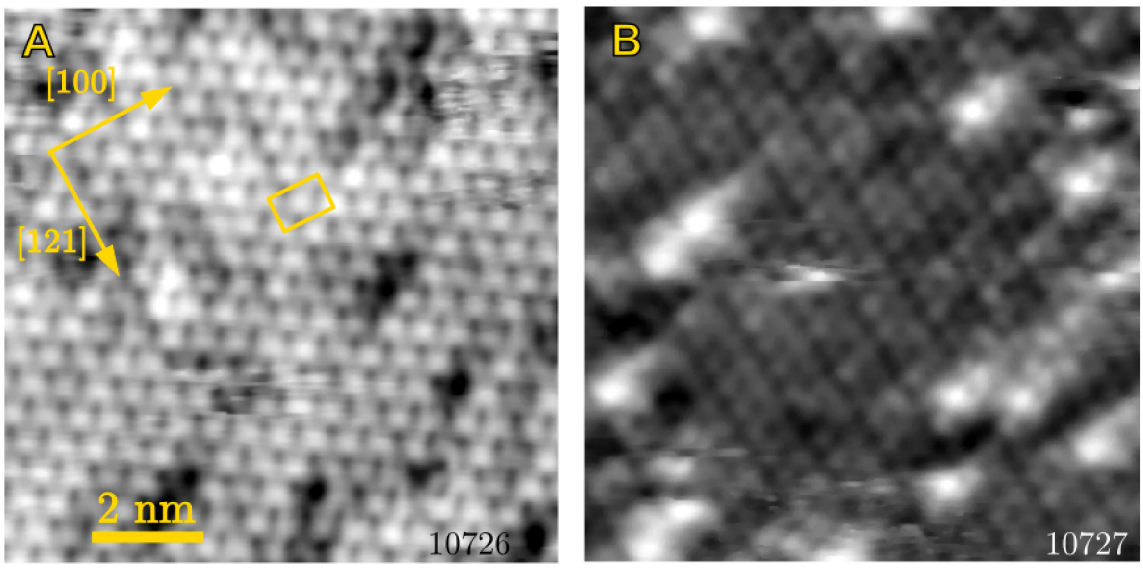

Figure 4.15: Filled states (left) and empty states (right) STM images of the (2 × 1) reconstructed surface of hematite (012). The (2 × 1) unit cell is highlighted by the yellow rectangle.

In the empty states images, there are always two lines close together followed by a wider gap. The same can be seen on the filled states images, but the appearance is strongly

dependent on the tip (it is not very clear in fig 4.15 A, but can be resolved quite well in figure 4.17 A). The (2×1) structure strongly resembles hexagonal pattern on some images (see figure 4.15 A).

The width of the terraces is similar as on the (1×1), but contrary to the behaviour observed on the (1×1), the single step edges on the (2×1) surface are very rare. Usually the terraces are bordered by a set of several closely neighboring step edges (see fig. 4.16 A). The single step height seems to be similar to the step height on the (1×1), based on measurement in one image shown in figure 4.16 B.

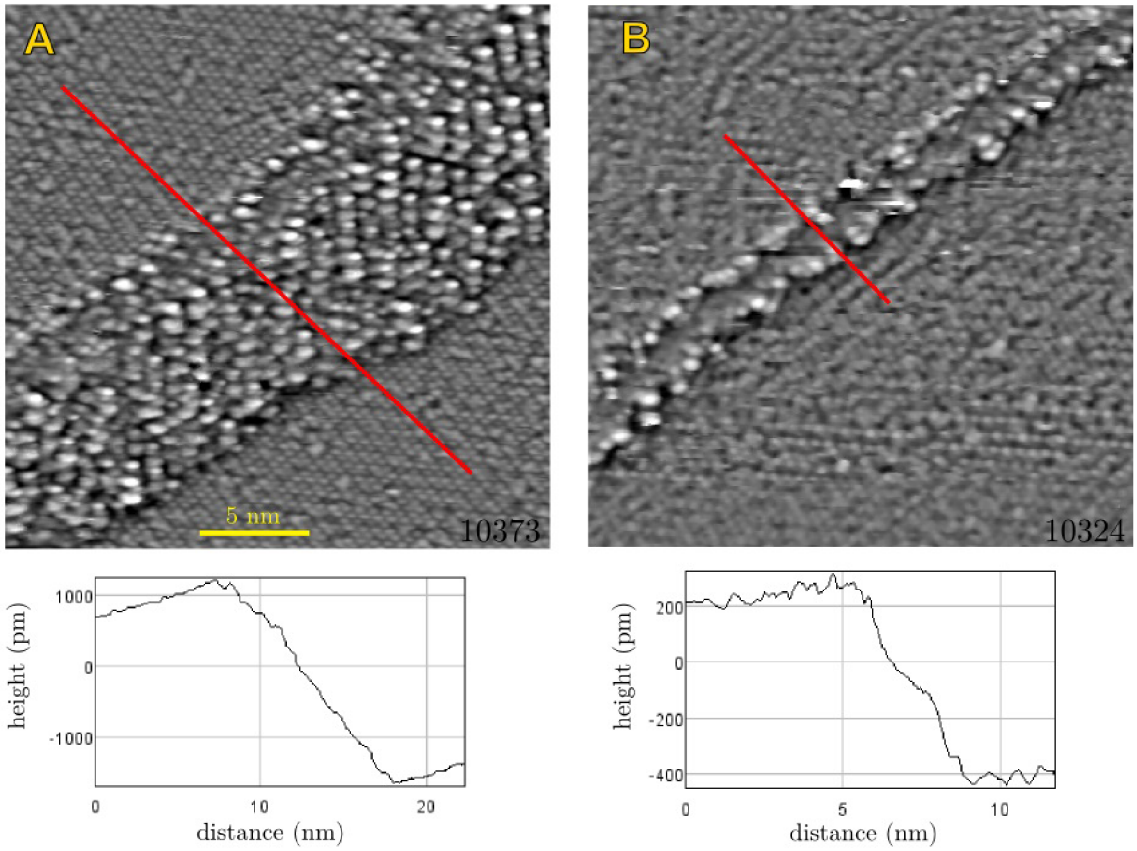

Figure 4.16: Differentiated high-pass filtered filled states STM images of the step edges on the hemqtite (012) (2×1) reconstructed surface, probably acquired with a multiple tip. The terraces are usually enclosed by a set of step edges similar to the one shown in image (A). The height of the usual set is in the range of $(10^2$–$10^4)$ pm, which would correspond to units to tens of steps of height 350 pm. Single step edges are difficult to find. Image B) shows height measurement on two single step edges. Although it cannot be said for sure if the image shows two step edges or one step edge imaged with a double tip, the height of ≈ 700 pm corresponds to two steps of height 350 pm, which were observed on the (1×1) surface.

When kept in UHV, the surface rather quickly develops into a different structure. Even though the pressure in the chamber is 7×10^{-11} mbar, some species adsorb on the surface. The images in figure 4.17 show the progression of the system in time. The adsorption of these species (as will be shown in the next section, it is most likely H_2O) changes the surface symmetry and within tens of minutes creates patches filled with 1D chains under the angle of $\pm 60°$ from the original line direction present on the fresh (2×1) surface (see fig. 4.17 B,C). After several hours, bright zig-zag lines with (2×1) start to form on the borders of the patches (fig. 4.17 C). After two days these bright zig-zag lines already occupy significant area of the surface (fig. 4.17 D). The 1D chain patched adsorbant overlayer is very mobile and rearranges itself constantly while forming, as measured by timelapse STM. The bright zig zag lines do not move with time, the mobility is only observed at the very ends of the lines. The 1D patched surface can be detected by LEED pattern as it creates $c(2 \times 1)$ spots (see figure 4.18 C). With exposure to electron beam of LEED, this adsorbant overlayer rearranges to (2×1) creating bright zig-zag lines, similar to the ones forming with time, but less ordered (see figure 4.18 B).

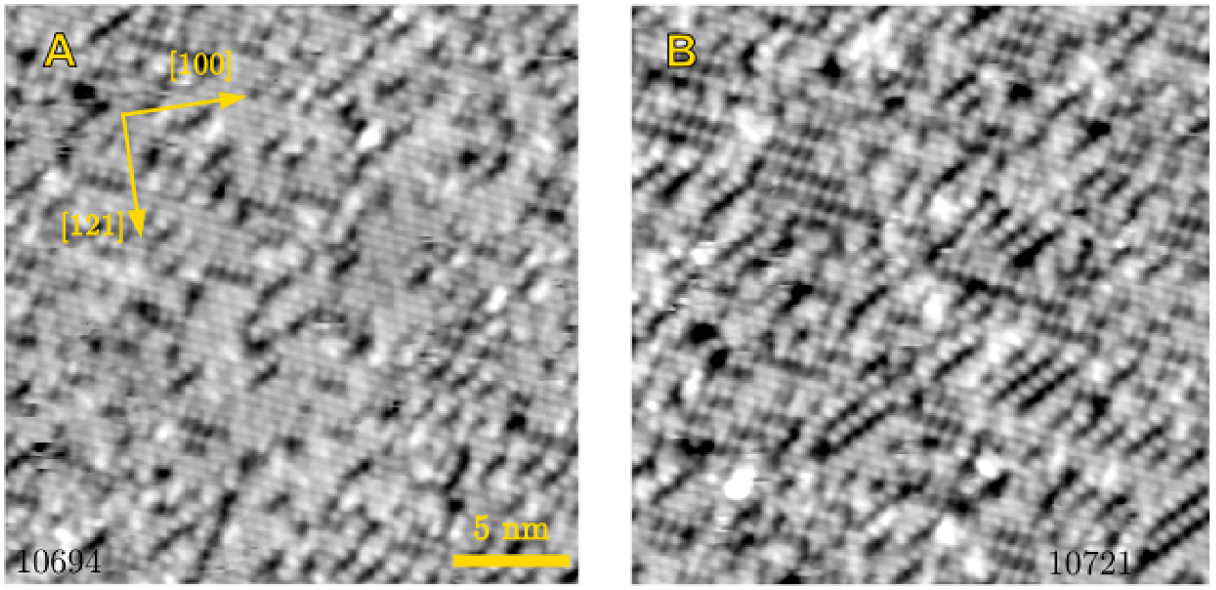

freshly prepared surface

after 80 minutes

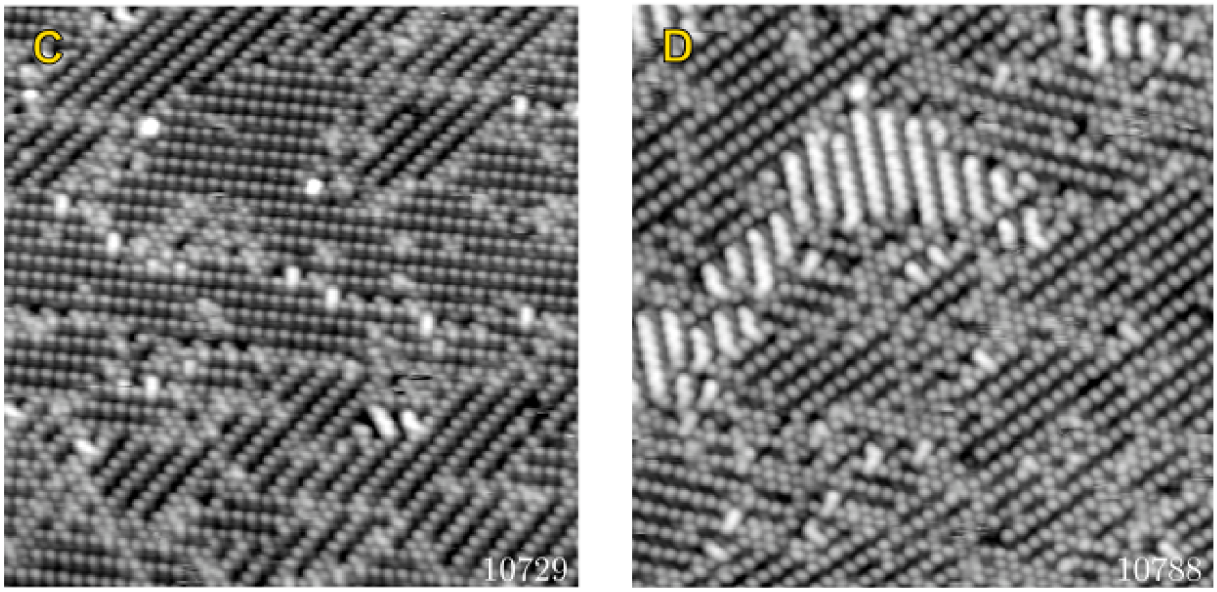

after cca 16 hours

after cca 60 hours

Figure 4.17: Development of the hematite (012) (2×1) reconstructed surface kept in UHV with time. The chamber pressure is 7×10^{-11} mbar. STM images are taken with $V_{sample} = = -2\,\mathrm{V}$, $I = 0.10\,\mathrm{nA}$. Adsorbants change the surface symmetry by creating patches of 1D chains. With time, bright zig-zag lines start to form. Images A and B are taken at the same spot, C and D are not.

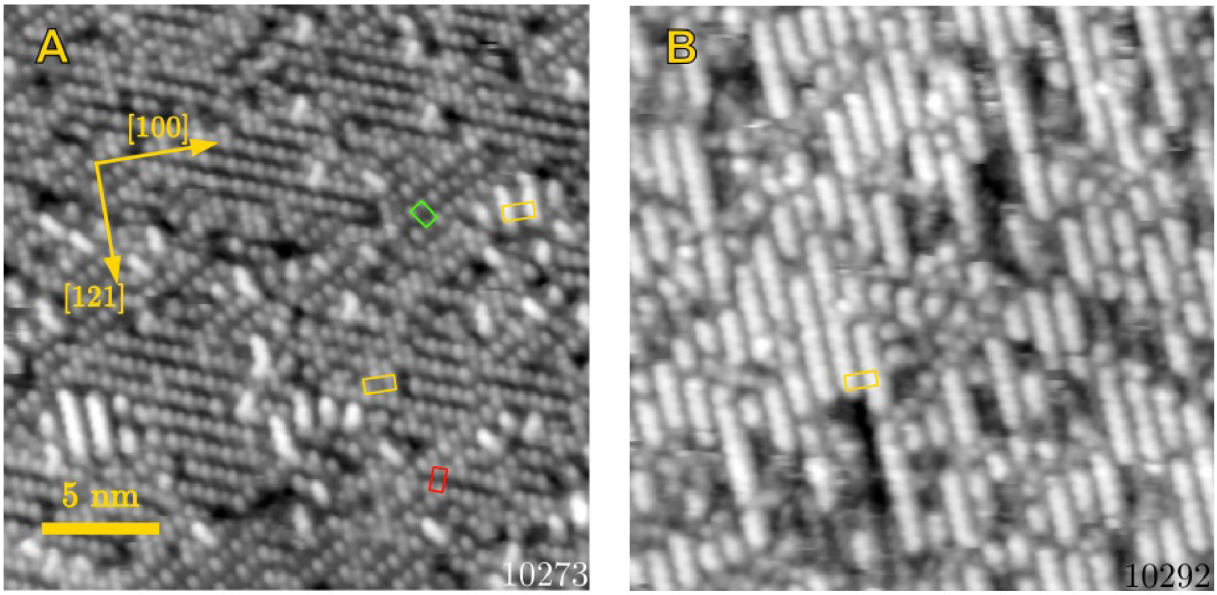

(2 x 1) surface after
cca 24 hours in UHV

the same surface after
cca 3 min exposure to e-beam

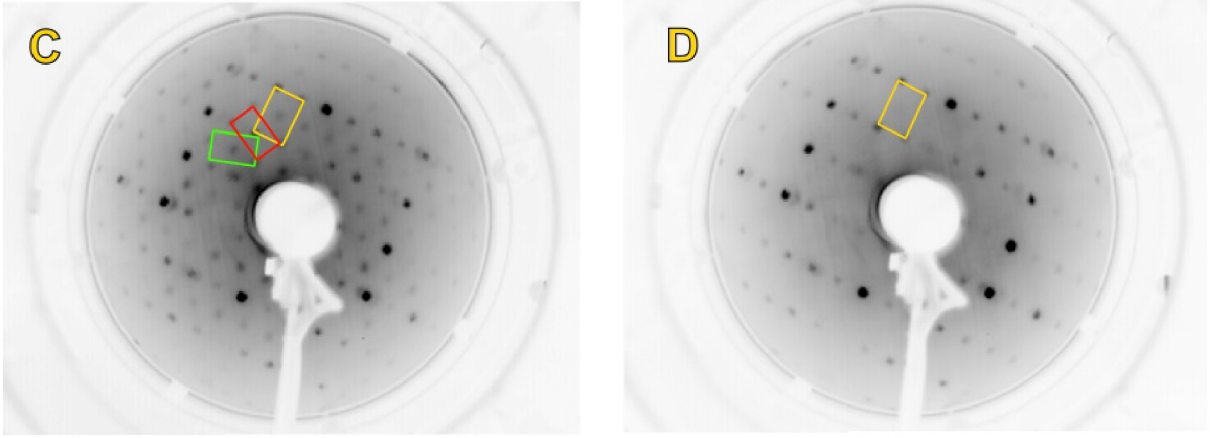

LEED pattern of the surface
featuring patched with 1D chains

LEED pattern after cca 3 min
of exposure to e-beam

Figure 4.18: STM and LEED results acquired on the hematite (012) (2×1) reconstructed surface left in UHV for several hours. The 1D chains create a c(2×1) spot in LEED as a superposition of the LEED pattern of three different domains. The unit cells are highlighted both in the STM images and in the LEED patterns (A,C). After several minutes eposure to the LEED e-beam the surface structure changes to (2×1) again (D). The surface is filled with bright zig zag lines (C). The STM images are taken at different spots.

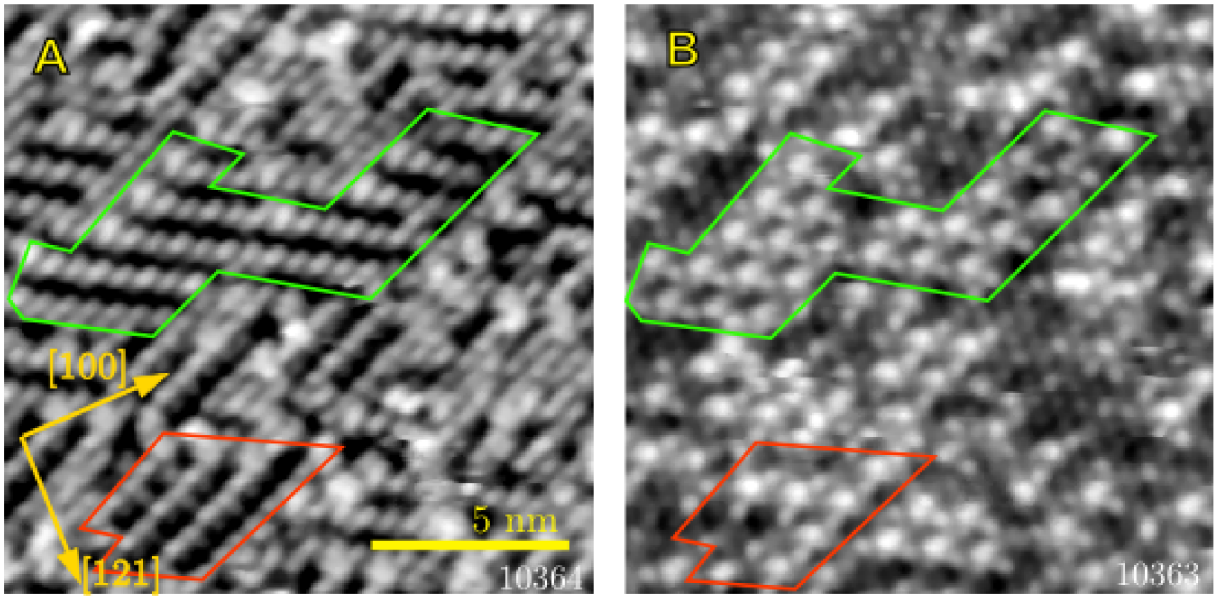

Figure 4.19: Filled (A) and empty (B) states image of the same spot on the patched reconstruction of the hematite (012) (2×1) reconstructed surface. The 1D chains can be seen in both images (as highlighted by the red and green lines), although in filled states they are much clearer. In empty states the repeating unit of the chain consits of two different species with one of them much more pronounced. In filled states, the chains look homogeneous.

The surface patched with 1D chains can be imaged both in filled and empty states. In both images, the chains look bright. While in filled states the chains look completely homogeneous, in empty states the repeating unit of the chain consits of two different species with one of them much more pronounced (see figure 4.19).

Dosing O_2

As the similar c(2 × 2) symmetry has been reported to form with dosing oxygen at room temperature [43], O_2 was the first candidate for the induced overlayer formation documented by STM. With O_2 exposure the 1D chain patches forming process is accelerated, but it never reaches the point where the whole surface would be covered by the patches of differently oriented 1D chains (see figure 4.20). Instead, islands of weakly bound oxygen and zig-zagging lines in the original direction start to form (see figure 4.20 D).

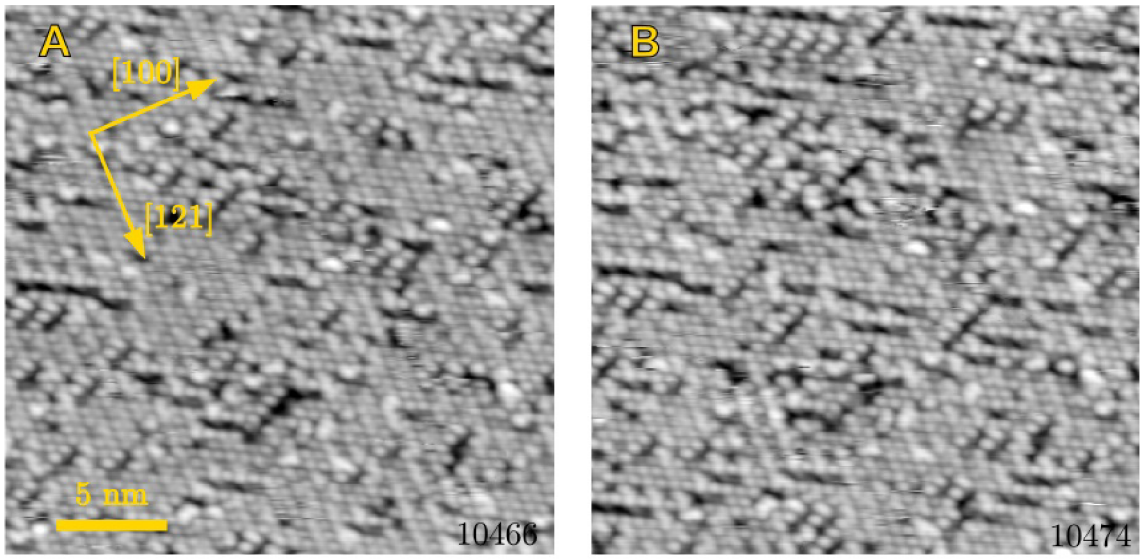

freshly prepared surface

after 25 min of dosing O_2
$p_{O_2} = 5{\cdot}10^{-9}$ mbar

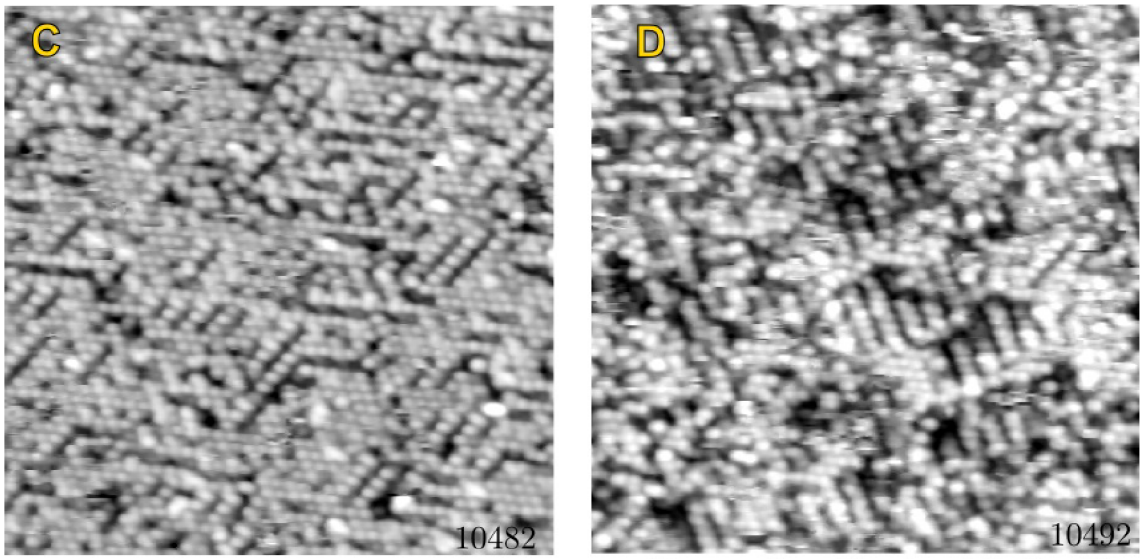

after another 25 min of dosing O_2
$p_{O2} = 5{\cdot}10^{-8}$ mbar

after another 25 min of dosing O_2
$p_{O2} = 2{\cdot}10^{-7}$ mbar

Figure 4.20: Dosing of O_2 on the (2 × 1) reconstructed (012) surface of hematite documented by STM. Filled states timelapse STM images on the same spot while dosing O_2. Oxygen accelerates the patches forming process in the beginning, but does not cause the same effect as just leaving the sample in UHV for several hours.

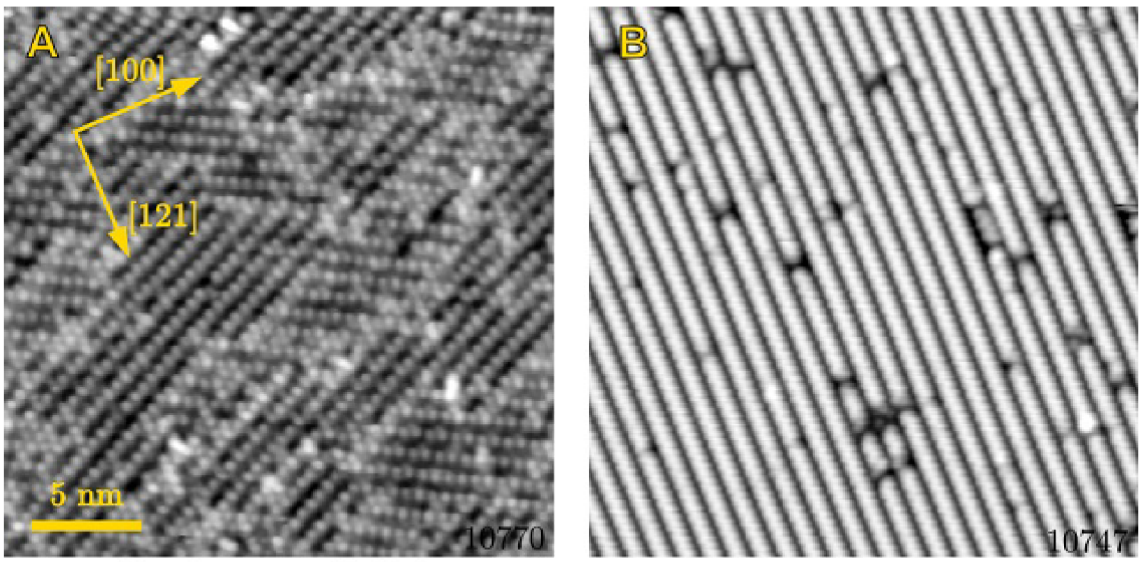

Figure 4.21: Dosing of water on the (2×1) reconstructed (012) surface of hematite documented by STM. A) Dosing small amount of H_2O on the freshly prepared (2×1) surface creates the same structure as keeping the freshly prepared surface in UHV for several hours. B) Dosing 1 L of H_2O fills the surface with bright zig-zag lines of the same kind as the ones that start to form on the patched surface after several hours in UHV.

Dosing H_2O

The second candidate adsorbant is H_2O. Water is common in residual gas and it is already known that the (012) surface dissociates water and adsorbs it at room temperature [33]. After dosing small amount of water (0.1 L, $1\,\mathrm{L} = 1.33\,\mathrm{s} \cdot 1 \cdot 10^{-6}$ mbar, pressure measured by cold cathode gauge), the surface is fully covered with the same 1D chain patches as after several hours in UHV (see figure 4.21 A). When the dose is increased (1 L), the surface is fully covered with bright zig-zag lines of the same type as the ones that form on the patched surface after several days in UHV (see figure 4.21 B).

With exposure to the e-beam of LEED, the observed (2×1) pattern changes to (1×1) within a few minutes. The STM images of the surface after exposure to LEED show disordered zig zag lines (see fig 4.22) , the (1×1) symmetry is not visible in STM nor in FFT of the STM images.

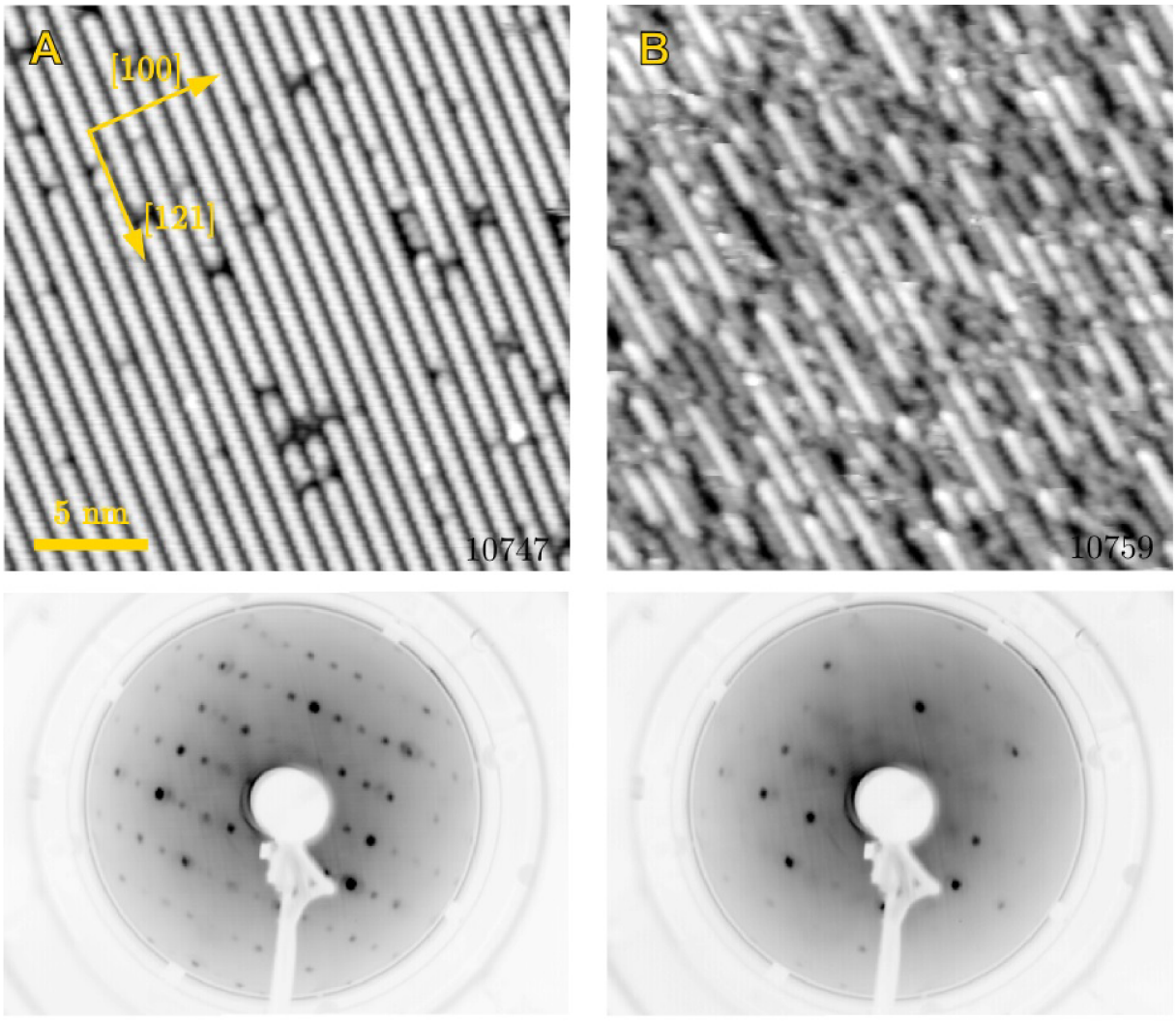

Figure 4.22: Effect of the LEED e-gun on the (2×1) reconstructed (012) surface of hematite. The clear (2×1) pattern of the adsorbed water (A) is transformed to (1×1) with prolonged exposure to LEED (B). In the STM image the (1×1) structure is not visible, the surface looks like disordered (2×1).

Discussion

Both the filled and empty states STM images of the (2×1) reconstructed surface feature distinctive (2×1) pattern. There are always two rows in the [121] direction, that are closely packed together and divided from the other rows by a slightly wider gap. The (2×1) pattern however looks different in empty and filled states images. In the filled states images, the two rows close together are "out of phase", meaning the atoms in the neighboring lines are not stacked in the [100] direction, but in line deflected roughly 30° from it. As a consequence, the (2×1) structure in the filled states resemble a hexagonal pattern (see figure 4.15 A). In the empty states however, the atoms in the neighboring rows are in the same line along the [100] direction and the surface looks rectangular. This would agree with the conclusion drawn from the STM images acquired on the (1×1) surface, which says that with different bias polarity different atoms are detected.

Based on the STM study of the (2×1) surface, the missing row termination model mentioned in [43] does not seem plausible as no missing row is observed. A possible surface termination model that would qualitatively explain the observed behaviour is shown in figure 4.23. The surface is created from the (1×1) by removing every other oxygen from every row (see fig 4.23 B). That way the (2×1) symmetry is created. The unit cell dimensions fit to the dimensions measured by STM, the structure of oxygen atoms corresponds to the pattern visible in the filled states STM images. The model also features "wider" and "narrower" gaps between the oxygen lines. All the surface Fe atoms are four coordinated, as can be seen in figure 4.23 A. Based on previous studies by Henderson [44], the surface Fe are in 2+ oxidation state. That is in agreement with the proposed model, as the surface unit cell has zero charge when the surface Fe is reduced (fig 4.23 C). There is a reason to believe the surface may undergo some relaxation, possibly resulting in the Fe atoms in the "narrower" or "wider" gap moving to a tetrahedral site between the remaining O atoms, effectively deactivating the "narrower" or "wider" cation site for adsorption. The stability of the proposed surface will be simulated by DFT studies in the near future.

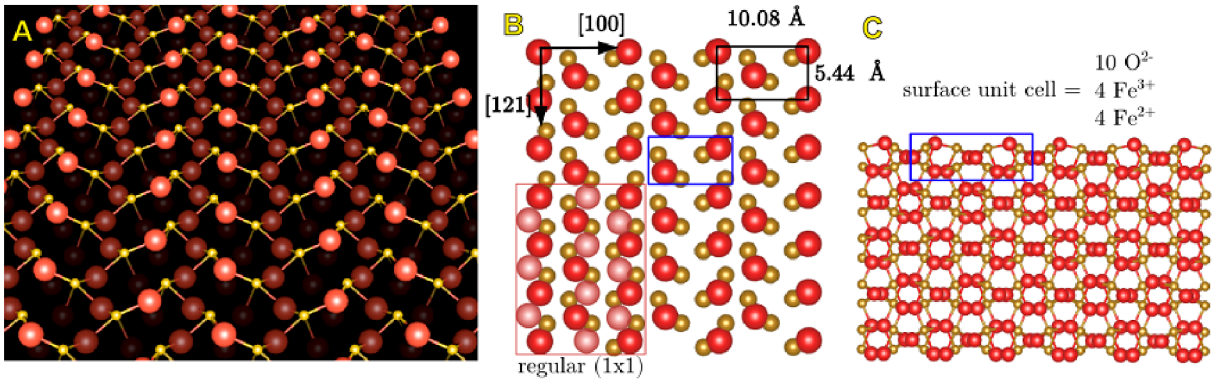

Figure 4.23: A) Perspective view on the proposed model of the hematite (012) (2×1) reconstructed surface. Oxygen atoms are red, iron atoms are yellow. All the surface Fe atoms are four coordinated. B) Space-filing top view on the top layer of the proposed (2×1) surface. Atoms removed from the (1×1) surface are shown in the red rectangle. C) Ball-and-stick side view on the proposed (2×1) surface.

Adsorption studies of O_2 and H_2O are in qualitative agreement with previous work on this surface [33], [44], [43], although there are many open questions left.

Adsorption of O_2 on the (2×1) surface affects the adsorption of H_2O, which corresponds to the results published in [43]. Henderson claims that O_2 coverages lower than $5.4 \cdot 10^{14}\,\mathrm{cm}^{-2}$ create $c(2\times2)$ symmetry in LEED, in higher coverages the (2×1) symmetry is recovered. The conclusion from TPD measurements is that O_2 adsorption stabilizes some OH groups on the surface. In our experience, O_2 accelerates the process of H_2O adsorption when the coverage is low. Then however, the overlayer never reaches the point, where it would exhibit strong symmetry resulting in intensive $c(2 \times 1)$ spots in FFT. Instead, zig-zag lines with (2×1) symmetry in the original direction and islands of weakly adsorbed species form on the surface. It remains unclear, why the surface would exhibit $c(2\times2)$ with low O_2 doses as observed by Henderson. In our work, we only observed very weak $c(2 \times 1)$ in the FFT of STM images taken after exposing the surface to low dose of O_2. A possible explanation might be that in the previous work the H_2O vapour pressure in the chamber was different and that water is the specie responsible for the differing

results. The subject of oxygen adsorption on the (2×1) reconstructed hematite (012) surface must be investigated further to clarify the slightly differing results and unify the conclusions.

According to [33], water adsorbs dissociatively on the (2×1) reconstructed surface and desorbs at 400 K. Contrary to usual behaviour on metal oxides, the water desorption peak has pseudo-zeroth order, which suggests the hydroxyls are bound in one-dimensional arrays with desorption ocuring preferentially at the ends of each array. That is in agreement with our work, where adsorbed H_2O creates bright zig zag lines with (2×1) symmetry with the ends of these lines being mobile. What is not entirely clear is how the 1D chains patched reconstruction fits into the TPD spectra published by Henderson. The troubling thing is that there is only one desorption peak above room temperature (which can be safely attributed to the zig-zag lines) for two different surface structures formed by dissociated H_2O. A possible explanation is that the zig zag lines are thermodynamically more stable than the patches, but their formation is kinetically hindered. The sites occupied in the patched reconstruction might be preferred as adsorption sites, but with more energy provided either by the presence of more adsorbants or by heating, it may rearrange to the thermodynamically more favourable zig-zag line configuration. As the temperature rises while measuring TPD, the 1D chains first rearrange to zig zag lines and only then desorb. Apart from reconciling the STM images with the TPD results, this theory would also explain why the 1D patched surface forms zig zag lines after exposure to the LEED electron gun. The (2×1)-to-(1×1) transition of the H_2O saturated surface exposed to LEED e-beam however remains puzzling. Further STM and TPD studies must be carried out in order to validate the presented hypotheses.

4.3.4. The (3×1) reconstruction

The (3×1) reconstruction, mixed with (2×1), was observed in the LEED patterns of the part of the sample, that was annealed to higher temperatures. Even after oxidation, the (3×1) spots never really disappeared. With lower LEED energies, faceting was clearly distinguishable see figure 4.25.

STM imaging on this part of the crystal was difficult, as the surface was very rough and steppy. STM images of characteristic features of this surface are shown in figure 4.24. As the surface is most probably hematite partially transformed to magnetite (will be discussed in the next section), this part of the crystal was not further investigated.

Discussion

The STM images of this surface strongly resemble the Fe_3O_4(110) as it features 1D array of bright lines with commensurate dimensions - the line separation on image 4.24 B is ≈ 2.6 nm, on magnetite (110) it is 2.52 nm [28]. The LEED results support this impression as the Fe_3O_4(110) surface is formed by nanofacets with (3×1) symmetry. From the calculated phase diagram of ixon oxides [62] it is clear, that the methods of preparation (annealing in UHV to 630 °C) are at the borderline between Fe_2O_3 and Fe_3O_4. All that put together, it seems reasonable to assume that this surface is partially transformed to Fe_3O_4.

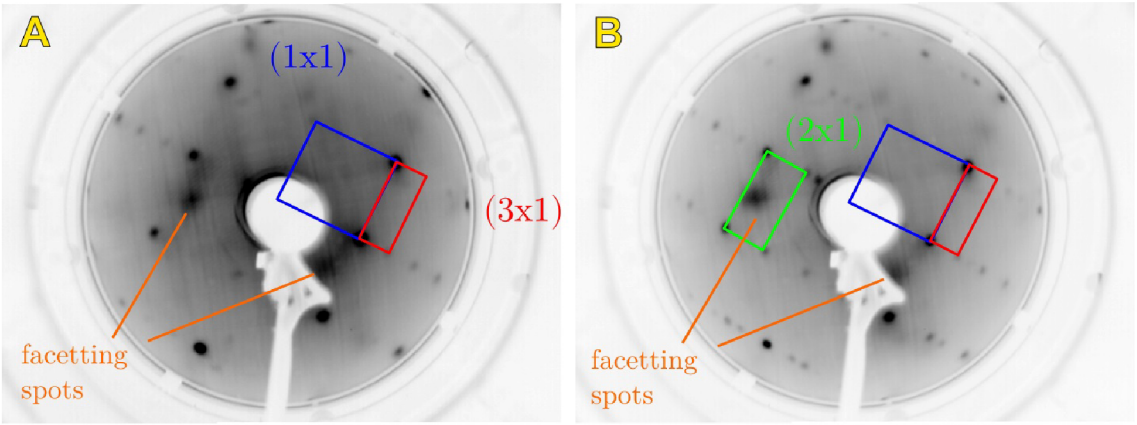

after annealing in O_2 | after annealing in UHV

Figure 4.24: LEED patterns (beam energy 50 eV) acquired on the "hotter" part of the hematite (012) surface. The (3×1) spots and facetting are distinguishable both after annealing in O_2 (A) and after annealing in UHV (B).

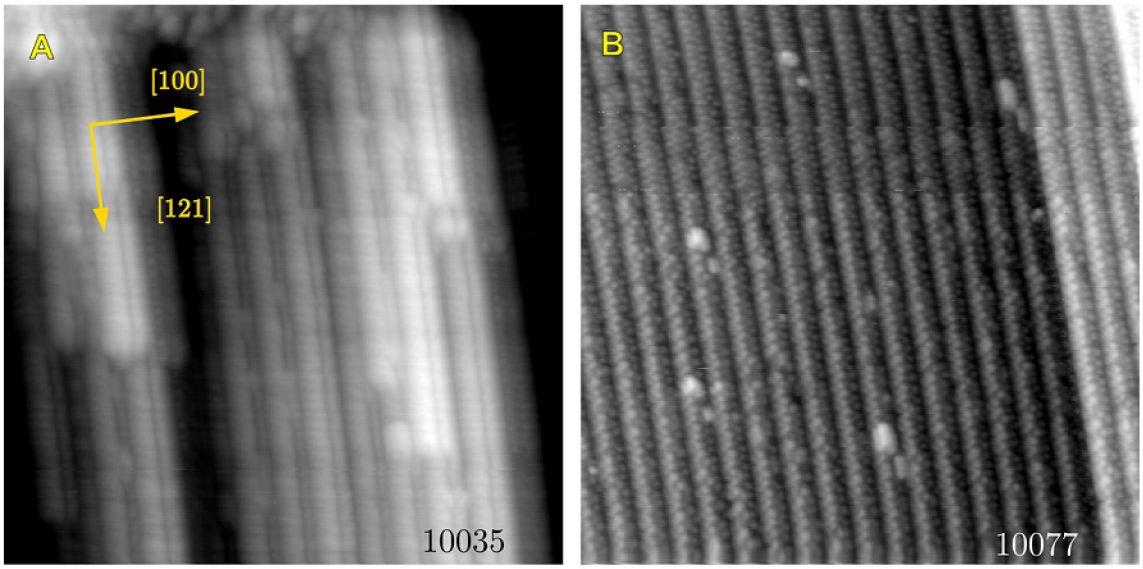

$V_{sample} = +2$ V, $I = 0.10$ nA | $V_{sample} = +1.5$ V, $I = 0.10$ nA

Figure 4.25: STM images on the "hotter" part of the hematite (012) crystal after annealing in UHV. The surface is filled with 1D steps and facets, strongly resembling the $Fe_3O_4(110)$ surface.

Conclusion

This thesis focuses on connecting the ultra-high vacuum surface science with electrochemical approach towards development of novel catalysts. A crucial part of this thesis is the design of the UHV-EC transfer sytem, which enables doing combined experiments, making use of the expertise from both fields.

The first two chapters give a brief introduction to the studied samples and techniques used for their surface characterization. To the UHV-EC transfer system, the third chapter is dedicated. Possible designs of the transfer system applicable to a specific UHV chamber are reviewed, three different configurations are discussed - a concept with vertical transfer in the load-lock chamber directly above the electrochemical cell, a configuration with a separate glass compartment and glass vertical transfer and a miniature flow cell. Eventually the concept with separate glass compartment with vertical transfer was chosen, the most notable advantages being preventing metal microparticles from falling to the electrochemical cell and ease of operation.

The concept was further developed and a fully functional UHV-EC transfer system was designed, assembled and brought into operation. The design features are discussed in depth in the third chapter. Aside from the parts designed specifically for the transfer system, a special holder with magnetic locking mechanism was designed, which is rather versatile and has already found its place in other UHV chambers at the institute as well.

The system was used for the stability studies of the $Fe_3O_4(001)$ surface reconstruction, that are described in the fourth chapter. It was shown that the $(\sqrt{2} \times \sqrt{2})R45°$ reconstruction survives in ambient conditions, exposed to both air and liquid water. However, what lifts the reconstruction are the oil traces coming from the roughing pump. The previous inconsistency in the water dosing experiments can be attributed to the carboneous contamination of the chamber.

The $Ag/Fe_3O_4(001)$ adatom array survives high doses of water (up to 10000 L) without any significant alteration of the structure visible in the STM images. After exposing the adatom array to air and liquid water, the surface became very difficult to scan, so the individual adatoms are not that well recognized. What can be said with certainty is that the adatom array did not sinter significantly.

The second experimental project described in this thesis is the first-ever published atomic scale study of the hematite (012) surface. Both the previously reported surface reconstruction of the hematite (012) surface were imaged with scanning tunneling microscope. Consistent with previous studies using different techniques, the oxidized (1×1) surface reconstruction corresponds to the bulk termination model. The reduced (2×1) surface was studied as well, the STM images however do not seem to correspond to any of the so far proposed surface termination models. Reactivity of the surface with H_2O and O_2 was studied using timelapse STM. Based on the STM study presented in this thesis, a surface structure model was proposed, its validity will be soon checked by DFT simulations.

The experimental results presented in this thesis are very encouraging. Although there was a glimpse of hope that the $Fe_3O_4(001)$ based adatom array might not be destroyed with water, the general consesus based on previous results was that it most probably would. Work presented in this thesis proves that the adatom array used for single atom catalysis in UHV environment survives in ambient conditions. Up to a few months ago, this claim would be nothing more than a wishful thinking. The subject will be further studied and the promising concepts developed in UHV will be tested in realistic conditions.

The hematite (012) project is still in a very early stage, but the so far acquired results surpassed even the most optimistic predictions. With the well known and troublesome nature of the hematite (001) surface, which makes it very difficult to work with in UHV environment, nobody tried STM imaging of the (012) surface before. We did now and we show, that not only the surface can be scanned without any difficulties, but many of the interesting properties, such as water dissociation, can be followed on an atomic scale. As promising as the hematite is for wide range of applications, understanding its surface structure may turn out to be a major development in the field.

References

[1] WILTSCHKO, R. and W. WILTSCHKO. The magnetite-based receptors in the beak of birds and their role in avian navigation. *Journal of Comparative Physiology A*. 2012, vol. 199, no. 2, pp. 89–98. ISSN 1432-1351.

[2] ZENG, T., W.-W. CHEN, C. M. CIRTIU, A. MOORES, G. SONG and C.-J. LI. Fe3O4 nanoparticles: a robust and magnetically recoverable catalyst for three-component coupling of aldehyde, alkyne and amine. *Green Chem.* 2010, vol. 12, no. 4, pp. 570. ISSN 1463-9270.

[3] DILNAWAZ, F., A. SINGH, C. MOHANTY and S. K. SAHOO. Dual drug loaded superparamagnetic iron oxide nanoparticles for targeted cancer therapy. *Biomaterials*. 2010, vol. 31, no. 13, pp. 3694–3706. ISSN 0142-9612.

[4] TARTAJ, P., M. P. MORALES, T. GONZALEZ-CARRENO, S. VEINTEMILLAS-VERDAGUER and C. J. SERNA. The Iron Oxides Strike Back: From Biomedical Applications to Energy Storage Devices and Photoelectrochemical Water Splitting. *Advanced Materials*. 2011, vol. 23, no. 44, pp. 5243–5249. ISSN 0935-9648.

[5] NOVOTNY, Z., G. ARGENTERO, Z. WANG, M. SCHMID, U. DIEBOLD and G. S. PARKINSON. Ordered Array of Single Adatoms with Remarkable Thermal Stability: Au/Fe3O4 (001). *Physical Review Letters*. 2012, vol. 108, no. 21. ISSN 1079-7114.

[6] BLIEM, R., E. MCDERMOTT, P. FERSTL, M. SETVIN, O. GAMBA, J. PAVELEC, M. A. SCHNEIDER, M. SCHMID, U. DIEBOLD and P BLAHA. Subsurface cation vacancy stabilization of the magnetite (001) surface. *Science*. 2014, vol. 346, no. 6214, pp. 1215–1218. ISSN 1095-9203.

[7] BLIEM, R., R. KOSAK, L. PERNECZKY, Z. NOVOTNY, O. GAMBA, D. FOBES, Z. MAO, M. SCHMID, P. BLAHA, U. DIEBOLD and et AL. Cluster Nucleation and Growth from a Highly Supersaturated Adatom Phase: Silver on Magnetite. *ACS Nano*. 2014, vol. 8, no. 7, pp. 753–7537. ISSN 1936-086X.

[8] BRAGG, W. H. The Structure of Magnetite and the Spinels. *Nature*. 1915, vol. 95, no. 2386, pp. 561–561. ISSN 0028-0836.

[9] VERVEY, E. J. W. Electronic Conduction of Magnetite (Fe3O4) and its Transition Point at Low Temperatures. *Nature*. 1939, vol. 144, no. 3642, pp. 327–328. ISSN 0028-0836.

[10] LIU, Jing-fu, Zong-shan ZHAO and Gui-bin JIANG. Coating Fe3O4 Magnetic Nanoparticles with Humic Acid for High Efficient Removal of Heavy Metals in Water. *Environ. Sci. Technol.* 2008, vol. 42, no. 18, pp. 6949–6954. ISSN 1520-5851.

[11] PARKINSON, G. S. Iron Oxide Surfaces. *Surface Science Reports*. 2016.

[12] XU, Z., F.-S. XIAO, S. K. PURNELL, O. ALEXEEV, S. KAWI, S. E. DEUTSCH and B. C. GATES. Size-dependent catalytic activity of supported metal clusters. *Nature*. 1994, vol. 372, no. 6504, pp. 346–348. ISSN 0028-0836.

[13] HARUTA, M. Size- and support-dependency in the catalysis of gold. *Catalysis Today*. 1997, vol. 36, no. 1, pp. 153–166. ISSN 0920-5861.

[14] TURNER, M., V. B. GOLOVKO, O. P. H. VAUGHAN, P. ABDULKIN, A. BERENGUER-MURCIA, M. S. TIKHOV, B. F. G. JOHNSON and R. M. LAMBERT. Selective oxidation with dioxygen by gold nanoparticle catalysts derived from 55-atom clusters. *Nature*. 2008, vol. 454, no. 7207, pp. 981–983. ISSN 1476-4687.

[15] VAJDA, S., M. J. PELLIN, J. P. GREELEY, C. L. MARSHALL, L. A. CURTISS, G. A. BALLENTINE, J. W. ELAM, S. CATILLON-MUCHERIE, P. C. REDFERN, F. MEHMOOD and et AL. Subnanometre platinum clusters as highly active and selective catalysts for the oxidative dehydrogenation of propane. *Nat Mater*. 2009, vol. 8, no. 3, pp. 213–216. ISSN 1476-4660.

[16] FU, Q. Active Nonmetallic Au and Pt Species on Ceria-Based Water-Gas Shift Catalysts. *Science*. 2003, vol. 301, no. 5635, pp. 935–938. ISSN 1095-9203.

[17] QIAO, B., A. WANG, X. YANG, L. F. ALLARD, Z. JIANG, Y. CUI, J. LIU, J. LI and T. ZHANG. Single-atom catalysis of CO oxidation using Pt1/FeOx. *Nature Chem*. 2011, vol. 3, no. 8, pp. 634–641. ISSN 1755-4349.

[18] LIN, Jian, Aiqin WANG, Botao QIAO, Xiaoyan LIU, Xiaofeng YANG, Xiaodong WANG, Jinxia LIANG, Jun LI, Jingyue LIU and Tao ZHANG. Remarkable Performance of Ir 1 /FeO x Single-Atom Catalyst in Water Gas Shift Reaction. *Journal of the American Chemical Society*. 2013, vol. 135, no. 41, pp. 15314 15317. ISSN 1520-5126.

[19] LIANG, S., C. HAO and Y. SHI. The Power of Single-Atom Catalysis. *ChemCatChem*. 2015, vol. 7, no. 17, pp. 2559–2567. ISSN 1867-3880.

[20] PARKINSON, G. S., Z. NOVOTNY, G. ARGENTERO, M. SCHMID, J. PAVELEC, R. KOSAK, P. BLAHA and U. DIEBOLD. Carbon monoxide-induced adatom sintering in a Pd/Fe3O4 model catalyst. *Nature Materials*. 2013, vol. 12, no. 8, pp. 724–728. ISSN 1476-4660.

[21] BLIEM, R., J. PAVELEC, O. GAMBA, E. MCDERMOTT, Z. WANG, S. GERHOLD, M. WAGNER, J. OSIECKI, K. SCHULTE, M. SCHMID and et AL. Adsorption and incorporation of transition metals at the magnetite Fe3O4 (001) surface. *Physical Review B*. 2015, vol. 92, no. 7. ISSN 1550-235X.

[22] BLIEM, R., J. van der HOEVEN, A. ZAVODNY, O. GAMBA, J. PAVELEC, P. E. de JONGH, M. SCHMID, U. DIEBOLD and G. S. PARKINSON. An Atomic-Scale View of CO and H 2 Oxidation on a Pt/Fe 3 O 4 Model Catalyst. *Angew. Chem. Int. Ed.* 2015, vol. 54, no. 47, pp. 13999–14002. ISSN 1433-7851.

[23] *Mineral database*. [online]. Available from: `http://www.mindat.org/min-29230.html`. [cited 18.04.2016].

[24] ZHAO, L., H. ZHANG, Y. XING, S. SONG, S. YU, W. SHI, X. GUO, J. YANG, Y. LEI and F. CAO. Morphology-Controlled Synthesis of Magnetites with Nanoporous Structures and Excellent Magnetic Properties. *Chem. Mater.* 2008, vol. 20, no. 1, pp. 198–204. ISSN 1520-5002.

[25] SANTOS-CARBALLAL, D., A. ROLDAN, R. GRAU-CRESPO and N. H. de LEEUW. A DFT study of the structures, stabilities and redox behaviour of the major surfaces of magnetite Fe3O4. *Phys. Chem. Chem. Phys.* 2014, vol. 16, no. 39, pp. 21082–21097. ISSN 1463-9084.

[26] YU, X., C.-F. HUO, Y.-W. LI, J. WANG and H. JIAO. Fe3O4 surface electronic structures and stability from GGA+U. *Surface Science*. 2012, vol. 606, no. 9-10, pp. 872–879. ISSN 0039-6028.

[27] YANG, T., X.-D. WEN, J. REN, Y.-W. LI, J.-G. WANG and C.-F. HUO. Surface structures of Fe3O4 (111), (110), and (001): A density functional theory study. *Journal of Fuel Chemistry and Technology*. 2010, vol. 38, no. 1, pp. 121–128. ISSN 1872-5813.

[28] PARKINSON, Gareth S., Peter LACKNER, Oscar GAMBA, Sebastian MAA , Stefan GERHOLD, Michele RIVA, Roland BLIEM, Ulrike DIEBOLD and Michael SCHMID. Fe3O4(110)-(1x3) revisited: Periodic (111) nanofacets. *Surface Science*. 2016, vol. 649, pp. 120–123. ISSN 0039-6028.

[29] WEISS, W. and W. RANKE. Surface chemistry and catalysis on well-defined epitaxial iron-oxide layers. *Progress in Surface Science*. 2002, vol. 70, no. 1-3, pp. 1–151. ISSN 0079-6816.

[30] PENTCHEVA, R., W. MORITZ, J. RUNDGREN, S. FRANK, D. SCHRUPP and M. SCHEFFLER. A combined DFT/LEED-approach for complex oxide surface structure determination: Fe3O4(001). *Surface Science*. 2008, vol. 602, no. 7, pp. 1299–1305. ISSN 0039-6028.

[31] GAO, G., X. LIU, R. SHI, K. ZHOU, Y. SHI, R. MA, E. TAKAYAMA-MUROMACHI and G. QIU. Shape-Controlled Synthesis and Magnetic Properties of Monodisperse Fe3O4 Nanocubes. *Crystal Growth & Design*. 2010, vol. 10, no. 7, pp. 2888–2894. ISSN 1528-7505.

[32] SIVULA, K., F. LE FORMAL and M. GRATZEL. Solar Water Splitting: Progress Using Hematite (alpha-Fe2O3) Photoelectrodes. *ChemSusChem*. 2011, vol. 4, no. 4, pp. 432–449. ISSN 1864-5631.

[33] HENDERSON, M. A., S. A. JOYCE and J. R. RUSTAD. Interaction of water with the (1x1) and (2x1) surfaces of α-Fe2O3(012). *Surface Science*. 1998, vol. 417, no. 1, pp. 66–81. ISSN 0039-6028.

[34] HUA, M., S. ZHANG, B. PAN, W. ZHANG, L. LV and Q. ZHANG. Heavy metal removal from water/wastewater by nanosized metal oxides: A review. *Journal of Hazardous Materials*. 2012, vol. 211-212, pp. 317–331. ISSN 0304-3894.

[35] TAMIRAT, A. G., J. RICK, A. A. DUBALE, W.-N. SU and B.-J. HWANG. Using hematite for photoelectrochemical water splitting: a review of current progress and challenges. *Nanoscale Horiz.* 2016. ISSN 2055-6764.

[36] ZBORIL, R., M. MASHLAN and D. PETRIDIS. Iron(III) Oxides from Thermal ProcessesSynthesis, Structural and Magnetic Properties, Modelssbauer Spectroscopy Characterization, and Applications. *Chem. Mater.* 2002, vol. 14, no. 3, pp. 969–982. ISSN 1520-5002.

[37] MORIN, F. J. Electrical Properties of alpha-Fe2O3 and alpha-Fe2O3 Containing Titanium. *Physical Review*. 1951, vol. 83, no. 5, pp. 1005–1010. ISSN 0031-899X.

[38] NAKAU, Tanehiro. Electrical Conductivity of alpha-Fe 2 O 3. *J. Phys. Soc. Jpn.* 1960, vol. 15, no. 4, pp. 727–727. ISSN 1347-4073.

[39] GUO, Haibo and Amanda S. BARNARD. Thermodynamic modelling of nanomorphologies of hematite and goethite. *J. Mater. Chem.* 2011, vol. 21, no. 31, pp. 11566–11577. ISSN 1364-5501.

[40] KUHLENBECK, H., S. SHAIKHUTDINOV and H. J. FREUND. Well-Ordered Transition Metal Oxide Layers in Model Catalysis - A Series of Case Studies. *Chem. Rev.* 2013, vol. 113, no. 6, pp. 3986–4034. ISSN 1520-6890.

[41] LAD, R. J. and V. E. HENRICH. Structure of α-Fe2O3 single crystal surfaces following Ar+ ion bombardment and annealing in O2. *Surface Science*. 1988, vol. 193, no. 1-2, pp. 81–93. ISSN 0039-6028.

[42] GAUTIER-SOYER, M., M. POLLAK, M. HENRIOT and M.J. GUITTET. The (1x2) reconstruction of the α-Fe2O3 (012) surface. *Surface Science*. 1996, vol. 352-354, pp. 112–116. ISSN 0039-6028.

[43] HENDERSON, M. A. Low temperature oxidation of Fe2+ surface sites on the (2x1) reconstructed surface of alpha-Fe2O3($01\bar{1}2$). *Surface Science*. 2010, vol. 604, no. 13-14, pp. 1197–1201. ISSN 0039-6028.

[44] HENDERSON, Michael A. Insights into the (1x1)-to-(2x1) phase transition of the α-Fe2O3(012) surface using EELS, LEED and water TPD. *Surface Science*. 2002, vol. 515, no. 1, pp. 253–262. ISSN 0039-6028.

[45] LOUNIS, S. Theory of Scanning Tunneling Microscopy. [online]. 2014. Available from: `http://arxiv.org/pdf/1404.0961.pdf`. [cited 10.05.2016].

[46] TERSOFF, J. and D. R. HAMANN. Theory of the scanning tunneling microscope. *Physical Review B*. 1985, vol. 31, no. 2, pp. 805–813. ISSN 0163-1829.

[47] LÜTH, Hans. *Solid Surfaces, Interfaces and Thin Films*. Springer Berlin Heidelberg, 2010. ISBN 9783642135927.

[48] SCHMID, M. *The Scanning Tunneling Microscope* [online]. Available from: `http://www.iap.tuwien.ac.at/www/surface/stm_gallery/stm_schematic`. [cited 15.05.2016].

[49] CECHAL, J. *Microscopy and Spectroscopy - lecture notes*.

[50] OURA, K., M. KATAYAMA, A. V. ZOTOV, V. G. LIFSHITS and A. A. SARANIN. Surface Science. *Advanced Texts in Physics*. 2003, pp. 440. ISSN 1439-2674.

[51] VIELSTICH, W. Methods in Electrocatalysis: Cyclic Voltammetry. In: *Handbook of Fuel Cells – Fundamentals, Technology and Applications*, Chichester: John Wiley & Sons, 2010. ISBN 9780470974001.

[52] MABBOTT, G. A. An introduction to cyclic voltammetry. *Journal of Chemical Education*. 1983, vol. 60, no. 9, pp. 697–702. ISSN 1938-1328.

[53] YAGATI, A. K., J. MIN and J.-W. CHOI. Electrochemical Scanning Tunneling Microscopy (ECSTM) - From Theory to Future Applications. *Modern Electrochemical Methods in Nano, Surface and Corrosion Science*. 2014.

[54] HOSTER, H. E. and H. A. GASTEIGER. Ex-situ surface preparation and analysis: Transfer between UHV and electrochemical cell. In: *Handbook of Fuel Cells – Fundamentals, Technology and Applications*, Chichester: John Wiley & Sons, 2003, pp. 236–265. ISBN 0471499269.

[55] CUESTA, A., M. KLEINERT and D. M. KOLB. The adsorption of sulfate and phosphate on Au(111) and Au(100) electrodes: an in situ STM study. *Physical Chemistry Chemical Physics*. 2000, vol. 2, no. 24, pp. 5684–5690. ISSN 1463-9084.

[56] PARKINSON, G. S., Z. NOVOTNY, P. JACOBSON, M. SCHMID and U. DIEBOLD. A metastable Fe(A) termination at the Fe3O4(001) surface. *Surface Science*. 2011, vol. 605, no. 15-16, pp. L42–L45. ISSN 0039-6028.

[57] GAMBA, O., H. NOEI, J. PAVELEC, R. BLIEM, M. SCHMID, U. DIEBOLD, A. STIERLE and G. S. PARKINSON. Adsorption of Formic Acid on the Fe3O4 (001) Surface. *The Journal of Physical Chemistry C*. 2015, vol. 119, no. 35, pp. 20459–20465. ISSN 1932-7455.

[58] PARKINSON, G. S., N. MULAKALURI, Y. LOSOVYJ, P. JACOBSON, R. PENTCHEVA and U. DIEBOLD. Semiconductor-half metal transition at the Fe3O4 (001) surface upon hydrogen adsorption. *Physical Review B*. 2010, vol. 82, no. 12, pp. 125413. ISSN 1550-235X.

[59] MULAKALURI, N., R. PENTCHEVA, M. WIELAND, W. MORITZ and M. SCHEFFLER. Partial Dissociation of Water on Fe3O4 (001): Adsorbate Induced Charge and Orbital Order. *Physical Review Letters*. 2009, vol. 103, no. 17, pp. 176102. ISSN 1079-7114.

[60] LIAO, P. and E. A. CARTER. Testing variations of the GW approximation on strongly correlated transition metal oxides: hematite (-Fe2O3) as a benchmark. *Physical Chemistry Chemical Physics* [online]. 2011, vol. 13, no. 33, pp. 15189–15199. ISSN 1463-9084. Available from: doi:10.1039/c1cp20829b. Available from: `http://dx.doi.org/10.1039/c1cp20829b`.

[61] TASKER, P.W. The stability of ionic crystal surfaces. *Journal of Physics C: Solid State Physics*. 1979, vol. 12, no. 22, pp. 4977–4984.

[62] KETTELER, Guido, Werner WEISS, Wolfgang RANKE and Robert SCHL GL. Bulk and surface phases of iron oxides in an oxygen and water atmosphere at low pressure. *Physical Chemistry Chemical Physics*. 2001, vol. 3, no. 6, pp. 1114–1122. ISSN 1463-9084.

[63] Van de KROL, R., Y. LIANG and J. SCHOONMAN. Solar hydrogen production with nanostructured metal oxides. *J. Mater. Chem.* 2008, vol. 18, no. 20, pp. 2311–2320. ISSN 1364-5501.

List of abbreviations

In order of appearance:

UHV	Ultra-High Vacuum
EC	Electrochemical Environment
STM	Scanning Tunneling Microscope
SAC	Single Atom Catalysis
TEM	Transmission Electron Microscope
SCV	Surface Cation Vacancy termination
DBT	Distorted Bulk Termination
DFT	Density Functional Theory
DFT+U	Density Functional Theory with Hubbard potential
LEED	Low-Energy Electron Diffraction
LEED IV	quantitative Low-Energy Electron Diffraction
PEC	Photoelectrochemical Cell
XPS	X-ray Photoelectron Spectroscopy
AES	Auger Electron Spectroscopy
EELS	Electron Energy Loss Spectroscopy
TPD	Temperature Programmed Desorption
AFM	Atomic Force Microscope
SPM	Scanning Probe Microscope
ESCA	Electron Spectroscopy for Chemical Analysis (synonym to XPS)
CCD	Charge-Coupled Device
WE	Working Electrode
CE	Counter Electrode

RE	Reference Electrode
EC-STM	Electrochemical Scanning Tunneling Microscope
PTFE	Polytetrafluorethylene (Teflon)
PCTFE	Polychlorotrifluoroethene (Kel-F)
PEEK	Polyether Ether Ketone
ISS	Ion Scattering Spectroscopy
RHE	Reversible Hydrogen Electrode
QCM	Quartz Crystal Microbalances
APDB	Anti-Phase Domain Boundary
ML	Monolayer
DOS	Density Of States
FFT	Fast Fourier Transform

List of supplementary data

Technical drawings

- `1_UHV_Holder_Locking` – Technical drawings of the individual parts and the assembly of the holder with locking mechanism described in section 3.5.1.
- `2_PEEK_holder` – Technical drawings of the individual parts and the assembly of the PEEK holder described in section 3.5.2.